The Astronomical Journal, 147:82 (47pp), 2014 April doi:10.1088/0004-6256/147/4/82

CSI 2264: SIMULTANEOUS OPTICAL AND INFRARED LIGHT CURVES OF YOUNG DISK-BEARING STARS IN NGC 2264 WITH *CoRoT* and *SPITZER*—EVIDENCE FOR MULTIPLE ORIGINS OF VARIABILITY*

Ann Marie Cody[1], John Stauffer[1], Annie Baglin[2], Giuseppina Micela[3], Luisa M. Rebull[1], Ettore Flaccomio[3], María Morales-Calderón[4], Suzanne Aigrain[5], Jèrôme Bouvier[6], Lynne A. Hillenbrand[7], Robert Gutermuth[8], Inseok Song[9], Neal Turner[10], Silvia H. P. Alencar[11], Konstanze Zwintz[12], Peter Plavchan[13], John Carpenter[7], Krzysztof Findeisen[7], Sean Carey[1], Susan Terebey[14], Lee Hartmann[15], Nuria Calvet[15], Paula Teixeira[16], Frederick J. Vrba[17], Scott Wolk[18], Kevin Covey[19], Katja Poppenhaeger[18], Hans Moritz Günther[18], Jan Forbrich[16,18], Barbara Whitney[20], Laura Affer[3], William Herbst[21], Joseph Hora[18], David Barrado[4], Jon Holtzman[22], Franck Marchis[23], Kenneth Wood[24], Marcelo Medeiros Guimarães[25], Jorge Lillo Box[4], Ed Gillen[5], Amy McQuillan[26], Catherine Espaillat[27], Lori Allen[28], Paola D'Alessio[29,31], and Fabio Favata[30]
[1] Spitzer Science Center, California Institute of Technology, 1200 East California Boulevard, Pasadena, CA 91125, USA; amc@ipac.caltech.edu
[2] LESIA, Observatoire de Paris-Meudon, 5 place Jules Janssen, F-92195 Meudon, France
[3] INAF–Osservatorio Astronomico di Palermo, Piazza del Parlamento 1, I-90134 Palermo, Italy
[4] Centro de Astrobiología, Dpto. de Astrofísica, INTA-CSIC, P.O. Box 78, ESAC Campus, E-28691 Villanueva de la Cañada, Madrid, Spain
[5] Department of Astrophysics, Denys Wilkinson Building, University of Oxford, Oxford OX1 3RH, UK
[6] UJF-Grenoble 1/CNRS-INSU, Institut de Planétologie et d'Astrophysique de Grenoble (IPAG) UMR 5274, F-38041 Grenoble, France
[7] Astronomy Department, California Institute of Technology, Pasadena, CA 91125, USA
[8] Department of Astronomy, University of Massachusetts, Amherst, MA 01003, USA
[9] Department of Physics and Astronomy, The University of Georgia, Athens, GA 30602-2451, USA
[10] Jet Propulsion Laboratory, California Institute of Technology, Pasadena, CA 91109, USA
[11] Departamento de Física – ICEx – UFMG, Av. Antônio Carlos 6627, 30270-901 Belo Horizonte, MG, Brazil
[12] Instituut voor Sterrenkunde, K. U. Leuven, Celestijnenlaan 200D, B-3001 Leuven, Belgium
[13] Infrared Processing and Analysis Center, California Institute of Technology, Pasadena, CA 91125, USA
[14] Department of Physics and Astronomy, 5151 State University Drive, California State University at Los Angeles, Los Angeles, CA 90032, USA
[15] Department of Astronomy, University of Michigan, 500 Church Street, Ann Arbor, MI 48105, USA
[16] Department of Astrophysics, University of Vienna, Türkenschanzstr. 17, A-1180 Vienna, Austria
[17] U.S. Naval Observatory, Flagstaff Station, 10391 West Naval Observatory Road, Flagstaff, AZ 86001, USA
[18] Harvard-Smithsonian Center for Astrophysics, Cambridge, MA 02138, USA
[19] Lowell Observatory, 1400 West Mars Hill Road, Flagstaff, AZ 86001, USA
[20] Astronomy Department, University of Wisconsin–Madison, 475 North Charter Street, Madison, WI 53706, USA
[21] Astronomy Department, Wesleyan University, Middletown, CT 06459, USA
[22] Department of Astronomy, New Mexico State University, Box 30001, Las Cruces, NM 88003, USA
[23] Carl Sagan Center at the SETI Institute, 189 Bernardo Avenue, Mountain View, CA 94043, USA
[24] School of Physics and Astronomy, University of St Andrews, North Haugh, St Andrews, Fife KY16 9AD, UK
[25] Departamento de Física e Matemática – UFSJ – Rodovia MG 443 KM7, 36420-000 Ouro Branco, MG, Brazil
[26] School of Physics and Astronomy, Raymond and Beverly Sackler, Faculty of Exact Sciences, Tel Aviv University, 69978 Tel Aviv, Israel
[27] Department of Astronomy, Boston University, 725 Commonwealth Avenue, Boston, MA 02215, USA
[28] National Optical Astronomy Observatories, Tucson, AZ 85719, USA
[29] Centro de Radioastronomía y Astrofsica, UNAM, Apartado Postal 3-72 (Xangari), 58089 Morelia, Michoacán, Mexico
[30] European Space Agency, 8-10 rue Mario Nikis, F-75738 Paris Cedex 15, France
Received 2013 November 12; accepted 2014 January 21; published 2014 March 13

ABSTRACT

We present the Coordinated Synoptic Investigation of NGC 2264, a continuous 30 day multi-wavelength photometric monitoring campaign on more than 1000 young cluster members using 16 telescopes. The unprecedented combination of multi-wavelength, high-precision, high-cadence, and long-duration data opens a new window into the time domain behavior of young stellar objects. Here we provide an overview of the observations, focusing on results from *Spitzer* and *CoRoT*. The highlight of this work is detailed analysis of 162 classical T Tauri stars for which we can probe optical and mid-infrared flux variations to 1% amplitudes and sub-hour timescales. We present a morphological variability census and then use metrics of periodicity, stochasticity, and symmetry to statistically separate the light curves into seven distinct classes, which we suggest represent different physical processes and geometric effects. We provide distributions of the characteristic timescales and amplitudes and assess the fractional representation within each class. The largest category (>20%) are optical "dippers" with discrete fading events lasting ∼1–5 days. The degree of correlation between the optical and infrared light curves is positive but weak; notably, the independently assigned optical and infrared morphology classes tend to be different for the same object. Assessment of flux variation behavior with respect to (circum)stellar properties reveals correlations of variability parameters with Hα emission and with effective temperature. Overall, our results point to multiple origins of young star variability, including circumstellar obscuration events, hot spots on the star and/or disk, accretion bursts, and rapid structural changes in the inner disk.

Key words: accretion, accretion disks – circumstellar matter – protoplanetary disks – stars: pre-main sequence – stars: variables: T Tauri, Herbig Ae/Be – techniques: photometric

Online-only material: color figures, extended figure

1. INTRODUCTION

Photometric variability on a variety of timescales is a long-appreciated characteristic of young stellar objects (YSOs). Since the initial association of brightness fluctuations with emission line objects near molecular clouds (Joy 1949), it has been inferred that YSO variability arises from a combination of physical processes operating at and near the stellar surface. The weak-lined T Tauri stars (WTTSs), so called for their lack of spectroscopic accretion signatures, tend to display stable sinusoidal light curves attributed to cool magnetic spots on the stellar surface (e.g., Stassun et al. 1999; Grankin et al. 2008; Rodríguez-Ledesma et al. 2009; Frasca et al. 2009). The classical T Tauri stars (CTTSs), on the other hand, typically exhibit much more complex time domain behavior, with light curves categorized as stochastic (e.g., Rucinski et al. 2008; Siwak et al. 2011), intermittently fading (e.g., Cody & Hillenbrand 2010; Alencar et al. 2010), or semi-periodic (e.g., Vrba et al. 1993; Herbst et al. 1994). Most of the photometric monitoring surveys conducted over the past few decades have focused on optical or near-infrared variability on timescales of days to years (e.g., Bouvier et al. 1993; Herbst et al. 1994, 2000; Skrutskie et al. 1996; Batalha et al. 1998; Cohen et al. 2004; Makidon et al. 2004; Caballero et al. 2004; Grankin et al. 2007; Alves de Oliveira & Casali 2008; Scholz 2012; Wolk et al. 2013; Parks et al. 2014). While they showed that brightness fluctuations are common at the 1%–10% level, sparse or uneven time sampling often precluded full assessment of variability, for CTTSs in particular. Ultimately, a full understanding of the time-domain properties of young stars is needed to inform models of their interaction with surrounding disks, the accretion process, as well as structure and geometry of star-disk systems.

Aperiodic or partially periodic variability in CTTSs has been attributed to a number of mechanisms, including obscuration by circumstellar material (e.g., Herbst et al. 1994; Chelli et al. 1999; Alencar et al. 2010), instabilities in the accretion shock at the stellar surface (Koldoba et al. 2008), unsteady accretion and hot spot evolution (e.g., Fernandez & Eiroa 1996; Stassun & Wood 1999; Carpenter et al. 2002; Scholz et al. 2009; van Boekel et al. 2010), and instabilities in the accretion disk (e.g., Bertout et al. 1988; Bertout 1989; Bouvier et al. 2007). A number of parameters, including magnetic field strength and shape (Cauley et al. 2012), disk structure (Flaherty et al. 2012; Wolk et al. 2013), stellar mass (Herbst & Shevchenko 1999), and rotation rate (Grankin et al. 2007), also appear to influence variability properties. Given these complexities, few theoretical models offer detailed, verifiable predictions on the time domain behavior of young stars. Some attempts to match the optical and near-infrared time domain properties of young stars to simple models (e.g., Herbst et al. 1994; Carpenter et al. 2001; Scholz et al. 2009; Rice et al. 2012; Faesi et al. 2012) have noted photometric behavior that is largely consistent with variable accretion, hot spots, or obscuration. Nevertheless, these very different physical scenarios could not be distinguished unambiguously from the limited time and wavelength coverage of ground-based data.

Recently, it has become increasingly clear that YSOs are not only variable on timescales as short as hours (Rucinski et al. 2008), but these brightness changes also appear at a wide range of wavelengths in individual objects (Rebull 2011, and references therein). Monitoring of disk-bearing stars by Eiroa et al. (2002) revealed optical and near-IR flux changes on 1–2 day timescales. While they speculated that changes in disk structure could produce disk emission or scattered light variations, the rapidity is difficult to explain. Wolk et al. (2013) too found a variety of near-IR variability, but on much longer timescales of multiple months. At longer wavelengths, Barsony et al. (2005) found large-amplitude mid-infrared variability preferentially among disks at early evolutionary stages. Instruments aboard the *Spitzer Space Telescope* (Werner et al. 2004) and *Herschel* (Pilbratt et al. 2010) have also enabled Muzerolle et al. (2009), Espaillat et al. (2011), Morales-Calderón et al. (2011), and Billot et al. (2012) to uncover mid- to far-infrared brightness fluctuations in disk-bearing young stars. Complementary modeling efforts such as those by Dullemond et al. (2003), Flaherty & Muzerolle (2010), and Romanova et al. (2011) have begun to offer detailed descriptions of inner disk dynamics and star-disk interaction but nevertheless require more extensive input from observations on more varied timescales and wavelengths. Despite the headway in matching observed brightness fluctuations to physical models, the sparseness or non-simultaneity of data taken in different bands has hindered a full explanation of young star variability.

The ongoing Young Stellar Object Variability (YSOVAR) project (Morales-Calderón et al. 2011; L. Rebull 2014, in preparation) is exploring the variability properties of young stars in several young clusters at an unprecedented combination of cadence, photometric precision, and wavelength coverage, particularly in the infrared. Variable accretion and extinction, as well as disk warps, shadowing, and magnetic instabilities, have been cited as plausible mid-IR variability mechanisms, and YSOVAR offers the best opportunity to untangle them. On the heels of this project, we have performed photometric monitoring of young NGC 2264 cluster members using the *Spitzer* Infrared Array Camera (IRAC; Fazio et al. 2004) and the *Convection, Rotation and Planetary Transits* satellite (*CoRoT*; Baglin et al. 2006) simultaneously. This campaign—the Coordinated Synoptic Investigation of NGC 2264 (CSI 2264)—constitutes a unique cooperative effort including 15 ground- and space-based telescopes, listed in Table 1. In this paper we focus exclusively on the results of optical and infrared photometric monitoring with *CoRoT* and *Spitzer* as part of CSI 2264; discussion of data acquired from other instruments is deferred to subsequent papers.

With sub-1% photometry at cadences down to a few minutes, these two space telescopes have provided the first set of simultaneous fully sampled light curves in the optical and infrared. Whereas previous studies of YSOs in NGC 2264 (e.g., Lamm et al. 2004; Makidon et al. 2004) and other regions had insufficient time sampling to identify more than generic aperiodic flux variations, we are able to resolve brightness fluctuations on all relevant timescales expected from significant variability mechanisms. From the exquisite *CoRoT* and *Spitzer* time series, we present here a census of light-curve morphologies based on an unbiased set of disk-bearing stars in NGC 2264. We first develop a visual classification scheme, which we then confirm via quantitative metrics that can be determined on any light curve without manual intervention. With distinct morphology classes in hand, we proceed to provide quantitative measures of timescales, periodicities, amplitudes, and correlations, as constraints on the theoretical models currently in development. We use only measurements from *CoRoT* and *Spitzer* light curves

* Based on data from the *Spitzer* and *CoRoT* missions. The *CoRoT* space mission was developed and is operated by the French space agency CNES, with participation of ESA's RSSD and Science Programmes, Austria, Belgium, Brazil, Germany, and Spain.
[31] Deceased.

Table 1
Coordinated Synoptic Investigation of NGC 2264: Observations

Telescope	Instrument	Dates	Band(s)	Time Sampling
Spitzer	IRAC/mapping	2011 Dec 3–2012 Jan 1	3.6 μm, 4.5 μm	101 minutes
Spitzer	IRAC/staring	2011 Dec 3; Dec 5–6; Dec 7–8; Dec 8–9	3.6 μm, 4.5 μm	15 s
CoRoT	E2 CCD	2011 Dec 1–2012 Jan 3	3000–10000 Å	32 s (high cadence), 512 s
MOST	Science CCD	2011 Dec 5–2012 Jan 14	3500–7500 Å	24.1, 51.2 s[a]
Chandra	ACIS-I	2011 Dec 3–2011 Dec 9	0.5–8 keV	~3.2 s[b]
VLT	Flames, UVES	2011 Dec 4–2012 Feb 29	4800–6800 Å	20–22 epochs
CFHT	MegaCam	2012 Feb 14–2012 Feb 28	*u*, *r*	30 epochs
PAIRITEL	2MASS camera	2011 Dec 5–2012 Jan 3	*J*, *H*, *K*	1–12 epochs
USNO 40 inch telescope	CCD	2011 Nov 22–2012 Mar 9	*I*	912–1026 epochs
Super-LOTIS	CCD	2011 Nov 11–2012 Mar 1	*I*	495–522 epochs
NMSU 1 m telescope	CCD	2011 Oct 12–2012 Mar 4	*I*	47–54 epochs
Lowell 31 inch telescope	CCD	2011 Oct 12–2012 Jan 14	*I*	44 epochs
OAN 1.5 m telescope	CCD	2012 Jan 10–2012 Feb 15	*V*, *I*	23–28 epochs
KPNO 2.1 m telescope	FLAMINGOS	2011 Dec 16–2012 Jan 3	*J*, *H*, K_S	40–52 epochs
FLWO 60 inch telescope	KeplerCam	2011 Nov 30–2012 Jan 26	*U*	35–60 epochs
ESO 2.2 m telescope	WFI	2012 Dec 24–2011 Dec 29	*U*, *V*, *I*	25–45 epochs
CAHA 3.5 m telescope	Omega 2000	2011 Dec 5–2012 Feb 18	*J*, *H*, *K*	35 epochs
CAHA 3.5 m telescope	LAICA	2012 Jan 25–26	*u*, *r*	20 epochs

Notes. We provide the details of observing runs associated with the Coordinated Synoptic Investigation of NGC 2264. Some of the data were not used due to non-photometric conditions. We also note that the fields of view were not the same for all instruments. In many cases we monitored a number of 5′–20′ regions at slightly different cadences, depending on weather. In the time sampling column, we show either the time between each data point or the total number of data points per field for the unevenly sampled ground-based runs.
[a] We note that *MOST* data for each of two fields were taken over only about half of each 101 minute orbit. Observations with a number of epochs listed were not taken at regular intervals, because of weather interruptions, and many of them involved multiple fields.
[b] The cadence listed for *Chandra* observations is the temporal resolution of photon arrival times during the exposures.

to explore connections between morphology and physical processes in this paper. In future work, we will incorporate additional multiwavelength and spectroscopic data collected by the CSI 2264 project to further constrain variability mechanisms.

The structure of this paper is as follows: In Section 2 we describe the stellar sample; in Sections 3 and 4 we describe the observations and data reduction. In Section 5 we present our classification of optical/infrared light-curve morphologies, and in Section 6 we provide a statistical characterization of the variables. In Section 7 we investigate the correlation of optical and infrared light-curve morphologies, subsequently exploring the relationship between variability properties and stellar and disk observables (Section 8).

2. SAMPLE SELECTION

At ~760 pc (Park et al. 2000) and ~1–5 Myr (Rebull et al. 2002; Dahm 2008), NGC 2264 provides a rich selection of pre-main-sequence objects with masses from the substellar regime through ~7 $M_\odot$. It includes areas of recent star formation where embedded stars are visible only at infrared and longer wavelengths (Teixeira et al. 2012), as well as lower extinction regions with 1000 to 2000 optical sources. The membership of this cluster is well characterized (Sung et al. 1997; Rebull et al. 2002; Ramírez et al. 2004a; Dahm & Simon 2005), encompassing a large population for time series studies. The bulk of members are within a one square degree region of sky, comparable to the fields of view covered by *CoRoT* and *Spitzer*, as shown in Figure 1. Our goal in studying variability among the YSOs in NGC 2264 is to analyze multiwavelength flux behavior in a relatively unbiased sample of disk-bearing members. Since *CoRoT* only observes using pre-selected pixel masks, we mined all of the available published data in advance to identify highly probable cluster members with previously derived stellar properties. A summary of our membership selection criteria is available in the Appendix; these resulted in a list of over ~1500 cluster members. For convenience of identification, we have assembled a comprehensive catalog of all cluster members, candidates, and field stars in the NGC 2264 field of view (FOV),

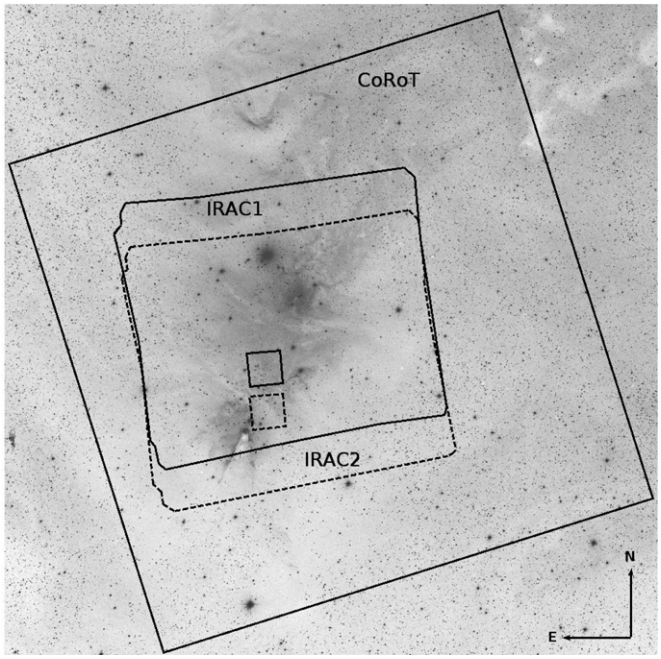

Figure 1. Field of view for IRAC and *CoRoT* observations of NGC 2264 carried out in 2011 December. The underlying image is from the Digitized Sky Survey (Lasker et al. 1990). The smaller square regions represent the IRAC staring fields in channel 1 (solid line) and channel 2 (dashed line). The large region observed by *CoRoT* is 1.°3 × 1.°3.

Table 2
CSI 2264 Sample Subsets

	Spitzer	*CoRoT*	Both
Total stars observed	19892	4235	1303
Field stars	17043	2129	184
Candidates	1583	1617	665
Members	1266	489	454
Class III	574	305	288
Unknown SED	59	8	3
Disk bearing	633	176	163[a]
Class II/III	90	24	23
Class II	389	140	129
Flat SED	65	9	8
Class I	89	3	3

Notes. The number of stars observed in each subset of the CSI 2264 sample. Members were selected according to the criteria in the Appendix, and candidates are objects that satisfy only one of those criteria. SED classes are derived in Section 2.1.

[a] Group discussed in this paper (i.e., disk-bearing members in both *CoRoT* and *Spitzer*); the actual sample size was 162, after removal of a low-quality light curve with few data points.

using the ID structure "CSI Mon," or "Mon" in shorthand. The full catalog of over 100,000 sources will be deferred to a later publication, and we list only the objects considered in this work by their Mon numbers.

We selected 489 high-probability cluster members for observation by *CoRoT* in 2011, along with a *Spitzer* FOV encompassing 1266 members. Selection was done by priority, with 450 members and candidate members (i.e., meeting only one of two membership criteria listed in the Appendix) previously observed by *CoRoT* during its 2008 SRa01 run having highest priority. The second level of priority consisted of 322 CTTSs not previously observed by *CoRoT*, and with $I < 17$. Lower priority objects were all WTTSs not previously observed by *CoRoT*. Previous variability was not a selection criterion, and therefore we expect the CTTS sample analyzed in this paper to be nearly unbiased. The breakdown of CTTSs versus WTTSs, however, is probably not reflective of the cluster distribution as a whole. To retain only those members with circumstellar disks, we next apply additional criteria, as discussed below. It is this subset of stars whose variability properties we will study in Sections 5–8. For reference, we provide the numbers of member and field objects in the *Spitzer* and *CoRoT* samples in Table 2.

2.1. Identification of Disk-bearing Objects

We now narrow our focus to the NGC 2264 sample of stars with infrared excesses indicative of circumstellar disks. Our main approach is to measure the slope, α, of the spectral energy distribution (SED) at near- and mid-infrared wavelengths, and to compare to the expectation of a bare stellar photosphere. Several different disk classification schemes exist in the literature. The most recent analysis of NGC 2264 members by Sung et al. (2009) involved the five classes I, II, III, pre-transitional, and transitional, based primarily on the loci of photometric points on infrared color–color diagrams. Since the definition of transitional disks has been a subject of debate and the set of infrared photometry is not complete for all objects, we prefer the SED slope definition (see Evans et al. 2009). These are systems that have outer disk properties of normal T Tauri stars but with inner disk holes or gaps.

Following Wilking et al. (2001) with some guidance also from Lada & Wilking (1984), Greene et al. (1994), and Bachiller (1996), we define $\alpha = d\log\lambda F_\lambda / d\log\lambda$ for flux F_λ as a function of wavelength, λ. We classify $\alpha > 0.3$ for Class I, 0.3 to −0.3 for flat-spectrum sources, −0.3 to −1.6 for Class II, and < -1.6 for Class III. The notation II/III is reserved for transitional type disks, as described below. For all objects in our *Spitzer* sample, we performed a least-squares linear fit to all available photometry (not including upper or lower limits) as observed between 2 and 24 μm. We obtained data at 5.8 μm and longer wavelengths from cryogenic *Spitzer* observations. To maintain consistency with the approach taken by the YSOVAR project (L. Rebull 2014, in preparation), we obtained archival IRAC and Multiband Imaging Photometry for Spitzer (MIPS) data (program IDs 3441, 3469, 50773, and 37) and performed our own photometric reduction with Cluster Grinder (Gutermuth et al. 2009). We produced photometry for all sources in the NGC 2264 region with a signal-to-noise ratio of at least 5. For objects in the Sung et al. (2009) sample, our absolute photometry agrees with theirs to within 1%. We note that formal errors on the infrared points are so small as to not affect the fitted SED slope. The fit was performed on the observed SED, with no reddening corrections. Accounting for reddening is unlikely to change the SED class, since all of our targets with *CoRoT* data are in low-extinction regions of the cluster. Variability could also alter the shape of the SEDs slightly, since not all of the photometry was obtained simultaneously. However, we find that an allowance of 15% uncertainty does not change the classification appreciably. We provide this slope assessment, as opposed to that of Sung et al. (2009), to ensure internal consistency and enable comparison with other clusters in the YSOVAR sample (see L. Rebull 2014, in preparation).

For objects with MIPS data (131 in the combined *CoRoT*/*Spitzer* sample), we compared the α value and resulting disk class derived with and without the 24 μm point. Disagreement occurred for around one-quarter of these, primarily due to disjoint 24 μm photometry compared to the shorter wavelength SED. In the majority of these cases, the disk is transitional. However, in others, it is possible that nebulosity is causing a false excess at long wavelengths, and we have adopted the α value from 2–8 μm data. For all disagreements, we visually inspected the SEDs to determine the most appropriate wavelength range for slope determination. We identified a total of 140 disk-bearing objects among NGC 2264 members targeted for observation with both *Spitzer*/IRAC and *CoRoT*.

There are additional cases where misclassifications may have occurred, such that disk-bearing stars are labeled as diskless. Several objects display high-amplitude variability, but their mid-infrared SED slopes of less than −1.6 result in Class III status. To assess whether they might have weak disks, we examined their [3.6]–[8.0] IRAC colors. Analysis of infrared photometry in other clusters (e.g., Cieza & Baliber 2006; Cody & Hillenbrand 2010) has shown that the requirement [3.6]–[8.0] > 0.7 is a fairly robust disk selection criterion, whereas [3.6]–[8.0] < 0.4 selects diskless stars with high accuracy. Using the 0.7 cutoff, we identified 23 additional stars in the *Spitzer* and *CoRoT* fields with weak or transitional disks, which are confirmed by visual inspection of the SEDs, revealing infrared excess above the expected photospheric flux level predicted from the stellar spectral type. We adopt the disk class "II/III" for these objects and present them along with the rest of the disk-bearing sample in common with *CoRoT* observations in Table 3. We also list the 2MASS and *CoRoT* cross matches here.

Table 3
NGC 2264 Members Monitored with *CoRoT* and *Spitzer*

Object	2MASS ID	*CoRoT* ID	*J*	*H*	*K*	[3.6]	[4.5]	[5.8]	[8.0]	[24]	Class	SpT	Hα	Comp?
CSI Mon-000007	J06415304+0958028	223994721	12.22 ± 0.02	11.53 ± 0.03	11.18 ± 0.02	10.12 ± 0.00	9.74 ± 0.00	9.32 ± 0.00	8.75 ± 0.00	6.20 ± 0.03	II	K7	...	Y
CSI Mon-000011	J06411725+0954323	223985009	12.83 ± 0.02	12.05 ± 0.03	11.55 ± 0.02	10.49 ± 0.00	10.07 ± 0.00	9.69 ± 0.00	8.82 ± 0.00	5.60 ± 0.01	II	K7	58.30	N
CSI Mon-000012	J06410934+0956081	602099712	11.91 ± 0.03	10.57 ± 0.03	10.00 ± 0.03	9.54 ± 0.00	9.31 ± 0.00	9.01 ± 0.00	8.52 ± 0.00	6.50 ± 0.03	II	K5	2.33	Y
CSI Mon-000021	J06405944+0959454	223980412	12.78 ± 0.03	12.09 ± 0.03	11.69 ± 0.02	11.25 ± 0.00	10.94 ± 0.00	10.71 ± 0.01	10.05 ± 0.02	7.56 ± 0.12	II	K5	7.41	N
CSI Mon-000024	J06415684+0947451	603414392	14.74 ± 0.04	14.07 ± 0.05	13.81 ± 0.05	13.61 ± 0.01	13.55 ± 0.01	13.39 ± 0.07	12.84 ± 0.13	...	II/III	...	...	Y
CSI Mon-000056	J06415315+0950474	223994760	12.96 ± 0.02	12.30 ± 0.02	12.00 ± 0.03	11.72 ± 0.00	11.39 ± 0.00	11.04 ± 0.01	10.29 ± 0.01	7.87 ± 0.06	II	K5	1.80	N
CSI Mon-000058	J06420870+0941212	616895632	...	...	...	11.68	11.27	11.24 ± 0.02	...	5.70 ± 0.03	flat	...	94.00	N
CSI Mon-000063	J06411193+0959412	616826518	14.20 ± 0.04	13.52 ± 0.04	...	12.81 ± 0.01	12.58 ± 0.01	12.21 ± 0.03	11.46 ± 0.03	9.34 ± 0.18	II	M2.5	19.35	N
CSI Mon-000090*	J06410896+0933460	616919796	12.96 ± 0.02	12.14 ± 0.02	...	11.37 ± 0.00	11.08 ± 0.00	10.65 ± 0.01	9.58 ± 0.02	7.10 ± 0.10	II	M3	51.00	N
CSI Mon-000103*	J06405954+0935109	223980447	11.59 ± 0.03	10.70 ± 0.03	10.31 ± 0.02	9.69 ± 0.00	9.30 ± 0.00	8.88 ± 0.00	8.15 ± 0.00	5.63 ± 0.06	II	K6	6.40	N
CSI Mon-000109	J06413743+0937280	223990338	14.23 ± 0.03	13.70 ± 0.03	13.50 ± 0.05	13.54 ± 0.01	13.56 ± 0.01	13.34 ± 0.07	12.53 ± 0.13	...	II/III	...	...	N
CSI Mon-000117	J06405413+0948434	602095753	14.16 ± 0.03	13.43 ± 0.02	13.07 ± 0.03	12.45 ± 0.02	12.12 ± 0.02	12.07 ± 0.22	11.47 ± 0.64	...	II/III	M2.5	353.00	N
CSI Mon-000119	J06412100+0933361	223985987	12.43 ± 0.02	11.63 ± 0.02	11.19 ± 0.02	10.45 ± 0.00	10.11 ± 0.00	9.89 ± 0.00	9.16 ± 0.01	6.31 ± 0.05	II	K6	10.60	Y
CSI Mon-000123*	J06410821+0934094	616919795	12.97 ± 0.03	11.90 ± 0.03	11.50 ± 0.04	11.01 ± 0.01	10.69 ± 0.01	10.29 ± 0.01	9.39 ± 0.01	5.06 ± 0.03	II	...	12.00	N
CSI Mon-000126	J06405783+0941201	616895876	12.87 ± 0.03	11.91 ± 0.03	11.27 ± 0.02	10.30 ± 0.00	9.74 ± 0.00	9.28 ± 0.00	8.71 ± 0.00	5.75 ± 0.05	II	M0	26.40	N
CSI Mon-000131	J06404927+0923503	616969822	13.04 ± 0.02	12.31 ± 0.02	12.04 ± 0.02	11.85 ± 0.00	11.74 ± 0.00	11.59 ± 0.01	11.38 ± 0.02	6.63 ± 0.02	II	K7	35.90	N
CSI Mon-000134	J06411441+0926582	603808964	13.03 ± 0.03	12.33 ± 0.02	12.11 ± 0.02	11.91 ± 0.00	11.86 ± 0.01	11.67 ± 0.04	10.90 ± 0.07	7.00 ± 0.09	II	M3.5	2.70	Y
CSI Mon-000153	J06405990+0947044	400007889	14.04 ± 0.03	13.17 ± 0.03	12.65 ± 0.03	11.57 ± 0.00	11.26 ± 0.00	10.98 ± 0.02	10.51 ± 0.05	7.07 ± 0.14	II	M3	39.90	Y
CSI Mon-000164*	J06410450+0930134	616919778	13.97 ± 0.03	13.21 ± 0.03	13.03 ± 0.04	12.81 ± 0.01	12.67 ± 0.03	12.59 ± 0.10	11.91 ± 0.12	...	II/III	M	8.60	N
CSI Mon-000168	J06414287+0925084	223991832	13.57 ± 0.03	12.77 ± 0.03	12.30 ± 0.03	11.77 ± 0.00	11.53 ± 0.00	11.27 ± 0.01	10.38 ± 0.03	6.82 ± 0.05	II	...	86.00	N
CSI Mon-000177*	J06410620+0936229	223982136	11.64 ± 0.02	11.02 ± 0.02	10.55 ± 0.02	10.17 ± 0.00	9.88 ± 0.00	9.69 ± 0.01	9.29 ± 0.05	4.69 ± 0.08	II	G5	10.00	N
CSI Mon-000183	J06411650+0926082	602079851	14.53 ± 0.04	13.64 ± 0.03	13.18 ± 0.04	12.92 ± 0.01	12.51 ± 0.01	12.03 ± 0.06	11.40 ± 0.12	...	II	...	4.10	N
CSI Mon-000185	J06413876+0932117	616919566	12.88 ± 0.03	12.11 ± 0.02	11.72 ± 0.02	10.82 ± 0.00	10.59 ± 0.00	10.35 ± 0.01	9.76 ± 0.01	6.24 ± 0.01	II	K4	58.60	N
CSI Mon-000219	J06411890+0935541	616919663	14.54 ± 0.07	13.76 ± 0.07	13.51 ± 0.06	13.08 ± 0.01	12.83 ± 0.01	12.71 ± 0.04	12.16 ± 0.08	8.48 ± 0.27	II	...	...	N
CSI Mon-000242	J06411185+0926314	602079796	12.21 ± 0.03	11.52 ± 0.03	11.26 ± 0.03	10.82 ± 0.00	10.70 ± 0.00	9.57 ± 0.01	...	...	II	K7	5.40	N
CSI Mon-000250	J06410050+0945031	223980688	12.74 ± 0.02	12.02 ± 0.03	11.53 ± 0.03	10.88 ± 0.00	10.60 ± 0.00	10.42 ± 0.01	10.15 ± 0.02	6.74 ± 0.04	II	K3	15.00	N
CSI Mon-000256	J06414422+0925024	223992193	13.33 ± 0.03	12.61 ± 0.02	12.33 ± 0.03	11.77 ± 0.00	11.58 ± 0.00	11.37 ± 0.01	11.02 ± 0.04	8.35 ± 0.39	II	...	...	N
CSI Mon-000273	J06411837+0939411	616895921	13.41 ± 0.03	12.65 ± 0.03	12.46 ± 0.03	12.13 ± 0.00	12.03 ± 0.00	11.96 ± 0.02	11.61 ± 0.05	6.79 ± 0.04	II	M1	123.50	Y
CSI Mon-000279	J06412119+0932146	603402480	14.08 ± 0.03	13.40 ± 0.03	13.19 ± 0.04	12.90 ± 0.01	12.88 ± 0.01	12.62 ± 0.06	11.84 ± 0.13	...	II/III	M2.5	5.80	N
CSI Mon-000280	J06404100+0927543	616944098	13.69 ± 0.03	12.94 ± 0.04	12.67 ± 0.03	12.38 ± 0.01	12.21 ± 0.01	12.00 ± 0.03	11.55 ± 0.07	7.42 ± 0.05	II	...	13.20	N
CSI Mon-000290*	J06405867+0936132	223980233	12.41 ± 0.02	11.58 ± 0.02	11.13 ± 0.02	10.59 ± 0.01	10.29 ± 0.01	9.92 ± 0.02	9.33 ± 0.03	...	II	M4	22.20	N
CSI Mon-000296	J06405059+0954573	602099706	12.47 ± 0.02	11.69 ± 0.03	11.28 ± 0.03	10.75 ± 0.00	10.56 ± 0.00	10.41 ± 0.01	10.03 ± 0.04	5.71 ± 0.04	II	K2	11.20	N
CSI Mon-000297	J06404516+0928444	223976747	12.39 ± 0.03	11.67 ± 0.02	11.35 ± 0.03	10.99 ± 0.00	10.68 ± 0.00	10.66 ± 0.01	10.42 ± 0.01	6.09 ± 0.03	II	K2	7.20	N
CSI Mon-000305	J06405748+0954573	605538647	14.82 ± 0.04	14.26 ± 0.04	14.04 ± 0.06	13.81 ± 0.01	13.61 ± 0.01	13.61 ± 0.09	12.71 ± 0.21	...	II/III	...	...	N
CSI Mon-000314	J06404459+0932261	616919732	14.05 ± 0.04	13.34 ± 0.03	12.98 ± 0.04	12.54 ± 0.00	12.42 ± 0.00	12.37 ± 0.03	12.35 ± 0.13	7.49 ± 0.16	II	M3	60.00	N
CSI Mon-000325	J06405934+0955201	605538641	10.65 ± 0.02	10.06 ± 0.02	9.70 ± 0.02	9.15 ± 0.00	8.91 ± 0.00	8.57 ± 0.00	7.88 ± 0.00	5.30 ± 0.03	II	G6	−0.17	N
CSI Mon-000326	J06405882+0939187	223980258	13.66 ± 0.03	12.98 ± 0.02	12.72 ± 0.02	12.43 ± 0.00	12.33 ± 0.00	12.07 ± 0.02	11.21 ± 0.04	7.54 ± 0.04	II	M0	27.90	N
CSI Mon-000328	J06412700+0930131	400007735	13.81 ± 0.03	13.07 ± 0.03	12.88 ± 0.02	12.74 ± 0.00	12.71 ± 0.01	12.60 ± 0.03	11.86 ± 0.05	7.21 ± 0.16	II	M1	25.80	N
CSI Mon-000335	J06413728+0945066	223990299	12.93 ± 0.07	12.24 ± 0.05	11.95 ± 0.03	11.50 ± 0.00	11.28 ± 0.00	10.94 ± 0.01	9.80 ± 0.01	6.05 ± 0.03	II	K4	35.00	N
CSI Mon-000341	J06405426+0949203	616849439	13.10 ± 0.03	12.28 ± 0.03	11.80 ± 0.03	11.01 ± 0.01	10.45 ± 0.00	9.86 ± 0.03	8.74 ± 0.06	4.99 ± 0.10	flat	M0.5	161.10	N
CSI Mon-000342	J06405573+0946456	616872592	13.94 ± 0.03	13.28 ± 0.04	12.90 ± 0.03	12.40 ± 0.01	12.18 ± 0.01	11.80 ± 0.06	11.01 ± 0.18	6.54 ± 0.32	II	M4	21.10	N
CSI Mon-000346*	J06410908+0930090	603402478	12.94 ± 0.03	11.96 ± 0.04	11.54 ± 0.02	10.27 ± 0.02	9.79 ± 0.02	9.20 ± 0.06	8.45 ± 0.05	...	II	K7	27.00	Y
CSI Mon-000356	J06410506+0949228	616849458	13.99 ± 0.03	13.41 ± 0.02	13.07 ± 0.04	12.65 ± 0.01	12.40 ± 0.01	12.07 ± 0.03	11.07 ± 0.05	9.30 ± 0.42	II	...	8.30	N

Table 3
(Continued)

Object	2MASS ID	*CoRoT* ID	*J*	*H*	*K*	[3.6]	[4.5]	[5.8]	[8.0]	[24]	Class	SpT	Hα	Comp?
CSI Mon-000357*	J06410574+0931012	616919781	12.37 ± 0.03	11.59 ± 0.02	11.30 ± 0.02	10.77 ± 0.00	10.65 ± 0.00	10.40 ± 0.01	9.93 ± 0.04	6.49 ± 0.12	II	K5	8.00	N
CSI Mon-000358	J06410673+0947275	400007959	14.00 ± 0.03	13.25 ± 0.03	12.90 ± 0.03	12.31 ± 0.00	12.03 ± 0.01	11.85 ± 0.02	11.15 ± 0.03	7.58 ± 0.06	II	...	6.20	N
CSI Mon-000370*	J06405679+0937490	223979728	12.22 ± 0.03	11.50 ± 0.03	11.25 ± 0.02	10.96 ± 0.00	10.74 ± 0.00	10.44 ± 0.01	9.47 ± 0.02	5.91 ± 0.03	II	K5	113.20	Y
CSI Mon-000378	J06405292+0944544	616872605	12.70 ± 0.02	11.86 ± 0.02	11.27 ± 0.02	10.88 ± 0.00	10.54 ± 0.00	10.09 ± 0.01	9.37 ± 0.04	6.27 ± 0.24	II	K5.5	8.50	N
CSI Mon-000379	J06410497+0950460	223981811	12.24 ± 0.02	11.54 ± 0.03	11.09 ± 0.03	10.50 ± 0.00	10.29 ± 0.00	10.08 ± 0.01	9.62 ± 0.03	5.82 ± 0.04	II	K2	36.50	N
CSI Mon-000406*	J06405968+0928438	616943998	13.19 ± 0.03	12.41 ± 0.03	12.08 ± 0.03	11.37 ± 0.00	10.93 ± 0.00	10.49 ± 0.01	9.57 ± 0.03	6.66 ± 0.08	II	...	46.10	N
CSI Mon-000412	J06404711+0932401	616919737	12.77 ± 0.03	12.00 ± 0.02	11.69 ± 0.03	11.15 ± 0.00	10.76 ± 0.00	10.38 ± 0.01	9.71 ± 0.03	6.57 ± 0.06	II	M1	30.70	N
CSI Mon-000423	J06411485+0925550	602079850	15.65 ± 0.09	14.30 ± 0.03	13.45 ± 0.04	11.27 ± 0.01	10.73 ± 0.00	10.08 ± 0.03	9.08 ± 0.06	5.48 ± 0.05	flat	...	89.80	N
CSI Mon-000424	J06411521+0937576	616895917	13.72 ± 0.03	12.99 ± 0.02	12.70 ± 0.02	12.29 ± 0.00	11.87 ± 0.00	11.54 ± 0.02	10.63 ± 0.04	7.91 ± 0.28	II	M1	11.50	N
CSI Mon-000425	J06411668+0929522	616943882	11.27 ± 0.03	10.50 ± 0.02	10.07 ± 0.02	9.33 ± 0.00	8.96 ± 0.00	8.55 ± 0.00	7.43 ± 0.00	4.31 ± 0.05	II	K5	6.30	N
CSI Mon-000427	J06404244+0932206	223976099	13.23 ± 0.03	12.64 ± 0.03	12.52 ± 0.03	12.44 ± 0.01	12.40 ± 0.01	12.22 ± 0.07	11.41 ± 0.19	...	II/III	K4	0.50	N
CSI Mon-000433*	J06410111+0934522	616919770	12.88	...	...	11.61 ± 0.00	11.39 ± 0.00	11.26 ± 0.02	10.90 ± 0.06	6.14 ± 0.08	flat	...	7.00	N
CSI Mon-000434*	J06410406+0935211	616919776	13.02 ± 0.03	12.34 ± 0.02	12.10 ± 0.02	11.77 ± 0.01	11.48 ± 0.01	11.24 ± 0.03	10.23 ± 0.04	7.10 ± 0.12	II	M2.5	4.30	N
CSI Mon-000441*	J06405809+0936533	223980048	13.31 ± 0.03	12.48 ± 0.02	12.08 ± 0.02	11.32 ± 0.00	10.97 ± 0.00	10.62 ± 0.01	10.00 ± 0.03	7.37 ± 0.11	II	...	34.00	N
CSI Mon-000448*	J06410360+0930290	602083897	12.81 ± 0.03	12.03 ± 0.03	11.69 ± 0.03	11.26 ± 0.00	10.89 ± 0.01	10.48 ± 0.01	9.46 ± 0.01	5.62 ± 0.07	II	...	20.40	N
CSI Mon-000454*	J06410362+0936046	616895890	13.25	...	...	11.28 ± 0.08	10.97 ± 0.08	9.17 ± 0.29	...	...	I	...	...	N
CSI Mon-000456	J06405154+0943242	616872585	12.36 ± 0.02	11.62 ± 0.03	11.16 ± 0.03	10.56 ± 0.00	10.31 ± 0.00	10.19 ± 0.02	9.45 ± 0.05	5.86 ± 0.10	II	K4	13.10	N
CSI Mon-000457*	J06410673+0934459	616919789	11.76 ± 0.03	10.28 ± 0.03	9.23 ± 0.02	7.95 ± 0.00	7.35 ± 0.00	6.70 ± 0.00	5.43 ± 0.00	1.61 ± 0.00	flat	G6	49.40	N
CSI Mon-000462	J06404218+0933374	223976028	10.76 ± 0.03	10.28 ± 0.03	9.84 ± 0.02	9.05 ± 0.00	8.79 ± 0.00	8.30 ± 0.00	7.60 ± 0.01	2.80 ± 0.01	flat	G0	7.30	N
CSI Mon-000469	J06404114+0933578	602083890	13.12 ± 0.02	12.25 ± 0.02	11.45 ± 0.02	10.66 ± 0.00	10.14 ± 0.00	9.74 ± 0.00	9.01 ± 0.01	6.04 ± 0.05	II	K7	236.50	N
CSI Mon-000470	J06404424+0953393	602095747	13.79 ± 0.03	13.10 ± 0.04	12.85 ± 0.04	12.56 ± 0.01	12.38 ± 0.01	12.17 ± 0.05	11.79 ± 0.09	...	II/III	>M4	...	N
CSI Mon-000474*	J06410682+0927322	603396438	10.43 ± 0.03	9.53 ± 0.03	8.86 ± 0.03	8.13 ± 0.00	7.65 ± 0.00	7.25 ± 0.00	6.41 ± 0.00	3.42 ± 0.00	II	G	104.70	N
CSI Mon-000491*	J06405616+0936309	616895873	11.89 ± 0.02	10.82 ± 0.02	10.05 ± 0.02	8.94 ± 0.00	8.50 ± 0.00	7.92 ± 0.00	6.91 ± 0.00	3.97 ± 0.02	II	K3	67.20	N
CSI Mon-000498	J06404750+0949289	616849574	11.55 ± 0.07	10.71 ± 0.05	10.08 ± 0.05	9.44 ± 0.00	9.17 ± 0.00	8.93 ± 0.01	8.16 ± 0.03	4.81 ± 0.03	II	K3	12.80	N
CSI Mon-000510	J06410429+0924521	602079845	12.72 ± 0.02	11.93 ± 0.02	11.46 ± 0.02	10.77 ± 0.00	10.28 ± 0.00	9.89 ± 0.00	9.00 ± 0.00	5.65 ± 0.03	II	M0	101.80	N
CSI Mon-000525	J06405118+0944461	223978308	10.74 ± 0.02	10.23 ± 0.02	9.67 ± 0.03	8.72 ± 0.00	8.36 ± 0.00	8.05 ± 0.00	7.55 ± 0.01	4.57 ± 0.06	II	G0	3.50	N
CSI Mon-000530	J06411938+0921469	602075358	13.77 ± 0.03	13.25 ± 0.03	13.23 ± 0.04	13.17 ± 0.01	13.13 ± 0.01	12.80 ± 0.09	12.10 ± 0.26	...	II/III	...	...	N
CSI Mon-000558	J06413974+0940279	223990964	11.34 ± 0.02	10.57 ± 0.02	10.07 ± 0.02	9.39 ± 0.00	9.12 ± 0.00	8.93 ± 0.00	8.12 ± 0.00	4.82 ± 0.01	II	K4	52.50	N
CSI Mon-000566	J06405275+0943004	400007955	14.32 ± 0.04	13.59 ± 0.04	13.28 ± 0.04	12.82 ± 0.02	12.58 ± 0.01	12.14 ± 0.08	11.13 ± 0.16	...	II	M3.5	19.40	N
CSI Mon-000567*	J06405639+0935533	616919752	12.77 ± 0.03	11.79 ± 0.02	11.02 ± 0.02	10.13 ± 0.00	9.66 ± 0.00	9.29 ± 0.00	8.59 ± 0.01	4.88 ± 0.03	II	K3	84.10	N
CSI Mon-000577	J06414382+0940500	616895846	12.05 ± 0.03	11.26 ± 0.03	10.69 ± 0.03	10.07 ± 0.00	9.81 ± 0.00	9.57 ± 0.00	8.84 ± 0.00	5.95 ± 0.03	II	K1	5.90	N
CSI Mon-000586	J06405799+0941314	605538448	15.10 ± 0.05	14.40 ± 0.05	14.16 ± 0.06	13.68 ± 0.01	13.40 ± 0.02	13.31 ± 0.09	12.87 ± 0.22	...	II/III	...	10.70	N
CSI Mon-000590*	J06405891+0928528	603396403	13.00 ± 0.03	12.30 ± 0.02	12.05 ± 0.03	11.77 ± 0.00	11.59 ± 0.00	11.34 ± 0.02	10.89 ± 0.05	...	II/III	M1	17.80	N
CSI Mon-000598	J06405932+0946165	616872597	12.78 ± 0.02	11.92 ± 0.03	11.51 ± 0.02	10.71 ± 0.00	10.48 ± 0.00	10.20 ± 0.01	9.63 ± 0.04	6.08 ± 0.06	II	M1	22.70	N
CSI Mon-000613	J06410577+0948174	616849463	12.02 ± 0.02	11.26 ± 0.02	10.80 ± 0.03	10.14 ± 0.00	9.84 ± 0.00	9.62 ± 0.00	8.89 ± 0.01	6.08 ± 0.04	II	K6.5	30.10	N
CSI Mon-000617	J06410948+0951500	602095761	12.34 ± 0.02	11.63 ± 0.03	11.41 ± 0.03	11.23 ± 0.00	11.14 ± 0.00	11.02 ± 0.01	10.61 ± 0.04	8.05 ± 0.19	II	M3	2.20	N
CSI Mon-000619	J06411475+0934134	603402479	13.87 ± 0.03	12.70 ± 0.03	11.80 ± 0.03	10.34 ± 0.00	9.91 ± 0.00	9.52 ± 0.00	8.83 ± 0.01	5.81 ± 0.03	II	K8.5	94.30	Y
CSI Mon-000631	J06410587+0922556	223982068	10.55 ± 0.02	10.15 ± 0.02	9.57 ± 0.02	8.58 ± 0.00	8.02 ± 0.00	7.35 ± 0.00	5.88 ± 0.00	3.21 ± 0.00	II	...	...	N
CSI Mon-000636	J06404884+0943256	616872578	13.33 ± 0.03	12.28 ± 0.03	11.71 ± 0.02	10.48 ± 0.00	9.92 ± 0.00	9.40 ± 0.01	8.51 ± 0.03	6.31 ± 0.08	II	M0	15.50	N
CSI Mon-000637	J06404921+0957387	616826638	13.57 ± 0.03	12.74 ± 0.04	12.37 ± 0.04	12.15 ± 0.00	12.11 ± 0.01	12.06 ± 0.03	12.13 ± 0.12	6.67 ± 0.06	II	M1	50.80	N
CSI Mon-000638	J06410456+0954438	602266765	9.52 ± 0.02	9.26 ± 0.02	8.91 ± 0.03	8.12 ± 0.00	7.61 ± 0.00	7.18 ± 0.00	6.34 ± 0.00	4.56 ± 0.03	II		...	N
CSI Mon-000650	J06410098+0932444	223980807	10.58 ± 0.02	9.71 ± 0.02	9.21 ± 0.02	8.26 ± 0.00	8.07 ± 0.00	7.80 ± 0.00	7.14 ± 0.00	4.50 ± 0.03	II	K1	6.40	N
CSI Mon-000654*	J06405949+0929517	616943997	13.26 ± 0.03	12.45 ± 0.03	12.09 ± 0.02	11.46 ± 0.00	11.11 ± 0.00	10.82 ± 0.01	9.75 ± 0.02	6.71 ± 0.12	II	M3	26.20	Y

Table 3
(Continued)

Object	2MASS ID	*CoRoT* ID	J	H	K	[3.6]	[4.5]	[5.8]	[8.0]	[24]	Class	SpT	Hα	Comp?
CSI Mon-000660*	J06410051+0929159	223980693	12.44 ± 0.03	11.65 ± 0.03	11.22 ± 0.02	10.50 ± 0.00	10.24 ± 0.00	10.01 ± 0.01	9.62 ± 0.02	8.53 ± 0.31	II/III	K4	16.60	N
CSI Mon-000667	J06412878+0938388	223987997	12.10 ± 0.02	11.55 ± 0.02	11.39 ± 0.02	10.73 ± 0.00	10.36 ± 0.00	9.92 ± 0.00	8.71 ± 0.00	5.22 ± 0.02	II	...	...	N
CSI Mon-000676	J06414780+0934096	223993199	12.06 ± 0.02	11.37 ± 0.02	11.15 ± 0.03	11.05 ± 0.00	10.93 ± 0.00	10.68 ± 0.01	9.81 ± 0.00	5.71 ± 0.01	II	...	...	N
CSI Mon-000681	J06413111+0926582	603808965	11.50 ± 0.03	10.69 ± 0.02	10.12 ± 0.02	9.29 ± 0.00	9.03 ± 0.00	8.66 ± 0.00	8.05 ± 0.02	5.31 ± 0.05	II	...	25.90	N
CSI Mon-000697	J06413455+0936325	223989567	13.71 ± 0.03	13.00 ± 0.02	12.81 ± 0.02	12.57 ± 0.00	12.56 ± 0.01	12.38 ± 0.02	11.84 ± 0.06	7.47 ± 0.12	II	M1	4.50	N
CSI Mon-000717	J06411511+0926443	616943877	13.00 ± 0.03	12.06 ± 0.02	11.60 ± 0.02	11.12 ± 0.00	10.82 ± 0.00	10.59 ± 0.01	9.86 ± 0.03	6.28 ± 0.13	II	M0.5	24.50	N
CSI Mon-000723	J06405254+0950585	616849436	14.19 ± 0.04	13.45 ± 0.03	13.23 ± 0.03	13.02 ± 0.01	12.96 ± 0.01	12.74 ± 0.10	11.96 ± 0.26	...	II/III	...	...	N
CSI Mon-000733	J06404982+0947309	616872582	12.28 ± 0.02	11.72 ± 0.02	11.43 ± 0.02	11.20 ± 0.01	11.07 ± 0.01	10.81 ± 0.11	9.67 ± 0.21	...	II/III	M4	2.10	N
CSI Mon-000753	J06410597+0939142	616895898	13.73 ± 0.03	13.12 ± 0.03	12.74 ± 0.03	12.29 ± 0.00	11.99 ± 0.00	11.57 ± 0.01	10.81 ± 0.01	8.36 ± 0.10	II	M5	7.40	N
CSI Mon-000765	J06405363+0933247	223978921	12.35 ± 0.03	11.68 ± 0.02	11.32 ± 0.02	10.80 ± 0.00	10.60 ± 0.00	10.40 ± 0.01	10.19 ± 0.05	6.92 ± 0.07	II	K1	18.20	N
CSI Mon-000766	J06404837+0948385	602095741	13.43 ± 0.02	12.29 ± 0.03	11.47 ± 0.03	10.79 ± 0.01	10.32 ± 0.00	10.06 ± 0.04	9.30 ± 0.09	5.66 ± 0.12	II	M0.5	70.10	N
CSI Mon-000771	J06411827+0933535	223985261	12.49 ± 0.02	11.84 ± 0.02	11.61 ± 0.02	11.50 ± 0.00	11.40 ± 0.00	11.40 ± 0.01	10.99 ± 0.03	5.47 ± 0.04	II	K4	28.90	N
CSI Mon-000774*	J06405884+0930573	223980264	11.72 ± 0.03	10.95 ± 0.03	10.51 ± 0.02	9.95 ± 0.00	9.69 ± 0.00	9.50 ± 0.00	8.53 ± 0.01	5.51 ± 0.03	II	K2.5	14.30	N
CSI Mon-000804	J06405571+0951138	616849440	12.87 ± 0.02	12.20 ± 0.03	12.01 ± 0.03	11.80 ± 0.01	11.45 ± 0.00	10.71 ± 0.04	9.55 ± 0.07	6.48 ± 0.19	II	K5.5	8.00	N
CSI Mon-000808*	J06405159+0928445	603396401	12.99 ± 0.03	12.20 ± 0.02	11.79 ± 0.03	11.30 ± 0.00	11.06 ± 0.00	11.08 ± 0.01	10.36 ± 0.03	6.73 ± 0.04	II	K4	50.20	N
CSI Mon-000811	J06404321+0947072	605538574	12.80 ± 0.04	12.09 ± 0.04	11.64 ± 0.05	10.79 ± 0.03	10.44 ± 0.02	9.88 ± 0.17	9.29 ± 0.52	5.12 ± 0.21	II	K6	27.10	N
CSI Mon-000876	J06411212+0929521	616944031	13.66	12.95	...	11.51 ± 0.07	10.85 ± 0.08	10.03 ± 0.19	8.78 ± 0.22	...	I	...	2.80	N
CSI Mon-000877	J06411678+0927301	616943883	12.65 ± 0.03	11.88 ± 0.03	11.50 ± 0.03	11.10 ± 0.00	10.82 ± 0.00	10.63 ± 0.01	10.13 ± 0.03	7.17 ± 0.16	II	K4	91.40	N
CSI Mon-000879	J06410338+0940448	603408580	12.93 ± 0.03	12.24 ± 0.03	12.07 ± 0.02	11.94 ± 0.00	11.87 ± 0.00	11.82 ± 0.02	11.78 ± 0.06	6.82 ± 0.05	II	M1	16.50	Y
CSI Mon-000914*	J06405191+0937558	602087948	14.37 ± 0.04	13.62 ± 0.03	12.89 ± 0.03	11.78 ± 0.00	11.13 ± 0.00	9.52 ± 0.00	7.81 ± 0.00	3.17 ± 0.00	I	...	...	N
CSI Mon-000919	J06411329+0931503	616919654	12.74 ± 0.03	12.03 ± 0.02	11.68 ± 0.03	11.02 ± 0.00	10.61 ± 0.00	10.15 ± 0.01	9.38 ± 0.01	6.67 ± 0.06	II	M4	79.90	N
CSI Mon-000928	J06412562+0934429	223987178	13.06 ± 0.02	12.39 ± 0.02	12.10 ± 0.03	11.45 ± 0.00	11.15 ± 0.00	10.73 ± 0.01	9.95 ± 0.01	7.11 ± 0.07	II	M0	15.90	N
CSI Mon-000936*	J06410715+0927294	605538236	...	...	...	10.64 ± 0.01	10.18 ± 0.01	9.60 ± 0.01	8.60 ± 0.02	5.79 ± 0.06	II	...	42.80	N
CSI Mon-000937	J06405255+0952059	603809175	12.69 ± 0.02	11.97 ± 0.02	11.72 ± 0.03	11.47 ± 0.00	11.35 ± 0.00	11.32 ± 0.02	11.02 ± 0.05	7.19 ± 0.28	II	K7	6.90	N
CSI Mon-000945	J06404989+0936494	223977953	12.40 ± 0.03	11.61 ± 0.03	11.16 ± 0.02	10.55 ± 0.00	10.20 ± 0.00	9.97 ± 0.01	9.24 ± 0.02	6.11 ± 0.07	II	K4	66.30	N
CSI Mon-000946	J06404840+0959392	616826633	14.71 ± 0.05	14.13 ± 0.06	13.81 ± 0.07	13.40 ± 0.01	13.25 ± 0.01	12.92 ± 0.05	10.60 ± 0.05	7.67 ± 0.15	II	G0	...	N
CSI Mon-000949	J06411182+0923325	616969729	14.04 ± 0.03	13.37 ± 0.03	13.07 ± 0.04	12.93 ± 0.02	12.91 ± 0.01	12.55 ± 0.13	11.52 ± 0.30	...	II/III	M3	3.60	N
CSI Mon-000951	J06411792+0929011	602079852	13.33 ± 0.03	12.30 ± 0.02	11.85 ± 0.02	11.22 ± 0.00	10.69 ± 0.01	10.32 ± 0.02	9.30 ± 0.02	6.04 ± 0.12	II	M2.5	231.40	N
CSI Mon-000954	J06410734+0925549	603396405	12.59 ± 0.07	11.95 ± 0.05	11.68 ± 0.05	11.48 ± 0.01	11.35 ± 0.01	11.13 ± 0.03	10.28 ± 0.05	...	II/III	K4	1.70	N
CSI Mon-000985	J06401515+1001578	223969098	14.55 ± 0.04	13.25 ± 0.03	12.35 ± 0.03	10.93 ± 0.00	10.62 ± 0.00	10.43 ± 0.01	9.89 ± 0.01	7.19 ± 0.02	II	...	...	N
CSI Mon-000996	J06404131+0951023	616849542	12.81 ± 0.03	12.02 ± 0.02	11.71 ± 0.02	10.90 ± 0.00	10.55 ± 0.00	10.22 ± 0.03	9.44 ± 0.07	6.10 ± 0.13	II	K7	24.50	N
CSI Mon-001003	J06402564+0959597	616803611	13.93 ± 0.03	13.13 ± 0.03	12.65 ± 0.03	12.12 ± 0.00	11.81 ± 0.00	11.20 ± 0.01	10.47 ± 0.02	7.85 ± 0.04	II	M4	157.00	N
CSI Mon-001005	J06400522+0950565	616849610	13.19 ± 0.02	12.48 ± 0.02	12.26 ± 0.02	11.95 ± 0.00	11.82 ± 0.00	11.52 ± 0.03	11.19 ± 0.07	...	II/III	...	...	N
CSI Mon-001017	J06402373+0955238	223971383	13.12 ± 0.03	12.26 ± 0.02	11.81 ± 0.02	11.11 ± 0.00	10.60 ± 0.00	10.35 ± 0.01	9.62 ± 0.03	6.49 ± 0.08	II	...	80.60	N
CSI Mon-001022	J06403911+0950586	616849543	12.29 ± 0.03	11.25 ± 0.02	10.51 ± 0.02	9.64 ± 0.00	9.20 ± 0.00	8.96 ± 0.01	8.38 ± 0.04	5.51 ± 0.08	II	K4	46.50	N
CSI Mon-001031	J06404005+0935029	616919878	12.24 ± 0.03	11.58 ± 0.04	11.25 ± 0.03	10.52 ± 0.00	10.24 ± 0.00	9.91 ± 0.02	8.74 ± 0.03	5.17 ± 0.04	II	K4	7.00	N
CSI Mon-001037	J06403086+0934405	223973200	12.69 ± 0.02	11.51 ± 0.02	10.67 ± 0.02	9.54 ± 0.00	9.20 ± 0.00	8.92 ± 0.00	8.22 ± 0.01	5.34 ± 0.03	II	K1	22.20	N
CSI Mon-001038	J06402262+0949462	602095739	13.88 ± 0.03	13.12 ± 0.03	12.87 ± 0.03	11.85 ± 0.00	11.37 ± 0.00	11.08 ± 0.02	10.86 ± 0.06	...	II	M0	2.70	N
CSI Mon-001048	J06400266+0935242	616919938	13.70 ± 0.03	12.99 ± 0.03	12.71 ± 0.03	12.27 ± 0.00	11.97 ± 0.00	11.55 ± 0.01	10.76 ± 0.02	8.15 ± 0.06	II	...	...	N
CSI Mon-001053	J06404113+0952565	602095745	12.53 ± 0.03	11.77 ± 0.02	11.25 ± 0.02	10.22 ± 0.00	9.74 ± 0.00	9.24 ± 0.00	8.51 ± 0.03	6.20 ± 0.16	II	K6	32.40	N
CSI Mon-001054	J06403652+0950456	400007538	12.93 ± 0.03	12.14 ± 0.03	11.71 ± 0.03	11.07 ± 0.00	10.68 ± 0.00	10.26 ± 0.03	9.55 ± 0.07	5.87 ± 0.07	II	M2	21.10	N
CSI Mon-001059	J06402063+0940499	616895951	13.50 ± 0.02	12.78 ± 0.02	12.41 ± 0.02	11.93 ± 0.01	11.61 ± 0.00	11.28 ± 0.04	10.57 ± 0.09	7.17 ± 0.17	II	...	...	N
CSI Mon-001061	J06402416+0934124	616919835	13.47 ± 0.02	12.52 ± 0.03	11.84 ± 0.02	11.12 ± 0.00	10.65 ± 0.00	10.25 ± 0.00	9.32 ± 0.01	6.45 ± 0.03	II	M0	20.10	N

Table 3
(Continued)

Object	2MASS ID	*CoRoT* ID	J	H	K	[3.6]	[4.5]	[5.8]	[8.0]	[24]	Class	SpT	Hα	Comp?
CSI Mon-001064	J06403518+0951567	616849538	12.61 ± 0.02	11.83 ± 0.02	11.47 ± 0.02	11.08 ± 0.01	10.74 ± 0.00	10.20 ± 0.05	9.19 ± 0.09	5.55 ± 0.05	II	M1	16.40	N
CSI Mon-001076	J06403819+0929524	605424384	13.93 ± 0.03	13.19 ± 0.03	12.89 ± 0.03	12.48 ± 0.00	12.29 ± 0.00	12.02 ± 0.02	11.28 ± 0.02	8.57 ± 0.07	II	M1	2.60	N
CSI Mon-001085	J06403280+0951293	223973692	12.68 ± 0.03	12.00 ± 0.03	11.79 ± 0.02	11.66 ± 0.02	11.58 ± 0.01	11.33 ± 0.20	10.45 ± 0.50	...	II/III	K6	2.70	N
CSI Mon-001094	J06403164+0948233	603420177	13.02 ± 0.03	12.35 ± 0.03	12.18 ± 0.02	12.07 ± 0.01	11.91 ± 0.01	11.90 ± 0.08	11.10 ± 0.15	6.19 ± 0.14	II	K5	54.60	N
CSI Mon-001099	J06404136+0954138	223975844	11.64 ± 0.03	10.95 ± 0.02	10.43 ± 0.02	9.70 ± 0.00	9.35 ± 0.00	9.00 ± 0.00	8.40 ± 0.00	6.98 ± 0.06	II	G1	12.20	N
CSI Mon-001100	J06403934+0934455	616919877	12.65 ± 0.02	11.14 ± 0.03	9.95 ± 0.02	7.98 ± 0.00	7.37 ± 0.00	6.73 ± 0.00	5.84 ± 0.00	2.39 ± 0.01	flat	K6	57.20	N
CSI Mon-001112	J06401867+0952420	616849655	14.04 ± 0.03	13.24 ± 0.03	12.89 ± 0.03	12.63 ± 0.01	12.54 ± 0.01	12.27 ± 0.08	11.42 ± 0.18	...	II/III	...	...	N
CSI Mon-001114	J06393339+0952017	223957142	12.63 ± 0.02	11.90 ± 0.02	11.66 ± 0.02	11.49 ± 0.00	11.46 ± 0.00	11.42 ± 0.01	10.91 ± 0.01	7.49 ± 0.03	II	M1.5	...	N
CSI Mon-001131	J06393441+0954512	223957455	12.99 ± 0.02	12.22 ± 0.02	11.93 ± 0.02	11.49 ± 0.00	11.15 ± 0.00	10.89 ± 0.01	10.19 ± 0.01	7.00 ± 0.04	II	...	...	N
CSI Mon-001132	J06402587+0950576	602095740	13.85 ± 0.03	13.07 ± 0.02	12.60 ± 0.02	11.43 ± 0.01	10.86 ± 0.00	10.45 ± 0.03	9.90 ± 0.09	6.68 ± 0.35	II	M2.5	166.00	N
CSI Mon-001140	J06394147+0946196	223959618	12.57 ± 0.03	11.92 ± 0.02	11.69 ± 0.02	11.36 ± 0.00	11.28 ± 0.00	11.26 ± 0.01	10.93 ± 0.02	5.82 ± 0.01	II	...	...	N
CSI Mon-001142	J06403446+0935182	616919870	13.55 ± 0.02	12.82 ± 0.02	12.53 ± 0.03	12.08 ± 0.01	11.92 ± 0.01	11.63 ± 0.02	11.24 ± 0.03	...	II/III	M2	10.90	N
CSI Mon-001144	J06402309+0927423	223971231	13.15 ± 0.02	12.31 ± 0.02	11.77 ± 0.02	11.01 ± 0.00	10.58 ± 0.00	10.44 ± 0.00	9.94 ± 0.01	7.22 ± 0.04	II	K5	49.50	N
CSI Mon-001149	J06403059+0950147	603420176	12.75 ± 0.03	11.67 ± 0.03	11.19 ± 0.02	10.62 ± 0.00	10.31 ± 0.00	9.91 ± 0.01	9.29 ± 0.02	7.06 ± 0.17	II	M3	33.90	Y
CSI Mon-001157	J06402009+0928285	223970440	13.15 ± 0.03	12.50 ± 0.03	12.24 ± 0.03	11.90 ± 0.00	11.61 ± 0.00	11.14 ± 0.01	10.12 ± 0.01	6.80 ± 0.04	II	...	3.20	N
CSI Mon-001167	J06403787+0934540	400007528	12.91 ± 0.02	12.19 ± 0.03	11.83 ± 0.02	11.35 ± 0.00	11.07 ± 0.00	10.90 ± 0.03	10.36 ± 0.07	7.45 ± 0.17	II	M3	23.40	N
CSI Mon-001171	J06393398+0949208	223957322	13.04 ± 0.02	12.27 ± 0.02	12.09 ± 0.02	12.08 ± 0.00	12.05 ± 0.00	11.94 ± 0.01	11.64 ± 0.02	6.76 ± 0.02	II	K7	...	N
CSI Mon-001174	J06401370+0956305	616826810	12.92 ± 0.03	12.13 ± 0.02	11.58 ± 0.02	10.64 ± 0.00	9.98 ± 0.00	9.27 ± 0.00	8.10 ± 0.00	5.38 ± 0.03	II	M2	130.20	N
CSI Mon-001181	J06401801+0950220	616849652	14.03 ± 0.03	13.33 ± 0.03	13.04 ± 0.03	12.80 ± 0.01	12.71 ± 0.01	12.43 ± 0.06	11.75 ± 0.17	...	II/III	M2	12.07	N
CSI Mon-001187	J06401417+0934283	602083884	13.75 ± 0.03	12.96 ± 0.03	12.59 ± 0.03	11.94 ± 0.00	11.56 ± 0.00	11.28 ± 0.01	10.51 ± 0.03	7.42 ± 0.05	II	...	8.00	Y
CSI Mon-001197	J06402616+0937092	603408572	14.23 ± 0.04	13.52 ± 0.03	13.30 ± 0.05	12.87 ± 0.01	12.47 ± 0.01	12.08 ± 0.03	11.32 ± 0.06	8.60 ± 0.33	II	...	...	N
CSI Mon-001199	J06404184+0951445	602095746	12.75 ± 0.03	11.85 ± 0.04	10.98 ± 0.05	9.67 ± 0.00	9.37 ± 0.00	8.98 ± 0.01	8.55 ± 0.05	6.03 ± 0.22	II	K5	22.90	N
CSI Mon-001205	J06402881+0948240	400007344	13.08 ± 0.03	12.40 ± 0.04	12.19 ± 0.03	11.98 ± 0.00	12.00 ± 0.01	11.96 ± 0.07	11.24 ± 0.19	...	II/III	...	...	N
CSI Mon-001217	J06403665+0952032	616849540	12.73 ± 0.03	11.76 ± 0.03	11.10 ± 0.02	10.01 ± 0.01	9.45 ± 0.00	8.98 ± 0.04	8.03 ± 0.09	4.36 ± 0.10	flat	K4	87.00	N
CSI Mon-001219	J06402744+0952303	616849516	14.32 ± 0.03	13.63 ± 0.02	13.36 ± 0.04	13.16 ± 0.01	13.13 ± 0.01	12.83 ± 0.14	11.99 ± 0.34	...	II/III	...	6.80	N
CSI Mon-001221	J06402342+0954555	616826682	14.01 ± 0.04	13.35 ± 0.04	12.97 ± 0.04	12.28 ± 0.01	12.01 ± 0.01	11.83 ± 0.03	11.40 ± 0.06	7.56 ± 0.14	II	...	32.10	N
CSI Mon-001223	J06400600+0949426	616849613	13.46 ± 0.03	12.76 ± 0.03	12.45 ± 0.03	12.04 ± 0.00	11.73 ± 0.00	11.31 ± 0.03	10.64 ± 0.07	6.82 ± 0.20	II	M2	4.27	N
CSI Mon-001234	J06401113+0938059	223968039	12.95 ± 0.03	12.12 ± 0.03	11.61 ± 0.03	10.91 ± 0.00	10.60 ± 0.00	10.32 ± 0.01	9.53 ± 0.01	6.65 ± 0.09	II	K6	52.90	N
CSI Mon-001240	J06402639+0956588	616826701	14.52 ± 0.03	13.89 ± 0.04	13.50 ± 0.05	12.87 ± 0.00	12.40 ± 0.00	11.98 ± 0.02	11.31 ± 0.05	8.62 ± 0.79	II	>M4	72.00	N
CSI Mon-001249	J06402027+0956063	616826670	12.30 ± 0.03	11.52 ± 0.03	11.21 ± 0.02	10.64 ± 0.00	10.18 ± 0.00	9.62 ± 0.00	8.72 ± 0.01	5.72 ± 0.04	II	M3	33.50	N
CSI Mon-001294	J06400552+0922260	616970063	13.95 ± 0.03	13.12 ± 0.02	12.73 ± 0.03	12.14 ± 0.00	11.96 ± 0.00	11.66 ± 0.01	11.02 ± 0.01	8.24 ± 0.04	II	...	31.20	N
CSI Mon-001308	J06395924+0927245	223964667	13.23 ± 0.03	12.46 ± 0.02	12.06 ± 0.02	11.78 ± 0.00	11.63 ± 0.00	11.42 ± 0.01	10.94 ± 0.01	6.66 ± 0.02	II	...	...	N
CSI Mon-006491	J06392550+0931394	616920065	13.77 ± 0.03	12.86 ± 0.03	12.38 ± 0.02	11.73 ± 0.00	11.44 ± 0.00	11.15 ± 0.01	10.52 ± 0.01	7.86 ± 0.03	II	...	...	N

Notes. We have assembled a list of NGC 2264 region members, candidates, and field stars, called the CSI Mon catalog. Here we show only the Mon identification numbers of objects discussed in this paper. The *CoRoT* IDs are from the SRa05 run. Hα refers to the equivalent width of the Hα emission line, and we adopt the values of Rebull et al. (2002) and Dahm & Simon (2005). Spectral types are from Walker (1956), Makidon et al. (2004), and Dahm & Simon (2005). Objects with the disk class II/III have a Class III SED based on the slope, but have significant evidence of a weak disk based on their [3.6] − [8.0] colors. The "comp" column denotes whether the object appears to have a companion within 1″ ("Y" if yes). Detection is based on visual binarity or elongation of the point-spread function reported by Sung et al. (2009), or spectroscopic indications of binarity via variable radial velocity measured by Fűrész et al. (2006). Objects with no known companion ("N") may still be undetected binaries. *Objects with IRAC staring data are marked with asterisks.

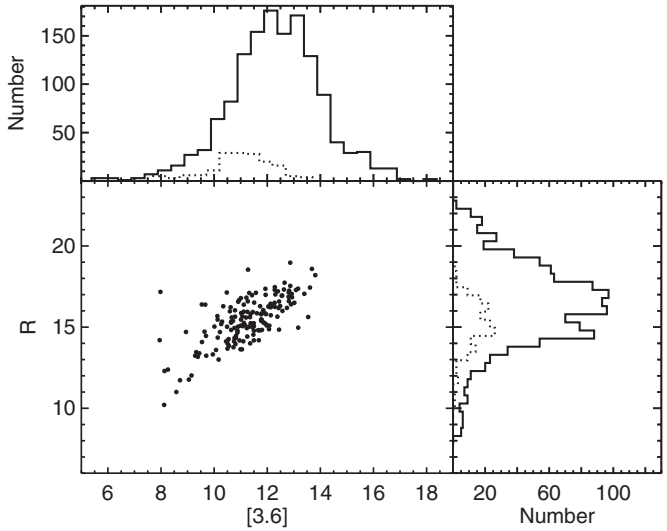

Figure 2. We present the distributions of 3.6 μm and *R*-band magnitudes characterizing our disk-bearing sample, shown as dotted histograms. The solid histograms show the distributions of all ∼1500 confirmed cluster members in these bands.

2.2. Overall Sample Properties

The full sample of ∼1500 cluster members in NGC 2264 includes spectral types ranging from M5 to A7 (Walker 1956; Makidon et al. 2004; Dahm & Simon 2005), corresponding to masses of ∼0.1 $M_{\odot}$ to several $M_{\odot}$. Restricting this to the 162 disk-bearing objects among the IRAC and *CoRoT* targets, the spectral types run from M5 to G0. We present the distributions of brightness in *CoRoT* and IRAC bands for this disk-bearing sample in Figure 2. Both the spectral type and *R* magnitude distributions are representative of the cluster sample as a whole. However, the collection of 3.6 μm points is skewed considerably toward brighter values than compared to the available infrared data set. This is because the requirement of *CoRoT* observations eliminates most faint and embedded objects from the set. We have also produced color–magnitude diagrams to compare the 162-object sample with the distributions of field stars and other cluster members; these are presented in Figure 3.

The pixel sizes for *Spitzer*/IRAC and *CoRoT* are 1.″2 and 2.″3, respectively. We are therefore unable to separate some visual binaries. However, thanks to the higher spatial resolution of previous ground-based data sets (i.e., Sung et al. 2008), we have a fairly complete list in Table 3 of blended objects. The effect of binarity on variability will need to be assessed once a more complete multiplicity census is available.

3. IRAC DATA

3.1. Observations

Spitzer has been operating in its Warm Mission mode since the exhaustion of cryogen in mid-2009, and it now observes exclusively in the IRAC 3.6 μm and 4.5 μm channels. Observations of a ∼0.°8 × 0.°8 region of NGC 2264, including the more embedded Cone Nebula and Christmas Tree Cluster regions, were carried out from 2011 December 3 to 2012 January 1 with Warm *Spitzer*/IRAC, under program 80040 (PI: J. Stauffer). The field center was R.A. = $06^{h}40^{m}45\overset{s}{.}0$, decl. = +09°40′40″. Since the cluster is considerably larger than the camera's 5.′2 × 5.′2 FOV for each channel, we visited targets ∼12 times a day with a series of mapping fields. For each such Astronomical Observation Request (AOR), we executed four pointings. Starting at the first position, two exposures were acquired with an 8″ dither to mitigate any detector artifacts or cosmic-ray hits. Total frame time for each was 12 s. Data were taken simultaneously in the two IRAC bands, but due to the non-overlapping IRAC FOVs, individual objects were monitored in one channel at a time. A spatial shift of just over half the field size was then performed, providing a second pair of dithers for half of the targets and a first dither pair for an equivalently sized set of targets in the newly observed section of the FOV. After three telescope offsets, the FOV has advanced by 7.′2, such that targets in the newly observed section of the "trailing" IRAC dectector's FOV will have been observed by the "leading" IRAC detector less than a minute earlier. Accordingly, most of our targets have two-color IRAC data, but for the approximately 40% of objects near the edges of the mapping region, there is only single-channel coverage.

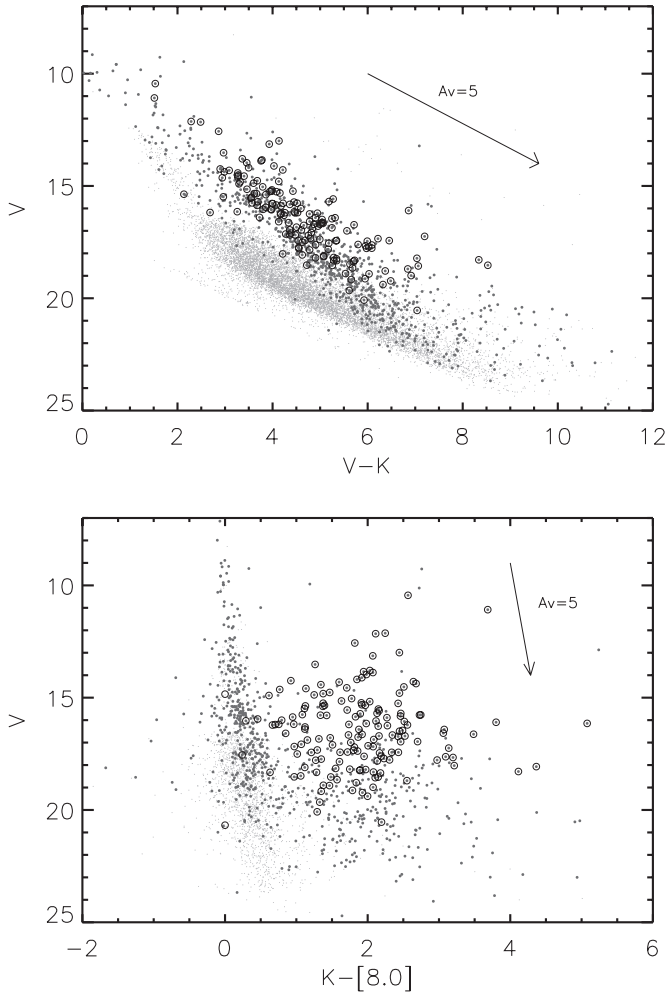

Figure 3. Color–magnitude diagrams, including field stars (light gray points), NGC 2264 members (dark gray dots), and objects in the 162 member disk-bearing data set highlighted in this paper (black circles). The optical/near-infrared diagram at the top indicates that the sample considered here is consistent with a pre-main-sequence track, while the near-infrared/mid-infrared diagram at the bottom confirms that the SED slope selection has resulted in a robust set of infrared-excess objects. The infrared extinction value at 8.0 μm is taken from Indebetouw et al. (2005).

Since stars brighter than magnitude 9.5 saturate the IRAC detector in 12 s exposures, we also acquired 0.6 s integrations of each field. This high dynamic range (HDR) mode was employed during every sixth round of mapping. The resulting observing

cadences were every ∼101 minutes for mapping data and ∼12 hr for the 0.6 s HDR mode data.

To capture light-curve behavior on even shorter timescales, we operated IRAC in staring mode for four blocks of 20, 26, 16, and 19 hr, respectively, toward the beginning of the run (see Table 1 for dates). The channel 1 and 2 FOVs were fixed on a region near the center of NGC 2264, and exposures with 6 s integration times were acquired repeatedly, with no dithering or HDR mode images. After taking readout and data volume restrictions into account, the cadence for staring mode data was ∼15 s. A total of 549 stars were observed in the staring fields. We display these regions, along with the full 3.6 and 4.5 μm FOVs, in Figure 1.

3.2. Light-curve Production

For both the mapping mode and the staring mode data, we used the IDL package Cluster Grinder (Gutermuth et al. 2009) to generate light curves from the BCD images released by the Spitzer Science Center (SSC) pipeline, version S19.1. Each flux-calibrated BCD was processed for standard bright source artifacts. Cluster Grinder delivers mosaics for each AOR, point-source locations, and photometric measurements from the mosaics ("by-mosaic" light curves). We then re-performed photometry on the BCD images using the Cluster Grinder source list, with a 5σ source detection threshold. We applied array-position-dependent systematic corrections for residual gain and pixel-phase effects (although the treatment of this was modified for staring data; see the Appendix). The pipeline also computes a variety of flagging information, including maximum pixel value for saturation detection, spatial coverage, and outlier rejection.

Aperture photometry was obtained from both the BCDs ("by-BCD" photometry) and the mosaics ("by-mosaic" photometry) using an aperture radius of 2.″4 (2 pixels) and a sky annulus from 2.″4 to 7.″2 (2–6 pixels). We also combined the resultant photometric by-BCD measurements into "by-AOR" photometric products, mimicking the cadence of the by-mosaic photometry. We have found that the photometric precision achieved with this approach is higher than that of the by-mosaic data, presumably because the latter does not allow for easy treatment of array-position-dependent systematics, such as residual gain and pixel-phase effects. Hence, we present only the by-BCD light curves (for staring data) and by-AOR light curves (for mapping data) here.

We flagged by-BCD photometry for saturation, low signal-to-noise ratio (S/N < 5), and outlier status (5σ above the median flux of other points in the same AOR). Affected points were omitted from by-AOR photometry, and unaffected points were combined via an unweighted mean. By-AOR photometry values resulting from fewer than three by-BCD measurements were flagged as well. Following these procedures, the majority of mapping mode light curves contain 300–320 valid data points.

For pairs of 0.6 s and 12 s exposures taken during the HDR mode, we selected the latter only if it did not exceed a count level of 20,800 DN (Warm IRAC saturates at ∼30,000 DN); otherwise, the measurements from the 0.6 s exposures were swapped in. For saturated objects brighter than a magnitude of ∼9.5, we retained only the twice daily short HDR exposures, resulting in by-AOR light curves with ∼50 points.

We adopted the standard zero points derived from the official Warm Mission FLUXCONV header values: 19.30 and 18.67 for 1 DN s^{-1} total flux at 3.6 and 4.5 μm, respectively. These values include standard corrections for our chosen aperture and sky annulus sizes (Reach et al. 2005).

Uncertainties for the by-BCD photometry were derived by combining three terms in quadrature: shot noise in the aperture, shot noise in the mean background flux per pixel integrated over the aperture, and the standard deviation of the sky annulus pixels (to account for the influence of non-uniform nebulous background). Finally, the BCD-level photometric uncertainties were combined in quadrature to yield uncertainties for the by-AOR photometry reported here.

To weed out extremely faint sources and artifacts, we required that each light curve contain at least five unflagged data points and have a mean photometric uncertainty of less than 10%. Applying these cuts, we generated a total of 13,856 mapping mode light curves in the 3.6 μm band and 12,186 light curves in the 4.5 μm band, 9541 of which include data in both bands. For our eventual comparison of behavior in the optical and infrared (e.g., Section 7), we performed further cuts and retained only IRAC light curves with at least 30 unsaturated points covering a minimum time span of 20 days. For the subset of observations executed in staring mode, we have additional high-cadence light curves for 290 objects with 3.6 μm band data and 259 objects with 4.5 μm band data. We have also produced binned staring light curves with smaller error bars at 2.5 minute cadence, which we describe below. Since the staring fields were observed simultaneously, there is no overlap between the 3.6 and 4.5 μm sets.

3.3. Mapping Data Quality

Comparison of the rms values for all mapping light curves with their mean predicted uncertainties revealed additional systematic errors that limited the photometric accuracy to 1%, as seen in Figure 4. In order to identify variable stars, we need to characterize the systematic effects as a function of magnitude in detail. Because of the transition to shorter exposure times toward the bright end of the sample, there is an upward bump in the rms distribution near 10th magnitude, and it is difficult to assess the systematic contribution here. We therefore computed a different measure of the systematic, "S," which should be independent of exposure time:

$$S = \sqrt{\mathrm{rms}^2 - \sigma^2}, \quad (1)$$

where σ is the uncertainty estimate described above, without systematics, and rms is the rms deviation of each light curve omitting flagged points. Plotting S against magnitude, we found that the nonvariable stars traced out an exponential trend, with a larger systematic contribution for fainter objects. To omit as many variable objects as possible while characterizing this effect, we considered only stars lacking firm NGC 2264 membership status (see the Appendix for membership evaluation criteria) and computed the median of the distribution of S values in 0.5 mag bins. We then fit an exponential curve of form

$$S(m) = e^{(m-m_0)} + S_0, \quad (2)$$

where m is magnitude and m_0 and S_0 are free parameters in units of magnitude.

The distribution of S values, as well as the fits for each IRAC band, are shown in Figure 5. We obtained best-fitting values of $S_0 = 0.014$, $m_0 = 19.75$ in the 3.6 μm band and $S_0 = 0.008$, $m_0 = 19.28$ in the 4.5 μm band, indicating that the photometry includes systematics at the 1% level. Indeed, this is expected from intrapixel sensitivity variations and detector gain variations, both of which are known to result in position-dependent flux measurements (see the Appendix). As shown in

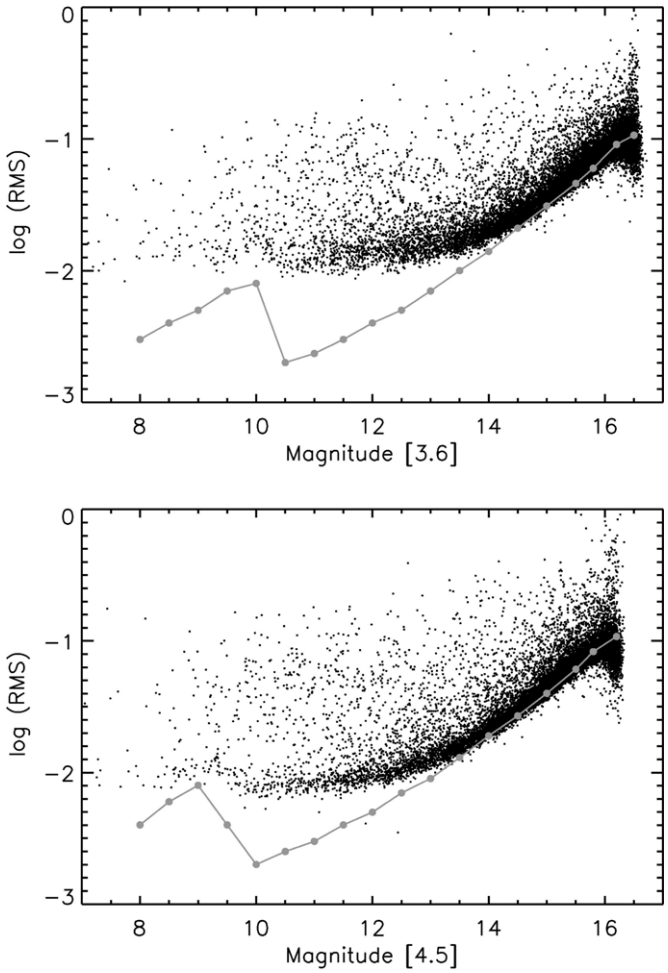

Figure 4. Expected and observed standard deviations of IRAC mapping light curves in channel 1 (top) and channel 2 (bottom), as a function of magnitude. Black points are the measured rms values, while the gray curve marks the estimated 1σ white-noise level in 0.5 mag bins (dots), as predicted by Poisson noise and sky background. The jump near magnitude 10 is due to the shift to shorter exposure times for bright stars observed with short HDR exposures. There is an empirical noise floor that is limited to just under 0.01 mag for the brightest objects. Points with large rms values above the empirical noise floor at each magnitude are predominantly variable cluster members.

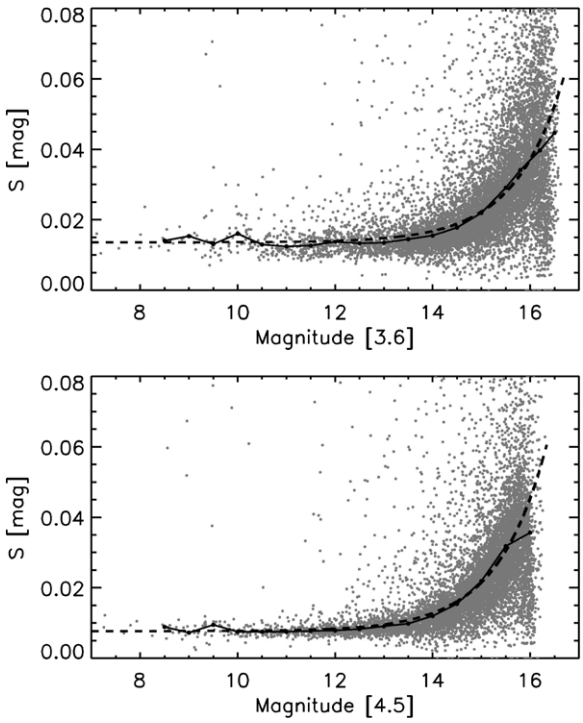

Figure 5. Systematic error ("*S*") as a function of IRAC magnitude, for channel 1 (top) and channel 2 (bottom). Gray points are field stars or objects with uncertain membership, culled by a lack of photometric or spectroscopic signatures of youth. For more information on NGC 2264 membership criteria, see the Appendix. Black circles mark the median trend of *S*, in 0.5 mag bins. The dashed curve represents the best-fit exponential trend.

Figure 5, *S* increases exponentially from ∼0.01 mag for 13th magnitude sources to 0.04 mag for 16th magnitude sources. Figure 4 demonstrates that the expected Poisson noise and sky noise increase from ∼0.01 mag to ∼0.1 mag over the same range of magnitudes. Thus, while both random and systematic uncertainties increase toward faint magnitudes, the systematic effects increase more slowly toward the faint end, such that they dominate the error budget for sources brighter than ∼14th magnitude, with random uncertainties becoming increasingly dominant for fainter sources.

To fully account for the errors, we added the fitted magnitude-dependent systematic offsets in quadrature to the derived uncertainties and adopted the result for the selection of variables and production of variability statistics, as will be discussed in Section 6. In addition, we have performed similar assessments of the staring data. Since those light curves are not presented extensively here, we refer the reader to the appendix for a discussion of their quality and the mapping/staring data merging process.

4. *CoRoT* DATA

The *CoRoT* satellite (Baglin et al. 2006) was launched in 2006 and observed until 2012 November. Consisting of a 27 inch diameter telescope with an external baffle to suppress scattered light from Earthshine, it performs broadband photometric monitoring (∼3700 to 10000 Å) of stars in two 10° diameter regions near the galactic center and anti-center, known as the *CoRoT* "eyes." Observations were originally carried out with two exoplanet-dedicated and two seismology-dedicated CCDs, but by the time of our observations, only one of each was in operation. Data from the exoplanet CCD are passed through low-resolution spectral dispersing prism to produce three-color photometry in approximately "red," "green," and "blue." For most targets, data from these three bands are coadded to generate a white-light curve. For 910 targets (including 262 with *Spitzer* observations), the full chromatic data set was retained. However, we did not use these data at this time as they showed signs of strong systematics as a function of both band and time. In addition to the 2011 observations described here, a prior *CoRoT* short run including many of the same NGC 2264 targets in 2008 provides long time baseline information on optical variability phenomena, including rotation (Affer et al. 2013) and pulsation properties (Zwintz et al. 2011).

4.1. Observations

NGC 2264 is the only rich 1–5 Myr cluster situated within one of the *CoRoT* eyes, making it the primary target for young star variability with this telescope. For the CSI 2264 campaign, we monitored a ∼1.°3 × 1.°3 field in NGC 2264 centered at R.A. = $06^{h}40^{m}18\overset{s}{.}0$, decl. = $+09°41'46\overset{''}{.}24$ (see Figure 1) from 2011 December 1 to 2012 January 9. These observations

composed the fifth *CoRoT* short run ("SRa05"). All stars were placed on the second exoplanet channel CCD (E2), as the first channel ceased to function in early 2009. NGC 2264 was previously observed during the SRa01 short run in 2008, using the first exofield CCD, E1. In each case, targets consisted of confirmed and candidate NGC 2264 members, as well as field objects selected for *CoRoT*'s transiting planet search program. Only data for pre-selected targets are downloaded from the satellite, with photometry consisting of flux values within a predefined aperture mask for each star. For SRa05, we monitored 489 confirmed and 1617 candidate NGC 2264 members, along with an additional 2129 field stars.

Light curves are produced by the *CoRoT* pipeline (Samadi et al. 2006), which performs corrections for gain and zero offset, jitter, and electromagnetic interference, as well as background subtraction. We obtained level N2 reduced data from the *CoRoT* archive, which consists of fully processed light curves. This includes fluxes and background levels, flagged for outliers and hot pixels. Typically ∼10%–15% of these were flagged and omitted from the light curves.

Exposure times were 512 s, resulting in up to ∼6300 data points per light curve. For a subset of stars with signs of eclipses or transits, a high-cadence mode was triggered with 32 s exposure times. This mode generated light curves with up to 100,850 points and was mainly used for stars brighter than 14th magnitude in *R* band.

The full range of magnitudes for observed stars was $R \sim 11$–17. Light-curve rms values ranged from 0.00055 for the brightest stars to 0.01–0.1 for the faintest objects. There is a substantial spread in rms as a function of magnitude, because of strong systematics in a subset of the light curves, which we address below.

We produced light curves from the *CoRoT* data by converting raw fluxes to the magnitude scale and subtracting the median after removal of outliers automatically flagged by the *CoRoT* pipeline. The zero point for *CoRoT* photometry is not well determined and may vary slightly between runs. To estimate a calibration for the SRa05 data set, we compared the logarithmic mean flux with *R*-band photometry reported in the literature by Rebull et al. (2002), Lamm et al. (2004), and Sung et al. (2008). A fit of the intercept results in an *R*-band zero point of 26.74.

The full 2011 *CoRoT* data set on NGC 2264 contains light curves for a total of 4235 objects, just over half of which are field stars, based on the membership criteria outlined in the Appendix. These were included for the transit monitoring portion of the campaign. A total of 2500 of the *CoRoT* targets were previously observed during the SRa01 run in 2008. In total, 1303 stars were observed by both *CoRoT* and *Spitzer*, about 65% of which are possible or likely field stars. All *CoRoT* light curves encompassed the full 39 day campaign.

In general, we performed source cross matching with a 1″ radius. For targets with source confusion within the *CoRoT* mask, we first identified the object in the optical by requiring its *CoRoT* calibrated *R* magnitude to match photometry of a known source to within 0.5 mag. We then identified the 2MASS counterpart and used those coordinates to select the appropriate *Spitzer* source.

4.2. Correction of Light-curve systematics

CoRoT light curves include a number of well-known systematic effects, including outliers and flux discontinuities due to radiation events or changes in detector temperature (Auvergne et al. 2009). Isolated outliers are automatically detected by the *CoRoT* pipeline and flagged in the resulting photometry. Other types of systematics can be removed if the light curves are well behaved or if color data are available (e.g., Mislis et al. 2010). However, correction becomes more difficult in a highly variable, mostly monochromatic data set such as ours.

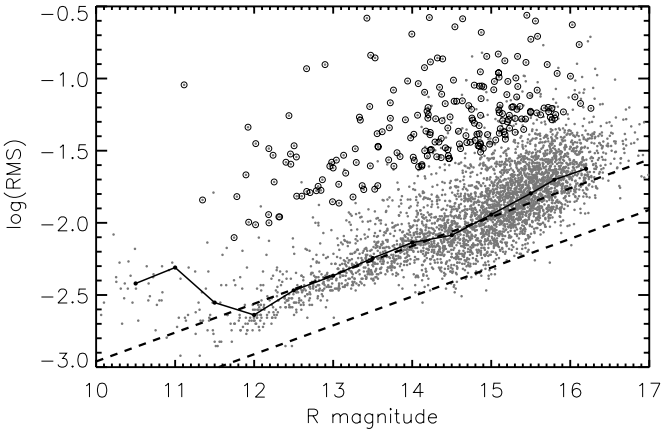

Figure 6. rms values of *CoRoT* light curves, as a function of magnitude. The black points and curve track out the median from 0.5 mag bins. A transition in rms behavior is seen near $R = 14$, as this was the cutoff used to select exposure times. Most objects brighter than $R = 14$ were monitored at high cadence (32 s exposures), while fainter objects were monitored at low cadence (512 s exposures). The bottom dashed line illustrates the estimated Poisson error. We have approximated the median error, including systematics, by shifting this upward by 0.35 in log(rms), as shown with the middle dashed line. We shift this another ∼0.5 dex to select variables (shown as black circles) at the 3σ level.

We found that ∼10% of light curves contained abrupt jumps in flux not attributable to stellar variation. Two prominent discontinuities appeared at the same time stamps in many light curves. These are due to detector temperature jumps, the times of which were provided by the *CoRoT* team. We searched for and corrected discontinuities at these locations by computing a weighted difference between the flux difference on either side of each jump.

Background correction has also introduced time-dependent systematics into the light curves. Background levels are measured as a median across 400 10 × 10 pixel windows placed in star-free regions of the FOV. As the E2 CCD has aged, the level of dark current, as well as its gradient across the detector, has increased. Further complicating background measurements is the intrinsic peak in background due to nebulosity near the NGC 2264 cluster center. As a result, the median background value subtracted from stellar fluxes can be an underestimate for many sources. The combination of these effects, along with the different CCD used to observe NGC 2264 during 2008, has resulted in artificial variability amplitude changes for stars observed in both the SRa01 and SRa05 runs. For well-characterized variables such as eclipsing binaries, we note amplitude differences of up to 10%.

To omit problematic data from variability statistics, we visually inspected all 2011 *CoRoT* light curves and flagged those with discontinuities that were at least a factor of seven times the rms (and often much more). About 10% of light curves received flags.

To assess the noise levels and fit the rms distribution as a function of magnitude, we have plotted the rms values of the entire ∼5000-object *CoRoT* data set versus the magnitude values, using the zero point of 26.74; the result is displayed in Figure 6. For bright objects ($R < 14$), the trend of rms values follows a slope consistent with Poisson noise plus a constant

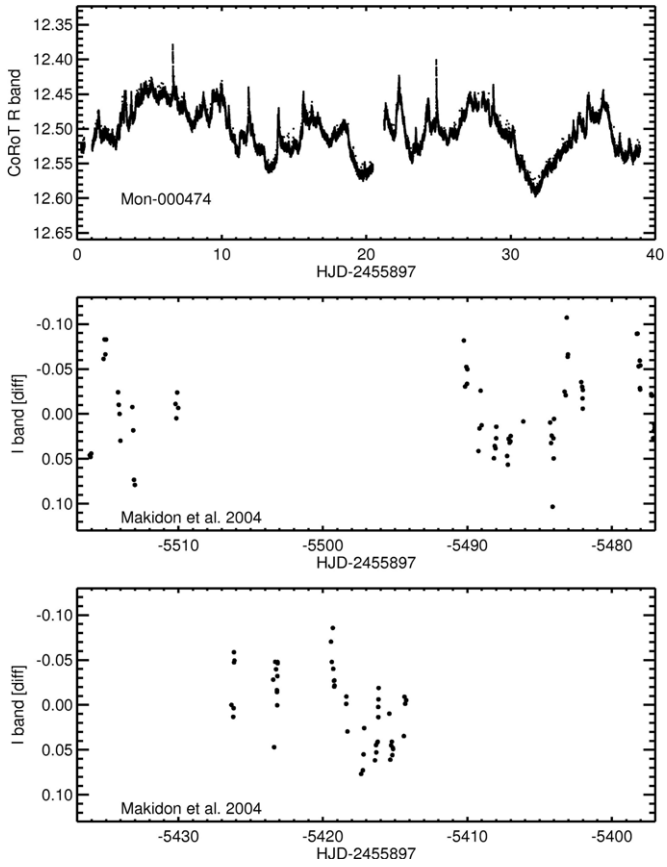

Figure 7. Light curves for Mon-000474, as observed by *CoRoT* from space (top) and Makidon et al. (2004) from the ground (middle, bottom). Short-duration flux increases appear in the high-cadence data but are difficult to discern in ground-based time series.

systematic. The distribution expands to lower values for objects beyond $R = 14$, with some rms values reaching the Poisson limit. This structure in the diagram is related to the change from high to low cadence near $R = 14$ and is not explained by the flagged objects, as these have a large range of rms values at all magnitudes. As seen in the figure, the rms values of the final light curves ranged from 0.001 mag (at $R \sim 11.5$) to 0.04 mag (at $R \sim 17$), with larger amplitudes for variable objects.

5. LIGHT-CURVE MORPHOLOGY CLASSES

The high cadence and precision of our *CoRoT* and *Spitzer* time series data enable an unprecedented window into the diversity of light-curve morphologies. We are able to analyze in detail the patterns and timescales of brightness fluctuations, and in some cases to separate them into multiple components. In comparison with ground-based monitoring results, finer morphological divisions appear in our data set. We provide an example comparison of one of our *CoRoT* light curves with typical ground-based data from Makidon et al. (2004) in Figure 7.

Our own approach to classifying variability in the 162 member disk-bearing *CoRoT*/*Spitzer* data set involves an initial visual classification, followed by statistical confirmation and analysis. As shown in Figure 8, we select variable types based on two parameters: stochasticity (or alternatively, periodicity), and degree of asymmetry in the flux.

For many types of variability mechanisms, we expect morphological properties to correlate with physical processes or

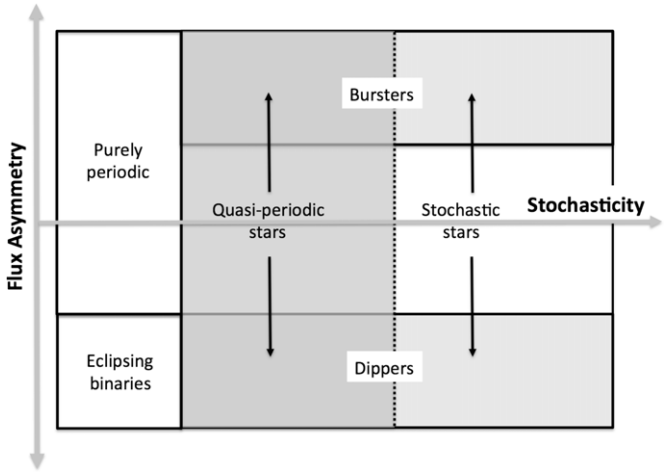

Figure 8. Schematic of the classification system we have applied for optical and infrared variability in the CSI 2264 data set. At the top end of the schematic are light curves preferentially populated with brightening events on top of a continuum, while at the bottom of the schematic are light cruves with fading events. The middle is occupied by variability that is more or less symmetric in flux. Moving from right to left are variables with increasingly stable repeating patterns.

geometry. For example, we expect the fraction of extinction-dominated variables to relate to disk scale height; this was estimated by Bertout (2000) to be ∼15%. In addition, timescales inherent in variability point to mechanisms associated with star or disk rotation, or disk and accretion instabilities. Multiwavelength properties of morphology should also confirm which processes dominate flux changes. For global changes in luminosity (e.g., from accretion), we might expect optical and infrared variations to be correlated; starspots, on the other hand, could induce phase lags at these two wavelengths. In summary, a careful accounting of morphological types can help to verify these assumptions.

In this section, we begin by highlighting progress made by previous campaigns, and then present the categories of variability illustrated in Figure 8, followed by speculation on the physical processes behind them.

5.1. Summary of Previous Classification Schemes

Prior optical and near-infrared YSO variability studies have proposed several different classes of T Tauri star behavior, depending on light-curve morphology, accretion status, and stellar mass. The first general survey of YSO variability was performed by Parenago (1954), who classified T Tauri stars based on histograms of their brightness levels. Objects that were more often bright than faint were referred to as Class I, objects with typical brightness similar to the mean were Class II, and stars that were more often faint than bright were called Class III. Following up on this, Weaver & Frank (1980) explored the relationship between light-curve class and emission line strength, finding that Class I objects were associated with preferentially weak strengths. Later, Herbst et al. (1994) presented a variability classification scheme based on 15 yr of photometric monitoring of 80 young stars. They divided light-curve behavior into four types, including periodic variations caused by cool spots in WTTSs ("type I"), irregular and periodic variations in CTTSs (types "II" and "IIp") attributed to variable accretion luminosity and rotational modulation of hot spots, respectively. In addition, they identified flux changes of 0.8–3 mag in the *V* band among T Tauri stars earlier than

spectral type K1 ("type III"). The mechanism for this behavior was proposed to be obscuration by circumstellar material, since it was not associated with veiling changes. It frequently involves pronounced flux decreases, interpreted as extinction events as in the prototype UX Ori.

A similar scheme was suggested by Alencar et al. (2010) based on higher cadence light curves of T Tauri stars from the first *CoRoT* short run on NGC 2264 in 2008 ("SRa01"). They divided the variability sample into periodic sinusoidal (spot-like), periodic flat topped (AA Tau-like), and aperiodic (irregular). These correspond roughly to the Herbst et al. (1994) classes, except that the AA Tau-type objects have much shorter timescales (a few to 10 days) than the higher mass UX Ori stars.

Further variability studies (e.g., Carpenter et al. 2001; Lamm et al. 2004; Grankin et al. 2007, 2008; Scholz et al. 2009) continued the strategy of dividing variability into periodic and aperiodic and assessing physical mechanisms by analyzing color changes as a function of magnitude. These photometric campaigns typically involved monitoring at lower cadences (days to years) or with many more gaps in time sampling than our own data set. In the case of NGC 2264, Lamm et al. (2004) classified stars only as periodic or irregular, based on periodograms and χ^2 tests. They concluded that variability was likely due to rotational modulation of cool spots (if periodic), or hot spots generated by accretion flows onto the star (if irregular).

5.2. "Dipper" Light Curves

One of the most common phenomena in our time series is transient optical fading events. These have been noted previously in YSOs, from the early-type HAeBe stars (e.g., Herbst & Shevchenko 1999) to lower mass AA Tau stars (e.g., Bouvier et al. 1999). Based on color trends and an inconsistent relationship of photometric behavior with veiling in accompanying spectra, these episodes have been attributed primarily to extinction by circumstellar material (e.g., Bouvier et al. 1999; Alencar et al. 2010). In some cases, the events recur periodically, although their depth changes. Morales-Calderón et al. (2011) identified similar behavior in infrared and near-infrared time series of YSOs in Orion, likewise attributing "dipper" events to stellar occultations by regions of enhanced optical depth in a surrounding dusty disk. In several cases, periodic fading on longer timescales (months to years) has been traced to obscuration by a circumbinary disk precessing about a double- or triple-star system (e.g., Cohen et al. 2003; Plavchan et al. 2008a; Herbst et al. 2010; Plavchan et al. 2013). If the dips are caused by varying dust extinction along the line of sight, then the light curves should become redder as they grow fainter. Bouvier et al. (2003) indeed found this behavior in the prototype AA Tau itself, noting color slopes similar to the values expected from an interstellar medium extinction curve.

Unsurprisingly, prominent fading events appear in our *CoRoT* and *Spitzer* light curves. These are distinguished from other types of variability by both the sharpness and rapidity of the brightness troughs. Outside of these events, the light curves display a "continuum" flux level with less variability. To quantitatively identify and compare dipper behavior in the different bands, we have selected by eye objects that are clearly asymmetric, in that their light curves appear different when flipped upside-down.

We have identified 35 optical and seven infrared dipper stars in the joint *CoRoT*/*Spitzer* disk-bearing sample. Two (Mon-000183 and Mon-000566) exhibit clear dips only in the infrared, although with knowledge of the *Spitzer* data, one can see small dips (2%–3% depth) in the *CoRoT* light curves at the same times. Many of the *optical* dippers, however, are accompanied by entirely different infrared light curves, with high-amplitude, long-timescale variability and little to no sign of dips.

Prominent example light curves are shown in Figures 9–12. In Section 6.2, we introduce criteria to distinguish between periodic, quasi-periodic, and aperiodic light curves. The dipper sample here is split nearly evenly among quasi-periodic and aperiodic behavior, although it is not clear how the physics variability mechanisms differ between the two groups. We find that seventeen of the optical dippers are quasi-periodic, compared to four in the infrared; we label them "QPD" in Table 4, and these are synonymous with the periodic AA Tau variables described in Alencar et al. (2010). While these may be explained by a warped disk or orbiting companion, it is more difficult to envision a mechanism for the *aperiodic* dippers. A possible origin is that magnetic turbulence induces scale height changes in the inner disk, as envisioned by Turner (2013).

Also problematic is the total fraction of our data set displaying dipping behavior. With more than 20% of the sample in this category, the assumption that dust obscuration is happening in randomly aligned disks implies that the occulting material lies at scale heights of $\sim$0.2, in units of distance from the central star. The presence of material this high up in a hydrostatic disk might require large surface densities at this radius.

In several cases, dipper behavior does not persist over the entirety of the time series. The fact that we detect fewer dips in the infrared is not simply a selection bias due to the lower cadence of the IRAC time series; a number of objects display prominent dips only in the optical, whereas any corresponding dipping behavior at longer wavelengths is hidden by high-amplitude, long-timescale behavior originating in the disk.

In general, dipper light curves display infrared amplitudes that are less than the optical amplitudes; this supports the idea that the fading events are caused by enhanced dust extinction. We explore the degree of correlation between optical and infrared flux in dipper light curves, as well as implications for the underlying physics, in Section 7.

5.3. Short-duration "Bursting" Light Curves

Dipper light curves are not the only ones displaying asymmetric behavior with respect to flux. We have identified a separate set of variables in the *CoRoT* data set that exhibit abrupt (i.e., 0.1–1 day) increases in flux, followed by decreases in flux on similar timescales. Examples are shown in Figures 13 and 14. We refer to these events as short-duration bursts (hereafter "bursts" or "B" in Table 4). We wish to distinguish them from more powerful outbursts such as FU Ori events, as well as the longer bursts identified in young stars by Findeisen et al. (2013). The bursts in our data set can be differentiated from coronal flares by their symmetric shapes (with respect to time), generally much longer durations, and sequential nature (i.e., many bursts occur in a row; they are by no means isolated events). Our examination of the light curves of WTTSs in the *CoRoT* sample revealed at most a few coronal flares per star over the 40 day observing window. Thus, while some of our bursting events may be due to stellar activity, most require a different explanation.

Some YSOs exhibit isolated bursts above a "continuum" flux level, while others display similar behavior superimposed on a longer term trend. The baseline flux level in bursting light curves of some members of this class even displays quasi-periodic

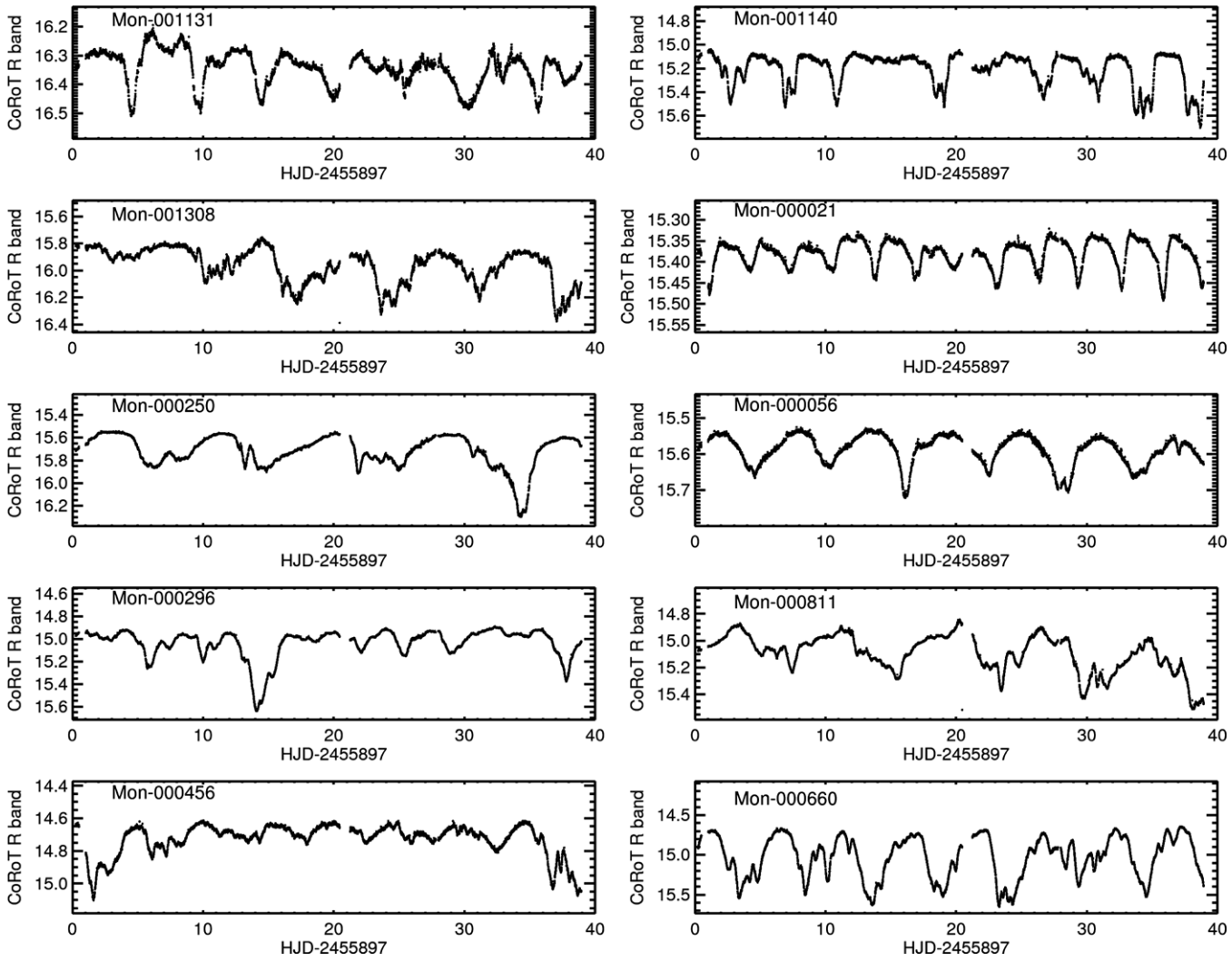

Figure 9. Prototypical quasi-periodic optical dippers observed with *CoRoT*. These light curves preferentially display fading events that repeat regularly, albeit with different amplitudes.

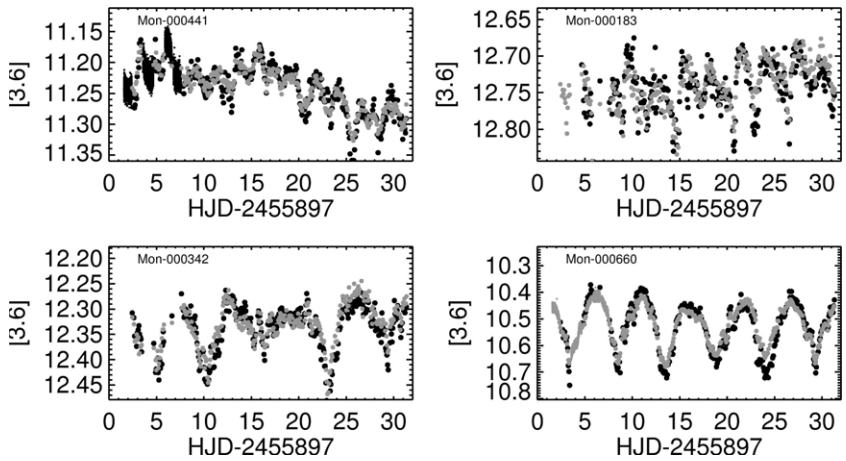

Figure 10. Quasi-periodic infrared dippers among NGC 2264 IRAC sources. Black points are 3.6 μm data, and gray points are 4.5 μm data. Only two of these were also identified as periodic dippers in the optical; the top two objects show small decrements in the *CoRoT* light curves, but the amplitudes were too low to independently confirm dipper status. The lack of larger amplitude behavior in the optical suggests that starspots are not a good explanation for the variability.

variability (i.e., "QPB" in Table 4). Since the burst durations are typically less than 1 day, we have in some cases subtracted out underlying trends to see the bursts more clearly. It should be noted that we are consequently insensitive to bursting behavior in timescales of $\sim$10 days or longer, unless there is no long-term trend.

We detect a total of 20 cases of short-duration optical bursting behavior in our 162 disk-bearing *CoRoT*/*Spitzer* data set, four

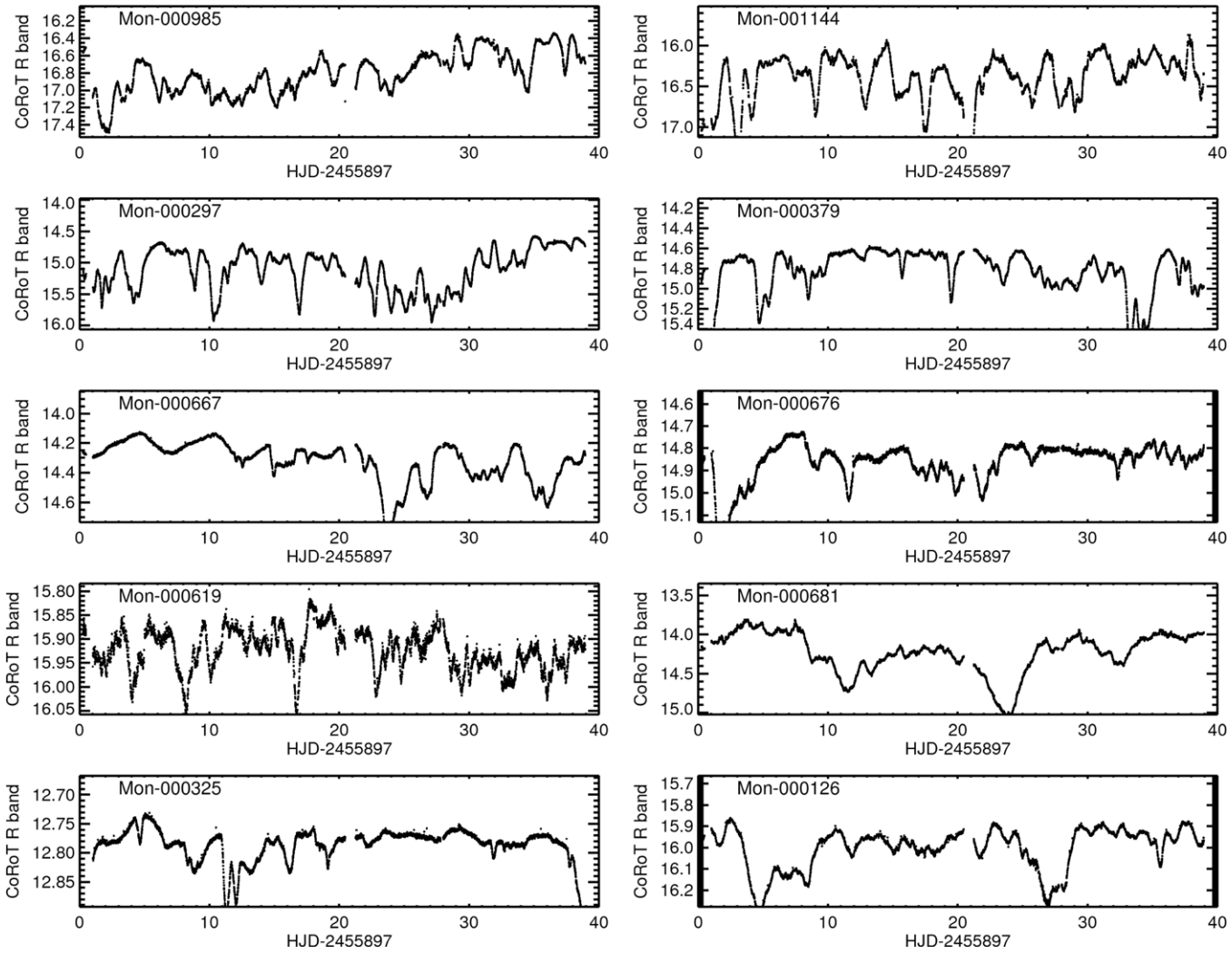

Figure 11. Prototypical aperiodic optical dippers observed with *CoRoT*. These light curves display prominent fading events with no detectable periodicity.

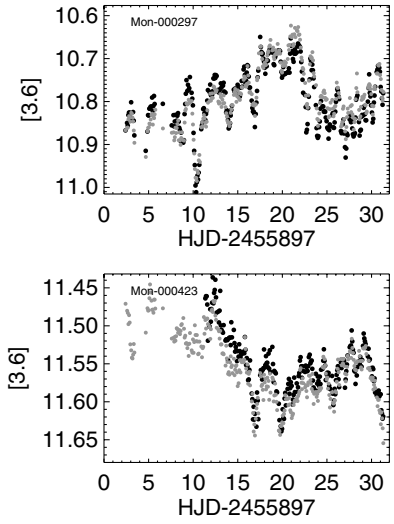

Figure 12. Aperiodic infrared dippers observed with IRAC; only two such objects were identified.

of which also occur in the infrared (see Table 4). In addition, we find three examples (Mon-000119, Mon-000346, Mon-000185) of bursting in the IRAC data set that appear stochastic in the corresponding *CoRoT* light curves (as discussed in Section 5.5), as well as one case where the object does not display prominent variability at all in the optical (Mon-000273).

Bursting behavior in the *Spitzer* data set is much more difficult to identify with the sparser time sampling of ∼12 points per day in the mapping observations. We only identify a few examples *exclusively* in the IRAC time series but note that in about 50% of cases, there are increases in infrared flux coincident with strong bursts in the optical. It therefore appears that a combination of short cadences and high precision (∼1% or better) is crucial to detecting the full range of timescales involved in bursting, at least as it appears in our data set. Longer timescale analogs may be present in multi-year data sets, such as the one presented by Findeisen et al. (2013).

We believe that the bursts are caused by accretion instabilities, based on their resemblance to the predictions of Romanova et al. (2008) and strong ultraviolet (UV) excesses evident for many of these stars. To our knowledge, these are the first observations of an entire class of objects with such behavior. As such, a more detailed exploration of the bursters, including average durations and strengths, is presented in a companion paper (Stauffer et al. 2014).

We wish to note that while this paper and Stauffer et al. (2014) are closely linked, they were written in parallel and evolved somewhat independently. The two papers used slightly different sets of data—most importantly, Stauffer et al. (2014)

Table 4
Variability Properties of the NGC 2264 Members Monitored with *CoRoT* and *Spitzer*

Object	rms (Optical)	rms [3.6]	rms [4.5]	(A)periodic? (Optical)	(A)periodic? (Infrared)	Timescale (d) (Optical)	Timescale (d) (Infrared)	Morph (Optical)	Morph (Infrared)	Stetson (opt/IR)	Lamm Class
CSI Mon-000007-	0.080	0.100	AP	AP	AP	11.70	28.89	B	S	2.94*	-
CSI Mon-000011	0.209	0.139	0.103	AP	AP	15.98	24.67	S	L	2.75	pv?/iv
CSI Mon-000012	0.023	0.023	0.022	QP	AP	2.94	-	QPS	U	0.65*	-
CSI Mon-000021	0.033	0.104	-	QP	AP	3.12	35.78	QPD	L	0.44	-
CSI Mon-000024	0.030	0.017	0.016	-	-	-	-	N	N	−0.00	-
CSI Mon-000056	0.041	0.060	0.049	QP	AP	5.88	35.26	QPD	L	0.02	-
CSI Mon-000058	0.032	0.077	0.085	QP	AP	2.13	15.43	QPS	U	−0.02	-
CSI Mon-000063	0.021	0.027	-	-	AP	-	16.67	N	U	−0.01	-
CSI Mon-000090-	0.022	0.045	0.040	AP	AP	4.09	31.80	U	L	0.02	-
CSI Mon-000103	0.060	0.026	0.020	QP	AP	3.33	13.65	QPS	U	1.33*	-
CSI Mon-000109	0.010	0.026	0.018	-	-	-	-	N	N	0.02	-
CSI Mon-000117-	0.029	0.067	0.066	AP	QP	24.17	4.55	B	QPS	0.86	iv
CSI Mon-000119	0.087	0.067	0.069	AP	AP	9.52	19.63	S	B	2.30	pv?/iv
CSI Mon-000123	0.012	0.022	0.020	-	AP	-	50.74	N	L	0.06	-
CSI Mon-000126	0.096	0.034	0.035	AP	AP	21.62	15.15	D	U	0.37	-
CSI Mon-000131	0.073	-	0.059	AP	AP	16.88	-	U	S	0.97	-
CSI Mon-000134	0.019	0.014	0.011	-	-	-	-	N	N	0.06	-
CSI Mon-000153	0.083	0.085	0.063	QP	AP	1.89	14.36	QPS	S	−0.19	iv
CSI Mon-000164	0.021	0.020	0.028	QP	-	0.66, 0.89	-	MP	N	0.19	-
CSI Mon-000168	0.061	0.053	0.059	AP	AP	49.78	24.83	D	L	0.73	pv?/iv
CSI Mon-000177	0.024	0.043	0.038	QP	AP	3.03	26.91	QPS	L	0.18	-
CSI Mon-000183-	0.017	0.033	0.030	AP	QP	19.50	3.01	U	QPD	0.18	iv+
CSI Mon-000185-	0.010	0.057	0.056	AP	AP	13.90	49.56	S	B	0.50	iv
CSI Mon-000219	0.097	0.029	0.031	-	AP	-	33.78	N	U	0.24	-
CSI Mon-000242	0.053	0.065	0.070	AP	AP	23.10	33.20	D	L	1.16	pv?/iv
CSI Mon-000250	0.143	0.087	0.080	QP	AP	9.09	17.28	QPD	L	−0.37	-
CSI Mon-000256	0.058	0.061	0.051	P	P	3.85	3.79	EB	EB	2.41	iv
CSI Mon-000273	0.012	0.048	0.059	-	AP	-	18.11	N	B	0.20	pv?/iv
CSI Mon-000279	0.025	0.022	0.017	QP	P	7.69	8.33	QPS	P	0.17	-
CSI Mon-000280	0.040	0.026	0.023	-	AP	-	13.54	N	U	0.02	-
CSI Mon-000290	0.016	0.031	0.037	QP	QP	5.88	5.88	QPS	QPS	0.31	-
CSI Mon-000296	0.130	0.030	0.025	QP	AP	7.69	30.28	QPD	U	0.24	iv+
CSI Mon-000297	0.326	0.069	0.070	AP	AP	8.72	17.73	D	D	5.60	iv+
CSI Mon-000305	0.020	0.020	0.052	-	AP	-	14.79	N	U	0.04	-
CSI Mon-000314	0.033	0.076	0.080	QP	AP	3.23	11.95	QPD	L	0.83	iv
CSI Mon-000325	0.035	0.080	0.025	AP	AP	9.56	40.64	D	L	−1.03*	-
CSI Mon-000326-	0.022	0.028	0.025	AP	QP	8.12	8.71	U	QPS	0.12	-
CSI Mon-000328	0.030	0.021	0.015	-	AP	-	10.00	N	U	0.00	-
CSI Mon-000335	0.022	0.065	0.065	QP	AP	4.55	16.06	P	U	0.07	iv
CSI Mon-000341	0.035	0.045	0.046	AP	AP	19.90	25.08	B	U	0.75	iv
CSI Mon-000342-	0.029	0.047	0.041	AP	AP	6.39	-	D	D	0.77	iv
CSI Mon-000346	0.110	0.062	0.060	AP	AP	22.80	-	S	B	0.78	-
CSI Mon-000356	0.030	0.016	0.012	-	-	-	-	N	N	−0.00	-
CSI Mon-000357	0.016	0.070	0.074	-	AP	-	21.92	N	L	0.40	-
CSI Mon-000358	0.039	0.037	0.038	QP	AP	5.88	12.00	QPD	U	0.37	-
CSI Mon-000370	0.041	0.027	0.026	QP	AP	12.50	-	QPS	L	0.24	-
CSI Mon-000378	0.070	0.056	0.044	QP	AP	11.11	24.32	QPS	L	0.39	pv?/iv
CSI Mon-000379	0.203	0.055	0.058	AP	AP	24.44	37.55	D	L	1.34	-
CSI Mon-000406	0.028	0.024	0.023	QP	AP	6.67	9.96	QPB	U	0.43	-
CSI Mon-000412	0.057	0.068	0.066	QP	AP	6.58	46.43	QPB	B	0.49	iv
CSI Mon-000423-	0.041	0.039	0.042	AP	AP	27.06	52.32	D	D	0.31	iv+
CSI Mon-000424	0.034	0.033	0.031	-	AP	-	35.80	N	L	0.16	iv
CSI Mon-000425	0.119	0.027	0.022	AP	AP	69.40	18.46	S	U	1.31*	iv+
CSI Mon-000427	0.025	0.020	0.013	QP	P	14.29	14.28	QPS	P	0.11	-
CSI Mon-000433	0.089	0.145	0.173	QP	AP	10.00	38.41	QPD	U	0.97	iv
CSI Mon-000434	0.042	0.019	0.025	P	AP	0.73, 7.48	33.45	MP	U	0.35	-
CSI Mon-000441	0.031	0.039	0.034	QP	QP	2.56	2.47	QPD	QPD	0.60	-
CSI Mon-000448-	0.038	0.027	0.031	AP	AP	22.10	18.87	U	U	0.04	-
CSI Mon-000454	0.024	0.019	0.016	-	-	-	-	N	N	−0.01	iv
CSI Mon-000456	0.096	0.048	0.028	QP	QP	5.00	4.65	QPD	QPS	0.95	iv
CSI Mon-000457	0.078	0.059	0.052	AP	AP	14.23	56.72	S	L	0.97*	pv?/iv
CSI Mon-000462-	0.004	0.088	0.083	AP	AP	49.79	19.98	D	L	0.23*	-
CSI Mon-000469	0.125	0.121	0.130	AP	AP	18.70	30.52	S	S	2.91	pv?/iv
CSI Mon-000470	0.015	0.017	0.017	-	QP	-	8.333	N	QPS	0.04	-
CSI Mon-000474	0.034	0.041	0.037	AP	AP	18.92	18.92	B	U	0.57*	iv

Table 4
(Continued)

Object	rms (Optical)	rms [3.6]	rms [4.5]	(A)periodic? (Optical)	(A)periodic? (Infrared)	Timescale (d) (Optical)	Timescale (d) (Infrared)	Morph (Optical)	Morph (Infrared)	Stetson (opt/IR)	Lamm Class
CSI Mon-000491	0.187	0.048	0.039	AP	AP	32.12	35.77	L	L	0.41*	iv++
CSI Mon-000498	0.042	0.039	0.033	QP	AP	4.35	19.00	QPD	U	−0.57*	-
CSI Mon-000510	0.047	0.036	0.051	AP	AP	33.59	24.82	B	U	0.32	pv?/iv
CSI Mon-000525	0.006	0.021	0.013	QP	-	2.00	-	QPD	N	−0.27*	iv
CSI Mon-000530	0.018	-	0.015	-	-	-	-	N	N	−0.01	-
CSI Mon-000558	0.026	0.055	0.045	QP	AP	11.11	38.95	QPS	L	1.20*	-
CSI Mon-000566-	0.020	0.051	0.050	AP	AP	21.46	7.99	U	D	0.23	-
CSI Mon-000567	0.101	0.101	0.096	AP	AP	18.38	14.00	B	B	3.13*	iv
CSI Mon-000577	0.033	0.050	0.048	AP	AP	6.24	18.03	S	U	0.72	iv
CSI Mon-000586-	0.035	0.030	0.032	AP	AP	27.91	28.70	U	L	−0.02	-
CSI Mon-000590-	0.016	0.014	0.009	AP	QP	47.25	2.27	S	QPS	0.12	-
CSI Mon-000598	0.042	0.087	0.075	AP	AP	57.61	43.289	B	L	0.37	-
CSI Mon-000613	0.063	0.031	0.030	AP	AP	26.94	51.44	S	L	0.92	-
CSI Mon-000617	0.012	0.017	0.008	QP	QP	5.88	5.88	QPS	QPS	0.10	-
CSI Mon-000619	0.043	0.114	0.106	AP	AP	6.10	47.86	D	L	−0.14	iv
CSI Mon-000631	0.004		0.015	-	AP	-	-	N	U	−0.22*	iv
CSI Mon-000636	0.171	0.069	0.065	AP	AP	19.12	33.79	S	L	1.63	-
CSI Mon-000637-	0.049	0.030	-	AP	AP	40.37	9.10	L	U	0.14	-
CSI Mon-000638	0.005	0.008	0.008	-	-	-	-	N	N	0.11*	-
CSI Mon-000650	0.117	0.029	0.028	AP	AP	36.88	23.36	D	L	0.53*	iv
CSI Mon-000654-	0.032	0.050	0.047	AP	AP	14.80	21.47	U	L	−0.11	iv+
CSI Mon-000660	0.265	0.090	0.070	QP	QP	5.00	5.26	QPD	QPD	6.96	-
CSI Mon-000667	0.139	0.129	0.115	AP	AP	38.48	50.62	D	L	0.60	-
CSI Mon-000676	0.092	0.079	0.087	AP	AP	12.17	28.89	D	L	0.81	iv
CSI Mon-000681	0.262	0.051	0.039	AP	AP	39.90	15.34	D	U	4.22*	pv?/iv++
CSI Mon-000697-	0.025	0.016	0.014	AP	-	18.29	-	U	N	0.04	pv?/iv
CSI Mon-000717	0.102	0.066	0.056	QP	QP	9.09	8.33	QPD	QPS	1.17	-
CSI Mon-000723-	0.019	0.016	0.016	AP	AP	16.89	-	U	U	0.04	-
CSI Mon-000733	0.008	0.014	0.009	-	-	-	-	N	N	−0.02	-
CSI Mon-000753	0.015	0.014	0.013	-	QP	-	1.59	N	QPS	0.05	-
CSI Mon-000765	0.025	0.134	0.156	QP	AP	2.38	41.38	QPS	L	0.08	-
CSI Mon-000766	0.065	0.106	0.111	AP	AP	19.75	45.87	S	L	1.06	pv?/iv
CSI Mon-000771	0.053	0.028	0.032	AP	AP	22.45	40.87	U	L	0.26	iv
CSI Mon-000774	0.145	0.068	0.046	AP	AP	9.21	51.96	S	L	3.07	-
CSI Mon-000804-	0.010	0.139	0.094	-	AP	15.17	45.91	B	L	0.06	-
CSI Mon-000808	0.035	0.046	0.044	AP	AP	37.26	10.36	B	U	0.54	iv++
CSI Mon-000811	0.139	0.051	0.052	QP	QP	7.69	8.33	QPD	QPS	1.53	iv++
CSI Mon-000876-	0.020	0.120	0.168	AP	AP	9.32	9.69	U	U	0.02	-
CSI Mon-000877	0.051	0.040	0.036	QP	AP	5.26	30.52	QPB	U	0.61	pv?/iv
CSI Mon-000879	0.034	0.025	0.012	AP	AP	34.70	6.29	S	U	0.20	-
CSI Mon-000914-	0.025	0.019	0.015	AP	AP	50.17	35.24	U	L	−0.03	-
CSI Mon-000919-	0.019	0.024	0.023	AP	AP	32.72	14.76	B	U	0.18	-
CSI Mon-000928	0.012	0.044	0.059	-	AP	-	11.47	N	L	0.16	-
CSI Mon-000936	0.052	0.043	0.049	AP	AP	21.55	-	B	B	1.15	-
CSI Mon-000937	0.015	0.035	0.027	-	AP	-	20.91	N	U	0.16	iv
CSI Mon-000945	0.095	0.069	0.063	AP	AP	41.91	31.78	B	L	0.80	-
CSI Mon-000946	0.028	0.024	-	-	-	-	-	N	N	0.05	-
CSI Mon-000949	0.028	0.014	0.018	-	-	-	-	N	N	−0.01	-
CSI Mon-000951-	0.026	0.042	0.049	AP	AP	9.56	37.66	U	L	0.02	-
CSI Mon-000954	0.032	0.026	0.029	P	AP	7.14	1.05	P	U	0.24	iv
CSI Mon-000985	0.236	0.058	-	AP	QP	68.64	4.35	D	QPS	1.99	-
CSI Mon-000996	0.098	0.051	0.044	AP	QP	62.20	8.33	S	QPS	1.07	iv
CSI Mon-001003-	0.028	0.025	-	AP	AP	36.84	40.26	U	U	−0.02	-
CSI Mon-001005	0.014	0.022	0.031	QP	AP	1.77	-	QPS	U	0.04	-
CSI Mon-001017-	0.018	0.033	0.038	AP	AP	-	54.88	B	L	0.08	-
CSI Mon-001022	0.070	0.061	0.061	AP	AP	14.96	38.49	B	L	1.32*	pv?/iv
CSI Mon-001031	0.015	0.026	0.028	QP	QP	4.55	4.55	QPS	QPS	−0.42	-
CSI Mon-001037	0.259	0.041	0.039	AP	AP	6.44	28.33	QPS	U	2.22*	-
CSI Mon-001038-	0.038	0.129	0.147	AP	AP	23.35	44.51	D	L	0.18	iv
CSI Mon-001048-	0.030	0.017	0.013	AP	AP	22.12	11.80	B	U	0.07	-
CSI Mon-001053	0.054	0.030	0.026	AP	AP	25.40	13.08	S	S	0.67	-
CSI Mon-001054	0.056	0.045	0.056	AP	AP	3.65	49.04	S	L	0.53	-
CSI Mon-001059	0.024	0.024	0.023	QP	AP	5.88	30.39	QPS	L	0.01	-
CSI Mon-001061	0.108	0.087	0.080	AP	AP	15.81	55.28	S	L	1.99	-
CSI Mon-001064	0.017	0.013	0.014	P	AP	2.70	23.28	P	U	0.22	-

Table 4
(Continued)

Object	rms (Optical)	rms [3.6]	rms [4.5]	(A)periodic? (Optical)	(A)periodic? (Infrared)	Timescale (d) (Optical)	Timescale (d) (Infrared)	Morph (Optical)	Morph (Infrared)	Stetson (opt/IR)	Lamm Class
CSI Mon-001076	0.067	0.034	0.034	AP	QP	65.26	5.88	U	QPS	−0.06	iv
CSI Mon-001085	0.040	0.020	0.018	P	P	3.45	3.45	P	P	1.16	-
CSI Mon-001094	0.043	0.037	0.043	QP	QP	4.17	4.45	QPS	QPS	1.97	-
CSI Mon-001099	0.014	0.036	0.038	QP	AP	3.45	27.05	QPS	U	0.32*	-
CSI Mon-001100-	0.030	0.049	0.041	AP	AP	8.53	33.21	U	L	−0.22*	pv?/iv
CSI Mon-001112	0.029	0.015	0.011	-	-	-	-	N	N	0.04	-
CSI Mon-001114	0.042	0.053	0.080	QP	AP	2.56	17.96	QPS	L	1.15	-
CSI Mon-001131	0.058	0.065	0.067	QP	AP	5.26	20.63	QPD	S	0.18	-
CSI Mon-001132	0.196	0.086	0.080	QP	AP	2.94	15.94	QPS	S	−0.43	iv
CSI Mon-001140	0.137	0.047	0.054	QP	QP	3.85	3.70	QPD	QPS	1.32	-
CSI Mon-001142	0.012	0.019	0.022	-	AP	-	9.58	N	U	−0.03	-
CSI Mon-001144	0.249	0.108	0.088	AP	AP	6.07	20.38	D	S	2.92	iv
CSI Mon-001149	0.025	0.017	0.019	-	AP	-	24.05	N	U	0.01	iv
CSI Mon-001157	0.012	0.026	0.033	QP	AP	3.85	26.58	QPS	U	0.09	-
CSI Mon-001167	0.059	0.030	0.028	QP	AP	9.09	9.21	QPS	S	0.42	iv
CSI Mon-001171	0.051	0.055	0.057	AP	AP	31.87	26.08	D	S	0.40	-
CSI Mon-001174-	0.037	0.035	0.034	AP	AP	76.09	12.86	B	B	0.76	-
CSI Mon-001181	0.023	0.016	0.015	QP	P	5.88	1.69, 5.88	QPS	MP	0.06	-
CSI Mon-001187-	0.044	0.047	0.045	AP	QP	60.81	3.12	B	QPS	0.93	iv
CSI Mon-001197	0.019	0.027	0.033	QP	AP	4.00	24.82	QPS	U	0.02	-
CSI Mon-001199	0.228	0.067	0.044	QP	QP	3.57	3.70	QPS	QPS	6.41	iv
CSI Mon-001205	0.031	0.016	0.012	P	P	6.67	6.67	P	P	0.38	iv
CSI Mon-001217	0.061	0.061	0.054	QP	AP	7.69	30.42	QPB	U	2.20*	-
CSI Mon-001219	0.031	0.018	0.015	-	-	-	-	N	N	−0.02	-
CSI Mon-001221	0.019	0.055	0.050	-	AP	-	47.96	N	L	0.03	-
CSI Mon-001223	0.054	0.021	0.017	QP	QP	8.33	7.54	QPS	QPS	0.54	-
CSI Mon-001234	0.129	0.050	0.043	AP	QP	6.80	4.76	S	QPS	1.55	pv?/iv
CSI Mon-001240	0.030	0.023	0.020	-	QP	-	2.08	N	QPS	0.14	-
CSI Mon-001249-	0.014	0.018	0.010	AP	AP	10.84	12.49	U	U	0.06	-
CSI Mon-001294	0.063	-	0.050	AP	QP	33.14	7.14	S	QPS	0.86	-
CSI Mon-001308	0.133	0.099	0.096	QP	QP	6.67	6.90	QPD	QPS	2.65	iv++
CSI Mon-006491	0.104	0.087	0.088	AP	AP	7.62	32.44	S	L	1.64	-

Notes. Variability status of stars in this paper. Mon ID numbers marked with a - sign denote faint ($R > 15.5$) variables that were detected only by eye. Columns 5 and 6 list whether the stars is aperiodic ("AP") by the Stetson index or rms measure, periodic ("P"), quasi-periodic ("QP"), or not detected as variable ("-"). Columns 7 and 8 are timescales, the derivation of which depends on whether the object is (quasi-)periodic or aperiodic. If (quasi-)periodic, then we list the timescale derived from the autocorrelation and periodogram analysis (Section 6.2); if aperiodic, then we list the timescale derived from the PeakFind algorithm (Section 6.5). In Columns 9 and 10, we provide the optical and infrared morphologies, with the following codes: S, stochastic; U, unclassifiable variable type; QPS, quasi-periodic symmetric; QPD, quasi-periodic dipper; QPB, quasi-periodic burster; L, long-timescale variable; N, non-variable; B, burster; D, dipper; EB, eclipsing binary; P, periodic; MP, multi-periodic. In Column 11, we note the degree of optical/infrared correlation via the median running Stetson index; here we have averaged the values from 3.6 μm and 4.5 μm data (both against optical light curves). The last column indicates the variability type ("pv" for periodic, and "iv" for irregular) assigned by Lamm et al. (2004) and compiled in their Table 4. *Stetson indices marked with asterisks are larger, because those objects only had HDR mode observations and hence fewer data points.

included stars with only 2008 *CoRoT* light curves, whereas such stars were excluded here—and slightly different criteria for defining light-curve classes. This resulted in slightly different sets of stars belonging to each class. In particular, the burst-dominated class in Table 1 of Stauffer et al. (2014) included 23 stars; 19 of those are also listed as burst dominated in Table 4 of this paper. Of the remaining four, one (Mon-000185) was included in Stauffer et al. (2014) based on its 2008 *CoRoT* light curve and hence was not in the parent sample for this paper. The other three were all classified as stochastic in our Table 4. Inclusion or exclusion of these stars from the burst-dominated class would not appreciably change the conclusions in either paper.

5.4. Quasi-periodic Symmetric Behavior

Our formal period search (Section 6.2) uncovered many quasi-periodic light curves in both the *CoRoT* and *Spitzer* data sets. Only five optical and four infrared light curves in our infrared-excess restricted data set displayed strictly periodic behavior typical of the spotted WTTSs in the current and previous *CoRoT* run on NGC 2264 (Affer et al. 2013). This set includes only two stars that are periodic in both bands (Mon-001085 and Mon-001205; see Table 4). This is not entirely surprising considering that our stars were selected specifically to have disks based on their SEDS, and many are actively accreting based on spectroscopy.

The remaining quasi-periodic disk-bearing stars exhibit repeating patterns that either change in shape from cycle to cycle or include lower amplitude stochastic behavior superimposed on a periodicity. We refer to these as quasi-periodic symmetric, or "QPS," in Table 4. Excluding the quasi-periodic dipper class, as well as the handful of quasi-periodic bursters already accounted for above, we detect 27 quasi-periodic symmetric cases in the optical and 22 in the infrared, with 6 appearing in both bands. Examples are shown in Figures 15 and 16. Unlike the

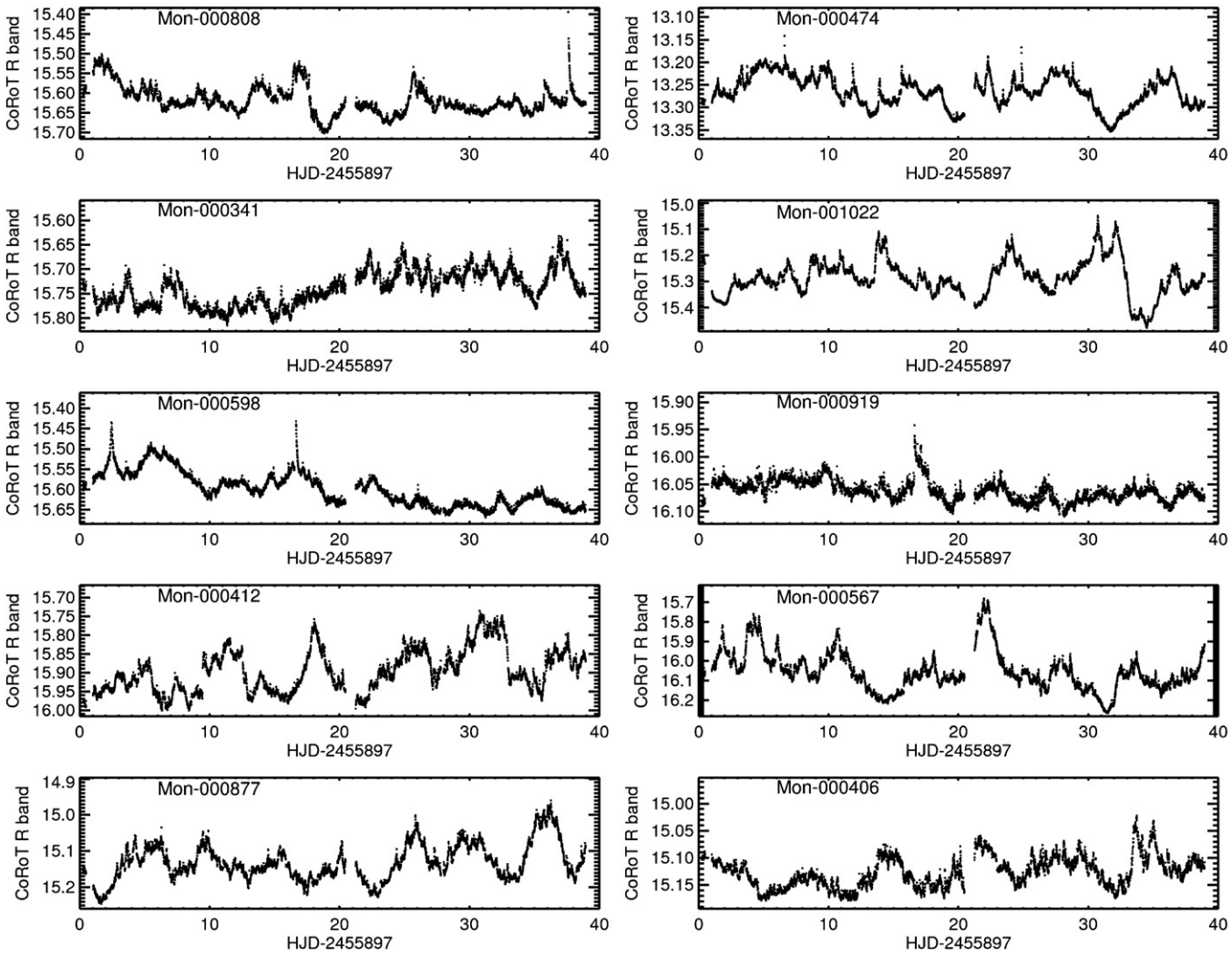

Figure 13. Prototypical bursters: short-duration flux increases in the optical. The events seen here may represent accretion bursts; some repeat regularly, while others are aperiodic.

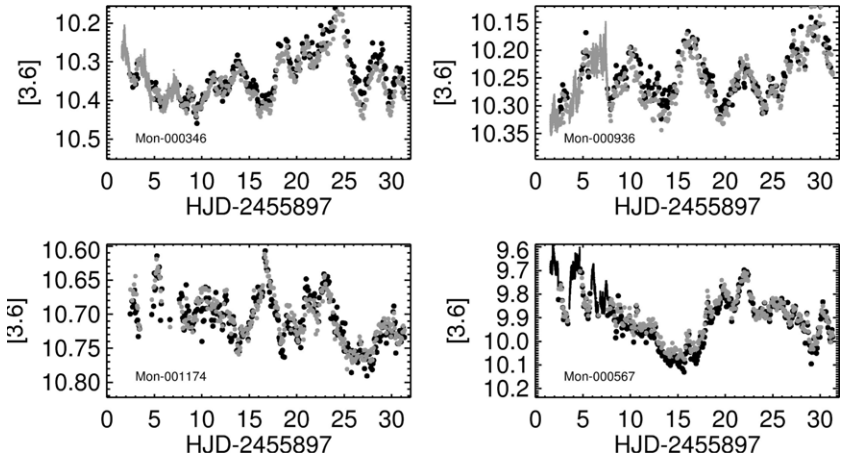

Figure 14. Infrared variables detected with bursting events in the IRAC staring and mapping time series. Black points are 3.6 μm data, and gray points are 4.5 μm data. Densely sampled portions at the beginning of the Mon-000346, Mon-000936, and Mon-000567 light curves are staring data.

bursters and dippers, all of these light curves are relatively symmetric with respect to an upside-down flip. We consider here only variables with periods less than half the total observation baseline; longer timescale behavior is indistinguishable from the "stochastic" class, introduced below.

The infrared variables that show repeating patterns do tend to be partially correlated with the optical behavior, even in cases for which we have assigned different morphology classes for the two wavelength bands. This may reflect multiple origins for the infrared flux variations: if a light curve is a superposition

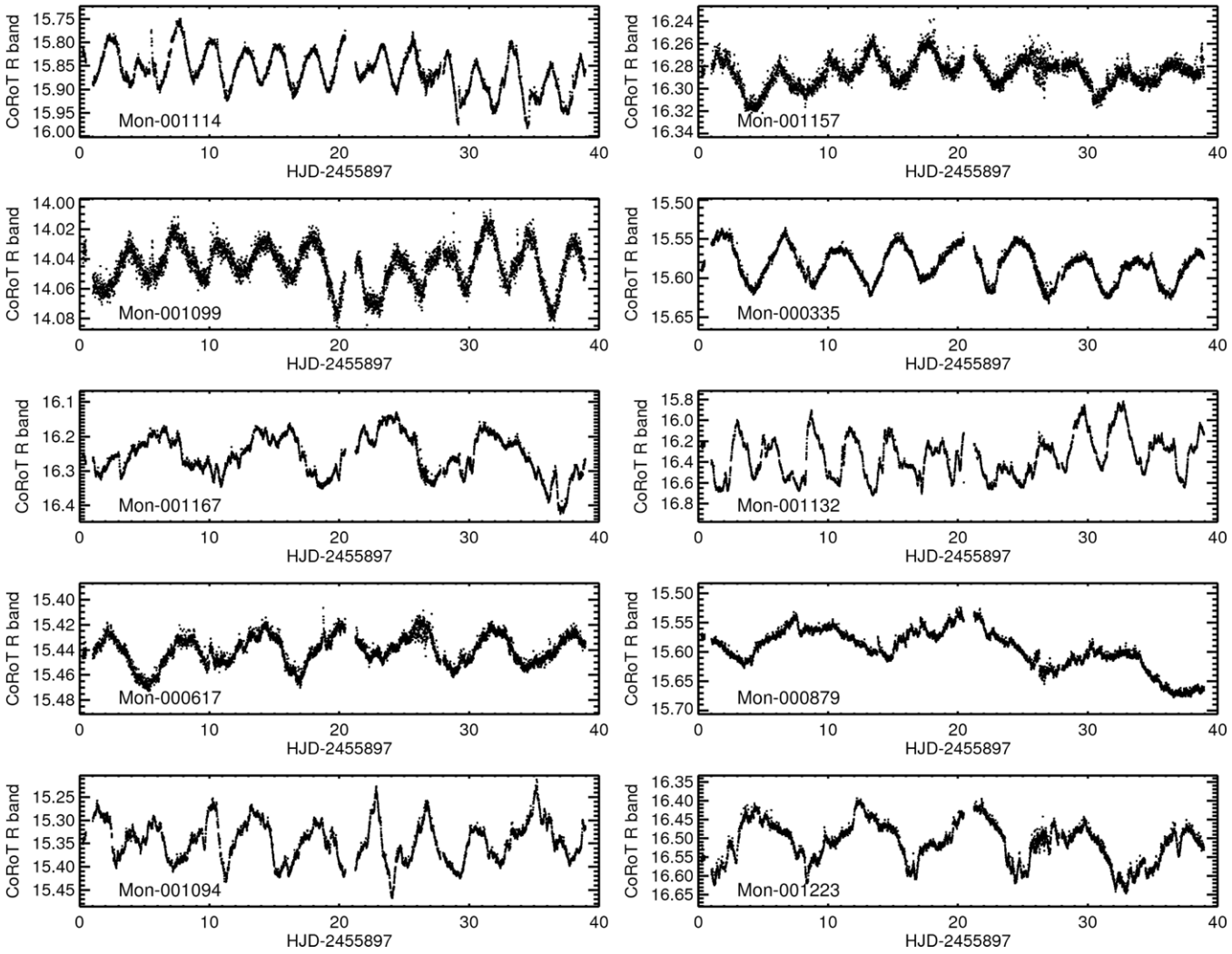

Figure 15. Quasi-periodic optical variability in NGC 2264 *CoRoT* sources. The patterns in these light curves show regular repetition, but amplitudes and shapes change from one cycle to the next.

of periodic behavior and higher amplitude aperiodic changes, then we may detect the former but assign a different overall classification.

We propose two possible origins for this quasi-periodic symmetric variability. First, it may be a combination of purely periodic variation (such as cool starspot modulation) with longer timescale aperiodic changes (e.g., from accretion). Second, it could reflect a single variability process that is not entirely stable from cycle to cycle. Examples include stellar hot spots for which brightness evolves as a function of stochastic accretion flow (e.g., the type IIp variability highlighted by Herbst et al. 1994), or structural inhomogeneities in the surrounding disk periodically occulting the central star, but with geometries different from the standard dipper orientation. The latter is indicated in cases where a $v\sin i$ value suggests that the measured period is too long to originate at the stellar photosphere (e.g., Artemenko et al. 2012; Cody et al. 2013). In addition, we cannot rule out that we are seeing cool spots that evolve much faster on disk-bearing stars than on their weak-lined counterparts.

5.5. "Stochastic" Stars

The majority of remaining variables show no preference for fading or brightening but nevertheless exhibit prominent brightness changes on a variety of timescales. Fourier transform periodograms (see Cody & Hillenbrand 2010) for these objects display amplitudes devoid of dominant periodicities and consistent with a "$1/f$" trend in amplitude; two examples are provided in Figure 17. This is in contrast to typical red or "flicker" noise, which follows a $1/\sqrt{f}$ trend in amplitude and $1/f$ in power (Press 1978). Thus, our stochastic objects display more power at low frequency than expected for standard flickering. Similar behavior was detected in a Herbig Ae star by Rucinski et al. (2010). The combination of lack of periodicity and coherence of the light curves suggests that these objects may represent a superposition of variable extinction (as in the dipper stars) and stochastic accretion (as in the bursting stars).

Stochastic behavior constitutes one of the largest classes of variability in the *CoRoT* data set. Figure 18 illustrates prototypical examples of optically stochastic behavior. We focus specifically on short-timescale stochastic YSOs, which have peak-to-peak timescales much less than the 40 day duration of the light curve. There are in fact only two longer duration variables among the optical sample (see Section 6.5); thus, there is a true dearth of optical behavior on timescales longer than a week.

Most *infrared* light curves are aperiodic, with fewer examples of quasi-periodic or asymmetric flux behavior (as in dippers

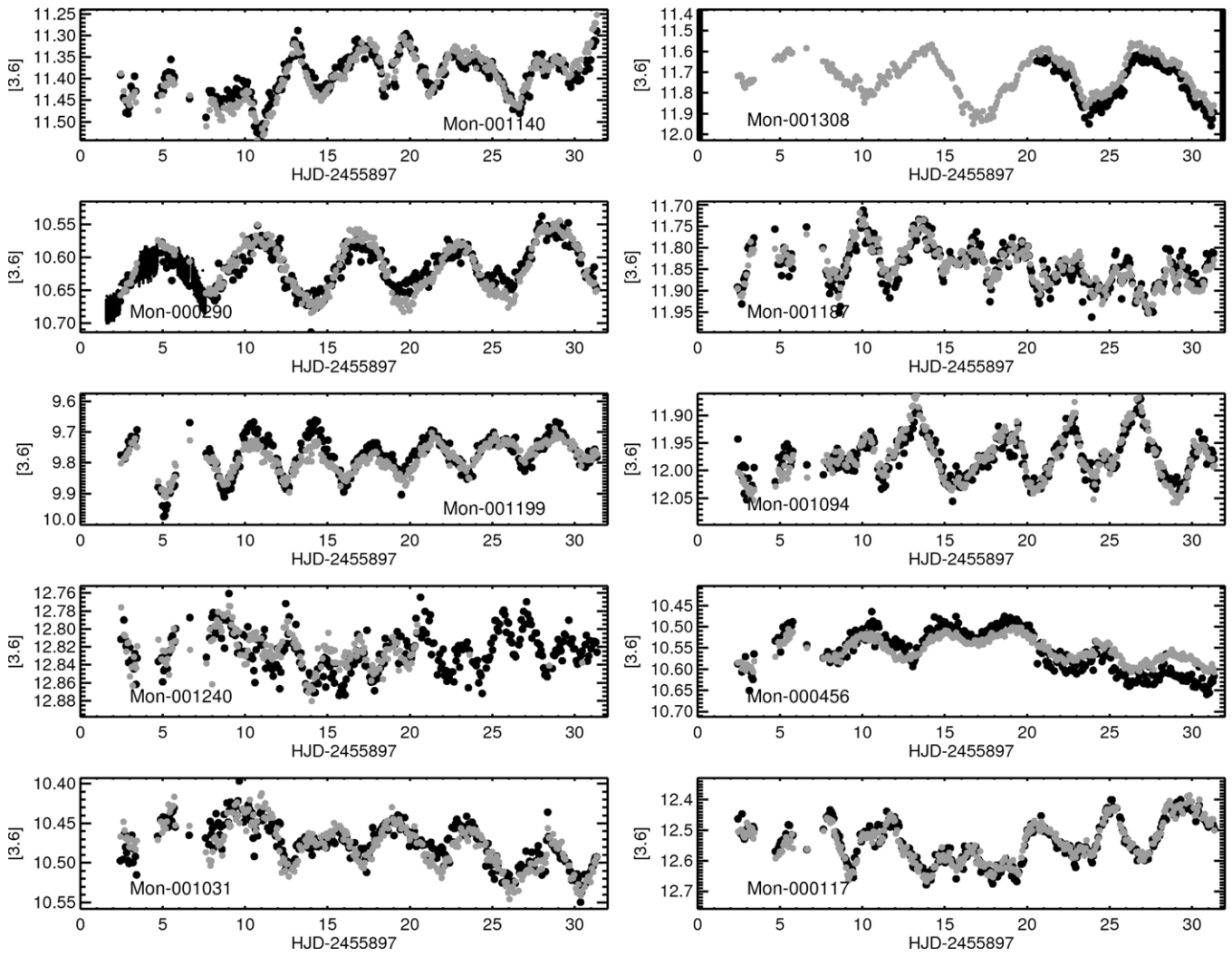

Figure 16. Quasi-periodic infrared variability in NGC 2264 IRAC sources. Black points are 3.6 μm data, and gray points are 4.5 μm data.

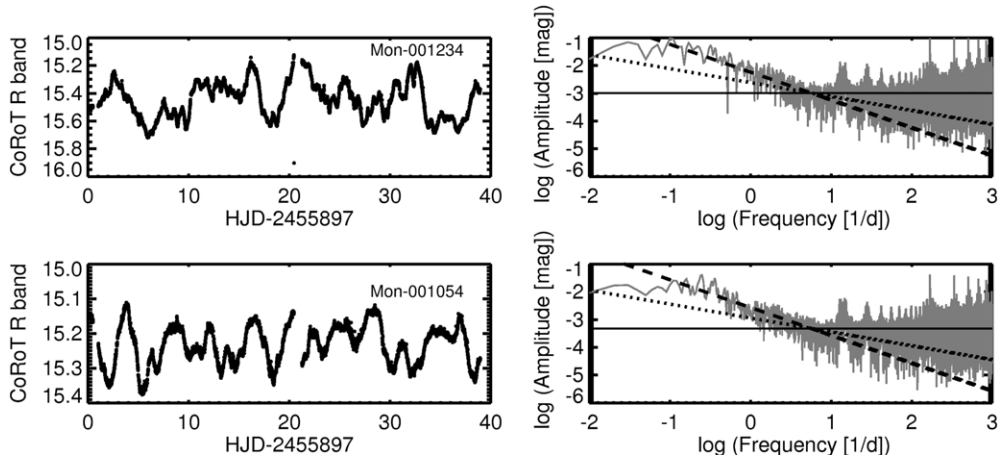

Figure 17. Light curves for two prototypical stochastically behaving stars, along with their Fourier transform periodograms, shown here in log space. Each Fourier transform consists of three parts: a relatively flat low-frequency regime, a steeper red noise trend from $\log(f) \sim -1$ to 1, and a flat white-noise-dominated regime for log frequencies beyond 1.0. We have fitted the white noise with a single value, shown as a black line. The red noise is modeled by a $1/\sqrt{(f)}$ trend in amplitude (i.e., $1/f$ in power; dashed line) and a $1/f$ trend in amplitude (dotted line), the latter of which fits the data much better.

or bursters) than in the optical. The timescales evident in the mapping data are also somewhat longer. Since the flux is generally disk dominated (although not by a large factor) at 3.6 and 4.5 μm, stochastic infrared variability could have a different origin from that in the optical, although it may simply reflect reprocessed variable starlight. The latter possibility is supported by the fact that we find stochastic behavior to be more than twice as common in the optical band than in the infrared. For long-timescale trends (see Section 5.6), the reverse is true: the behavior is much more common in the infrared. Orbital

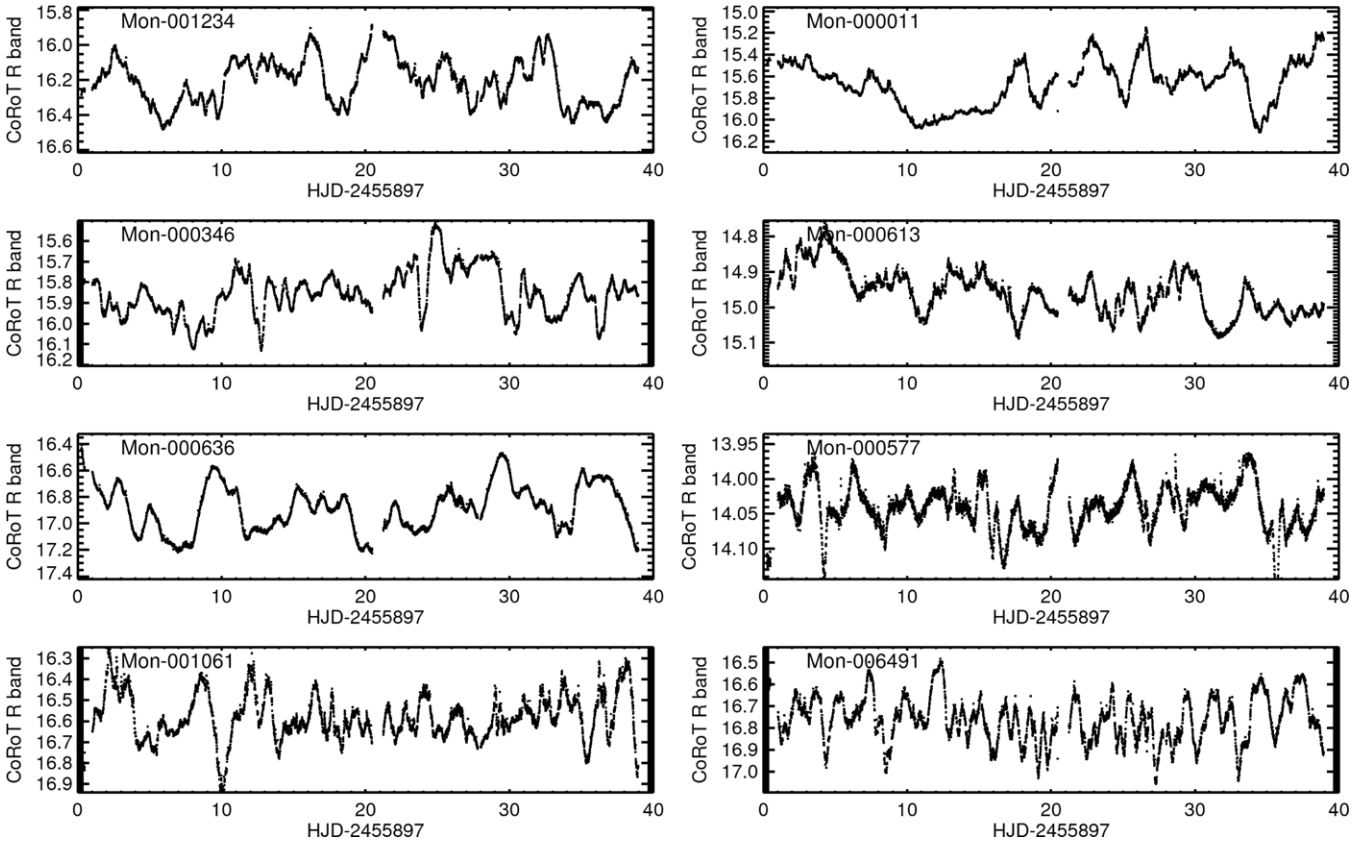

Figure 18. Stochastic optical light curves in the *CoRoT* sample. These variables show no detectable periodicity, nor any preference for fading or brightening events.

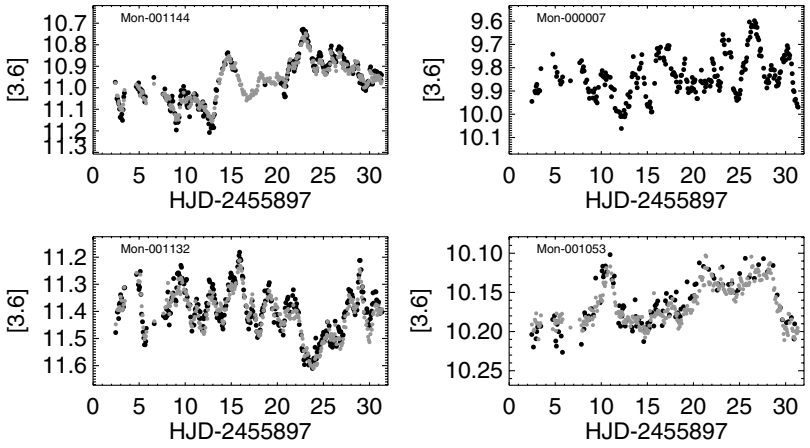

Figure 19. Stochastic infrared light curves detected in IRAC time series. Black points are 3.6 μm data, and gray points are 4.5 μm data.

timescales in the disk emission region range from a couple of days to several weeks, depending on the mass and temperature of the star. It is therefore difficult to produce stochastic infrared behavior without invoking reprocessed optical variability or long timescales, which we consider separately below.

We present a selection of stochastic infrared light curves in Figure 19.

5.6. Long-timescale Behavior

A subset of our disk-bearing stars displays variability that grows or declines all the way out to the longest timescale of observation. We select as "long timescale" those objects for which the largest peak-to-peak amplitudes occur on timescales of 15 days or longer. This behavior is much more common among the infrared light curves than those in the optical. Because of the 30–40 day duration of our time series, we are unable to classify the trends morphologically and simply refer to them as "long-timescale" variables. The long duration of flux changes likely reflects disk dynamics beyond the inner edge, where Keplerian timescales are longer than one week. It also involves fairly large amplitude changes, from 0.08 to 0.6 mag among the sample identified here. We present prototypical examples of long-timescale infrared behavior in Figure 20.

Notably, the optical behavior of these objects involves much shorter timescales. Only two *CoRoT* light curves contained trends gradual enough to be classified as "long timescale." The rest fall into a variety of classes, from quasi-periodic dippers to stochastic.

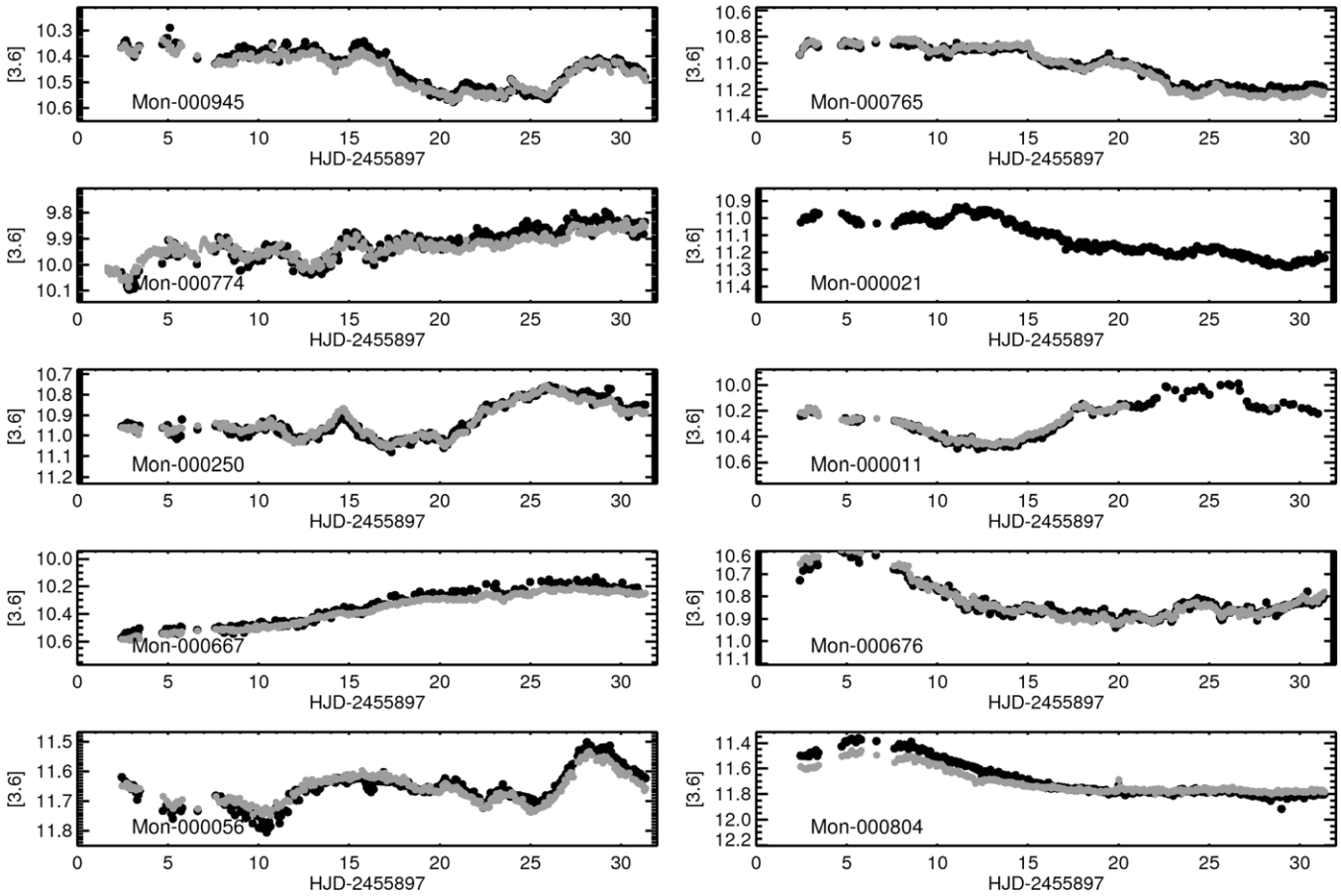

Figure 20. Infrared light curves with long-timescale variability. Black points are 3.6 μm data, and gray points are 4.5 μm data. The peak-to-peak amplitude range for these objects is 0.18–0.42 mag.

The distribution of stochastic and long-timescale stars in each band suggests that while some infrared variability reflects reprocessed starlight, this is a minor contribution to the flux. Some other process must dominate the long-wavelength variability at long timescales, and this could involve changes in the disk luminosity or shape.

5.7. Unusual Variability Types in Disk-bearing YSOs

There are several notable cases of rare light-curve types that merit discussion, since they may signify unusual geometry, disk evolutionary states, or variability processes.

We detect purely periodic optical behavior in only five stars (Mon-000335, Mon-001064, Mon-001085, Mon-001205, and Mon-000954), which we show in Figure 21. The latter two are nearly sinusoidal. These light curves are not easily distinguishable from the magnetically active WTTSs, and in fact all but two of them have weak or transitional disk SED classifications ("II/III"), along with weak reported Hα emission equivalent widths and low UV excesses. By some schemes, these sources could have been included with the WTTS set. We therefore believe that the variability here reflects cold spots on the stellar surface in systems where circumstellar dust obscuration and variable accretion are minimal. Nevertheless, it could be generated by very stable accretion flow onto a hot spot in the two objects that have significant infrared excesses (Mon-000335 and Mon-001064).

Similar to the optical light curves, we detect only four instances of periodic infrared behavior, shown in Figure 22: Mon-000279, Mon-000427, Mon-001205, and Mon-001085. The latter two of these are also periodic in the optical, likely reflecting the variability induced by rotational modulation of starspots.

We also highlight an unusual optical light curve consisting of a periodic morphology interrupted by fading episodes, as shown in Figure 23. The origin of the variability in this K5.5 star, Mon-000378, may be a combination of spots interspersed by circumstellar extinction dip events; this is difficult to verify since the infrared behavior does not correlate with the optical in this case.

5.8. Statistical Division of Light-curve Morphologies

The fractions of different variability types offer insights into the diversity and relative importance of different physical mechanisms at work in the inner disks, magnetospheres, and stellar photospheres of young stars. We reproduce the schematic of the different variability types in Figure 24, with their fractions overlaid.

The fractions for different types of optical variability are also presented in Table 5. A subset of light curves did not fall into any of the morphological classes described above, either because the data were noisy or because the light-curve shape was unusual. We denote these as unclassifiable in Tables 3 and 5.

The non-variable stars are those sources that did not pass the Stetson test (infrared) or rms test (optical and single-band infrared). Among the *CoRoT* light curves, we are only able to distinguish variability down to rms values of 0.02 at $R = 14$ and 0.06 at $R = 16$. It is likely that the 19% of optical sources

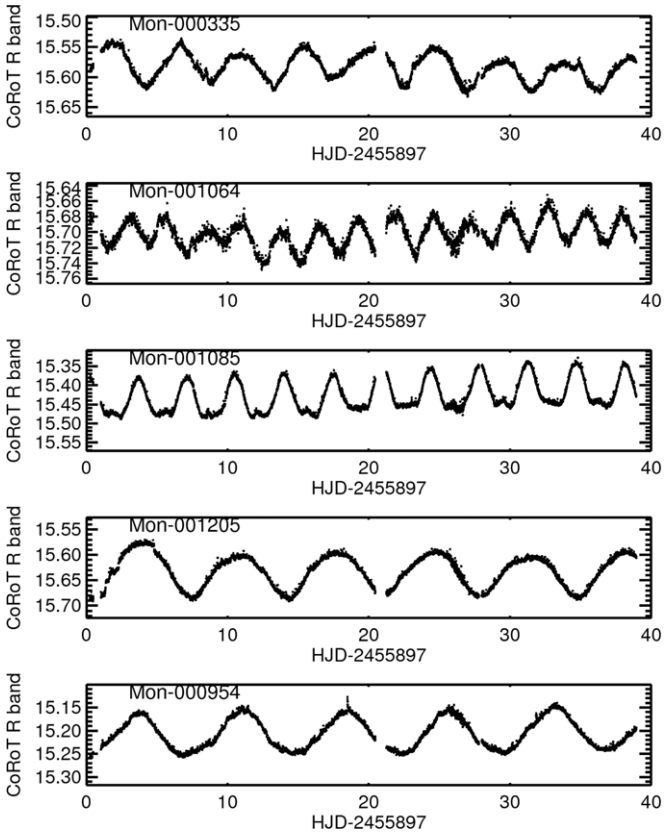

Figure 21. Periodic (as opposed to quasi-periodic) optical light curves. These are the most regular light curves in the entire disk-bearing data set. The weak infrared excesses, Hα, and low UV excesses of these objects suggest that they host cool magnetic spots, which appear in the light curves via rotational modulation.

Table 5
CSI 2264 Morphology Fractions in Disk-bearing Stars

Morphology Class	Optical	Infrared
Bursters	13^{+3}_{-2}% (21)	5^{+2}_{-1}% (8)
Periodic dippers	10.5^{+3}_{-2}% (17)	3^{+2}_{-1}% (5)
Aperiodic dippers	11^{+3}_{-2}% (18)	1^{+2}_{-1}% (2)
Quasi-periodic symmetric	17±3% (27)	13.5^{+3}_{-2}% (22)
Stochastic	13^{+3}_{-2}% (21)	6^{+2}_{-1}% (9)
Long timescale	1^{+2}_{-1}%	30^{+4}_{-3}% (48)
Periodic	3^{+2}_{-1}% (5)	2.5^{+2}_{-1}% (4)
Multiperiodic	1^{+2}_{-1}% (2)	1±1% (1)
Eclipsing binary	1±1% (1)	1±1% (1)
Unclassifiable	11^{+3}_{-2}% (18)	29^{+4}_{-3}% (47)
Non-variable	19±3% (30)	9^{+3}_{-2}% (15)

Notes. We list the fractions of objects in each variability class, along with the number (out of the 162 member disk-bearing object set) in parentheses. These classifications have been made by eye, whereas we provide statistical support for them in Section 6.4.

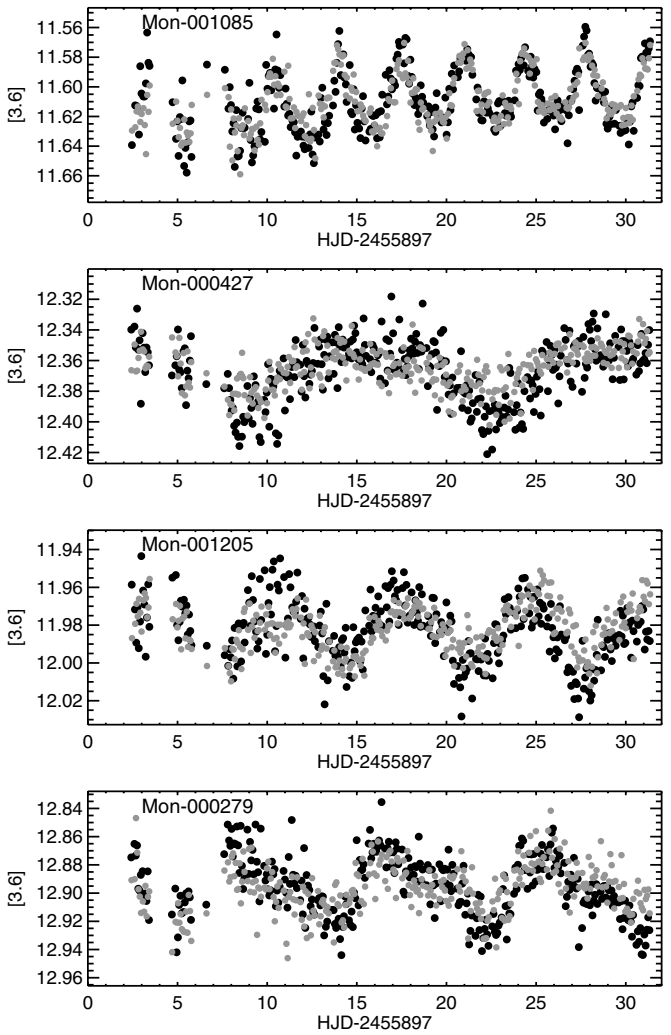

Figure 22. Periodic infrared light curves. Black points are IRAC 3.6 μm data, and gray points are 4.5 μm.

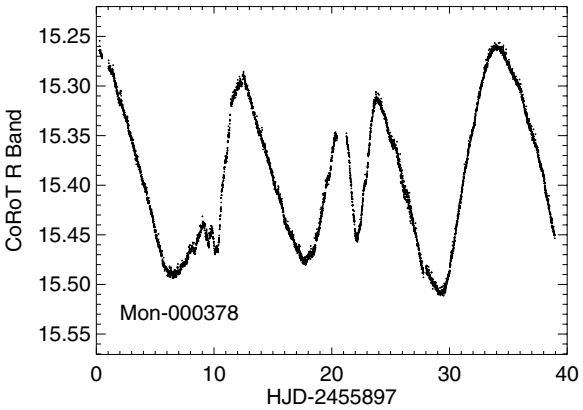

Figure 23. The unusual optical light curve of Mon-000378. This may be a combination of periodic behavior and circumstellar obscuration.

that are not variable according to our statistical measures simply have lower level brightness fluctuations.

Of note, the total fraction of dippers (both periodic and aperiodic) is just over 21%, a value that significantly exceeds the prediction of Bertout (2000) (15%), but is not as large as the ∼30% found by Alencar et al. (2010). These results suggest that the frequency of dipper behavior is surprisingly large, given typical inner disk scale height estimates (e.g., $H/R \sim 0.05$).

Assessment of our infrared data set revealed that long-timescale variability was the most common type, and the other variability groups were less populated. The associated fractions for each infrared morphology class are also included in Table 5. Evidently, infrared variability is more common than optical variability, at least at the wavelengths and timescales sampled by these observations of disk-bearing sources.

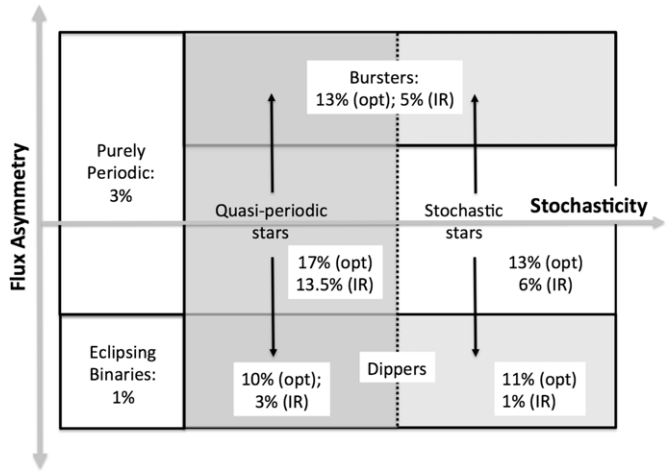

Figure 24. Schematic of the optical and infrared variability types detected in our 162 member disk-bearing data set, with optical ("opt") and infrared ("IR") fractions. Not noted here are the percentages of long-timescale and unclassifiable variables, as well as non-variables; hence, the listed values do not add up to 100%.

5.9. Assessment of Sample Bias

In order to compare our identified variability types with models, we must first account for any biases introduced by the *CoRoT* sample selection. Targets for this telescope were selected in advance, whereas we observed all stars in a ∼1 square degree region with *Spitzer*/IRAC. *CoRoT* targets were selected primarily with NGC 2264 membership in mind, and priority was given to known CTTSs. Since we have already restricted our light-curve morphology sample using membership and infrared excess, there should be no associated bias. There was, however, knowledge of variability from *CoRoT*'s SRa01 observations in 2008, and one might ask whether this contributed to more variables being observed than in a randomly selected sample of CTTSs. We argue that the answer is no, for the following reasons.

First, we have examined the input target priority list for the 2011 *CoRoT* observations. It is this set from which the final target list and pixel masks were selected. Of 772 possible high-priority targets, 350 were not previously observed by *CoRoT* and hence should have no variability bias. Of the 474 targets that were already observed in 2008, *none* had variability as the sole signature of youth. All input stars had prior membership information consistent with our criteria described in the Appendix and therefore should not be biased by previous knowledge of variability.

To probe further for systematics in our variability class fractions, we have selected a set of disk-bearing NGC 2264 members that were observed with *CoRoT* in 2008 and *Spitzer* in 2011. In this way, we assemble a sample similar to the 2011 data set highlighted in the rest of this paper, but with no prior knowledge of variability (apart from some sparser ground-based data, such as that of Lamm et al. (2004)). We classified the optical morphologies into the same categories described in this section and computed their fractions. We find that the fraction of non-variables is actually *higher* in 2011 than 2008 (19% versus 11%), again refuting the idea that variability knowledge biased the input catalog, thereby affecting the results reported here. On the contrary, we attribute the higher fraction of non-variables in 2011 to a slightly fainter sample. The total number of disk-bearing stars approximately doubled from the 2008 to the 2011 *CoRoT* run, and many of the newly observed sources were fainter and thus had lower signal-to-noise ratio than the typical SRa01 target.

Comparing the distribution of variable types in 2008 versus 2011, we find that in every one of the categories presented in Sections 5.1–5.6, *except* for the aperiodic dippers, the fraction of stars in each class for 2008 is the same to within the uncertainties presented above in Section 5.8. The fraction of aperiodic dippers decreased from ∼20% in the 2008 data set to 11% in the 2011 data set. This change is offset by the increase in the fraction of non-variable sources in 2011, leaving all of the other class fractions the same to within the 1σ errors. We speculate that the slightly fainter (and hence lower mass) 2011 sample may bias against the detection of aperiodic dipper behavior. However, it is not clear as to why the *periodic* dipper fraction is then similar in both samples. Because of this discrepancy in the aperiodic dipper fraction, we suggest that its uncertainty be increased from ∼3% to ∼10% in any theoretical attempt to account for the distribution of variability types.

6. STATISTICAL IDENTIFICATION AND PROPERTIES OF VARIABILITY

By eye, both the optical and infrared Light-curve sets display a wide variety of behaviors, including varied morphologies and timescales. Yet classification and understanding of the variability properties of our disk-bearing stars benefits from a quantitative approach. At some level, we are likely to identify all accreting stars as variable, given sufficient precision. We wish to determine the fraction of our light curves that are variable at the ∼1% level, thereby defining a subsample of objects to which we can attach a confident morphological classification. We therefore measure a suite of light-curve statistics for further classification, including amplitudes, standard deviations, symmetry metrics, and timescales.

6.1. Statistical Selection of Variables

6.1.1. IRAC Data Set

The high precision and cadence, as well as large sample size, of our *Spitzer* and *CoRoT* data sets permit detection of stellar variability down to fairly low amplitudes in comparison to previous photometric monitoring studies. Since our focus here is on disk-bearing stars, we might expect the majority of targets to display non-sinusoidal or aperiodic variability dominated by accretion and circumstellar effects rather than the cool spot rotational modulation that explains well the periodic variability of the WTTSs, as pointed out by Herbst et al. (1994). We have therefore taken several approaches to identifying photometrically variable objects in the photometry.

For IRAC data, we take advantage of the fact that nearly simultaneous light curves are available at both 3.6 and 4.5 μm for the majority of objects (151/162 stars in the disk-bearing *CoRoT*/IRAC sample). Furthermore, the behavior in these two bands should be similar, since their emission regions in the disk are at comparable radii. This enables identification of correlated variability via a Stetson cross-correlation index (Stetson 1996), the use of which was previously promoted for variability detection in young stars by Carpenter et al. (2001) and Plavchan et al. (2008b). For data in two bands, this index is defined in the following way:

$$\text{Stetson} = \Sigma_{i=1}^{N} \text{sgn}(P_i)\sqrt{|P_i|}, \quad (3)$$

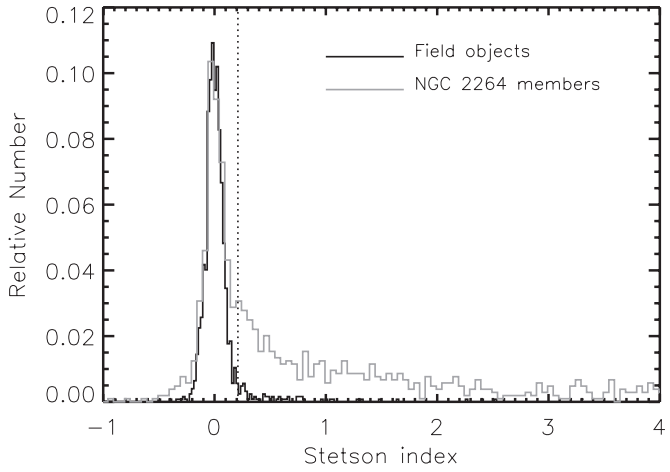

Figure 25. Distribution of Stetson indices for objects with mapping light curves in both IRAC channels. Light curves of known cluster members are clearly more correlated than those of field stars. Our adopted 3σ cutoff for variability, as determined from the field object distribution, is shown as a dotted line.

where N is the number of simultaneous pairs of observations in the two bands, sgn is the sign function (i.e., -1 for negative input values, 0 at zero, and 1 for positive input values), and P_i is the product of the normalized residuals of two observations:

$$P_i = \frac{N}{N-1}\left(\frac{d_{1i} - \langle d_1 \rangle}{\sigma_{1i}}\right)\left(\frac{d_{2i} - \langle d_2 \rangle}{\sigma_{2i}}\right), \quad (4)$$

where d_{1i} and d_{2i} are simultaneous photometric points in bands 1 and 2, respectively, $\langle d \rangle$ refers to their means, and σ_{1i}, σ_{2i} their uncertainties, including systematics.

Since data taken at each wavelength are not exactly simultaneous, we interpolate one of the light curves onto the time stamps of the other. We find that the Stetson index has a roughly constant baseline regardless of stellar brightness. Objects with Stetson values well above this level have a degree of correlation in the two bands that cannot be accounted for by random noise. We determine a threshold for variability by examining the Stetson index distribution of likely field stars that do not meet any of the NGC 2264 membership criteria outlined in the Appendix, as displayed in Figure 25. These have a low probability of being variable and should therefore reflect the intrinsic noise spread in Stetson index. We fit a Gaussian profile to the distribution, finding a 1σ width of 0.07. We therefore adopt a variability threshold of 0.21, for 3σ confidence; this is denoted by the dotted line in Figure 25. The distribution of Stetson indices for likely cluster members (also shown in Figure 25) displays a break at this value, confirming that this cutoff is a reasonable dividing line between variable and non-variable objects.

To select infrared variables among the set of targets with only single-band IRAC mapping or staring data, we must rely on another variability criterion. Light-curve rms is a suitable metric, as long as we take the systematic noise contribution into account. We incorporate the noise model determined in Section 2.2 to compare the measured rms values against the expected noise level in each mapping light curve. For staring light curves, we use the estimated uncertainties, since these are a good approximation to the errors. Each of the four staring time series is treated separately.

We determine a cutoff value in the difference between measured and expected log(rms). As with the assessment of systematic errors, we have divided our sample into sets of field stars and confident NGC 2264 members. Stars that are

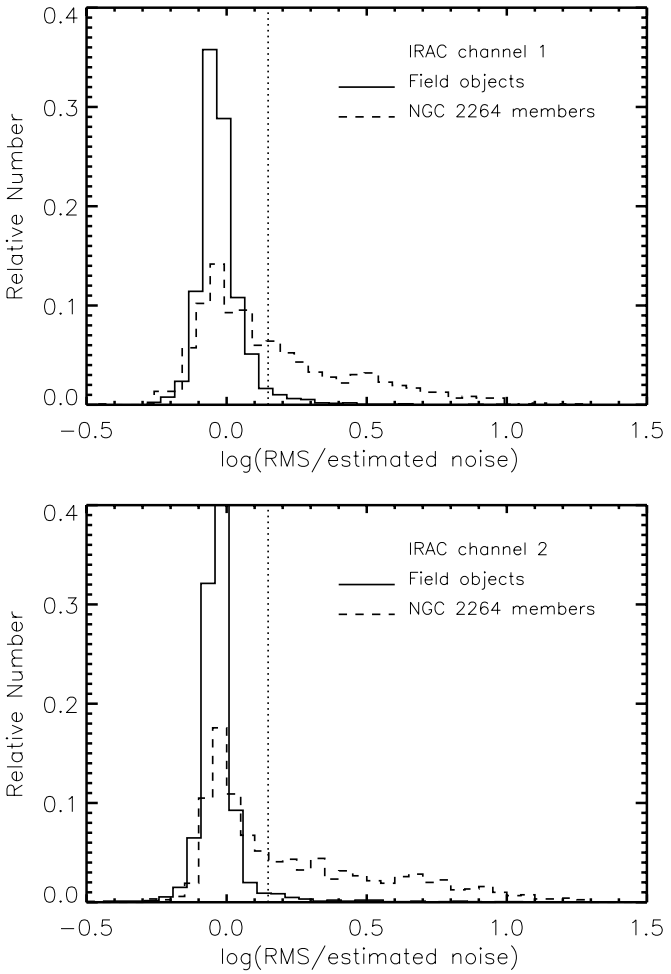

Figure 26. Histograms of rms values from IRAC mapping light curves in channel 1 (top) and channel 2 (bottom). The dotted vertical line indicates the 3σ variability cutoff determined from the rms distribution of field objects.

candidates but not confident members are not included in the determination of the cutoff, but they are evaluated for variability afterward. We take the distribution of rms values for the group of field stars to be representative of non-variable behavior, and find it to be approximately Gaussian. The excess of rms beyond expectations is much larger for the second group, as shown in Figure 26. We adopt as our single-band variability criterion a cutoff of 3σ, or 0.15, in the distribution of $\log(\mathrm{rms}/\mathrm{rms}_{\mathrm{expected}})$. This is indicated by dotted vertical lines in Figure 26. For stars with data in both IRAC bands, we find that the rms test is not as sensitive as the Stetson index in detecting variability.

Out of the 162 member disk-bearing data set considered here, 11 do not have multi-band *Spitzer* data, and nine (82%) of these are variable by the rms criterion. In the subset that *do* have data in both bands, 137 of 151 (91%) are variable by the Stetson index. In contrast, only 36% of stars *without* disks detected by *Spitzer* are variable in the infrared, and many of these display sinusoidal patterns attributable to rotating starspots.

Objects with amplitudes larger than 0.2 mag were inspected on the raw IRAC images to determine whether stray light from a bright neighboring star might be inducing artificial variability via background contamination. This is often the case when an object with both 3.6 and 4.5 μm data is detected as variable based on its rms, but not based on the Stetson index. A handful of candidate variables were eliminated in this way.

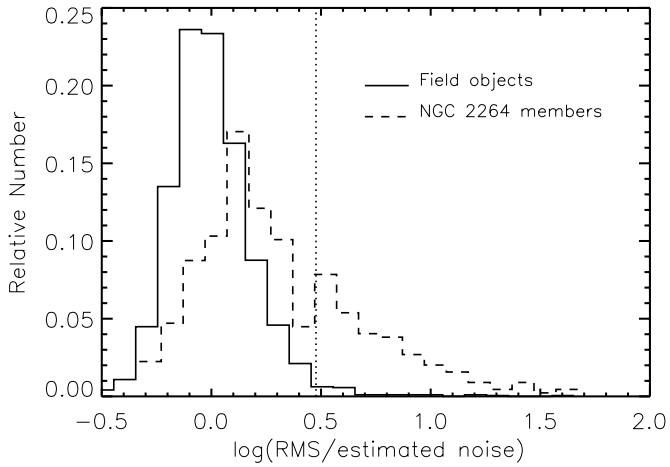

Figure 27. Distribution of *CoRoT* light curve rms values divided by estimated uncertainty. Cluster members are clearly more variable than field stars, although the distribution is determined in part by pre-selection of targets, some of which were observed to be variable during the 2008 *CoRoT* run. The vertical dotted line marks the 3σ cutoff that we have determined from the non-member rms distribution; this was used for variable selection.

6.1.2. CoRoT Data Set

Selection of variables in the *CoRoT* data set is more difficult than with *Spitzer*/IRAC given the systematic effects (e.g., jumps, hot pixels) present in some of the light curves. Defects remained even after correction of the two most prominent jumps in the light curves (see Section 3.2).

For variable selection, we first considered the full set of YSOs observed by *CoRoT* and then narrowed our focus to the 162 disk-bearing stars with simultaneous *Spitzer* data. We determined the median trend in rms as a function of magnitude, using 0.5 mag bins and omitting objects that were flagged or known NGC 2264 members (implying high likelihood of variability). Despite the unexplained structure at $R > 14$ (see Figure 6), the median fit in log space is well modeled by the Poisson noise expectation, shifted upward by a constant value of 0.35. We therefore adopted this as the underlying noise distribution. The fit breaks down for $R < 12$, and here we simply adopt the median trend in rms, which is roughly linear.

We require that variables have rms values at least three times the median noise level for their magnitude. In Figure 27, we display the distributions of log(rms/noise) for likely cluster members and field stars. The cluster members are clearly more variable, and the chosen cutoff at rms/noise = 3.0 selects variables at the $\sim 3\sigma$ confidence level, according to a fit of the non-member distribution. Additional low-amplitude periodic objects that did not meet this rms selection criterion were identified via periodogram and autocorrelation function (ACF) analysis, which we discuss below.

We find the chosen threshold to be adequate in that all of the selected objects are clearly variable by eye. However, there is a collection of faint ($R > 16$) objects in the *CoRoT* sample that are also clearly variable by eye, but do not meet the selection criterion since their rms values are <0.05 mag. The brightness fluctuations in these cases consist of short-duration upward or downward events that depart significantly from the median value but are too transient to contribute significantly to the overall variance. The coherence of the light curves during the events causes them to stand out in comparison to the artificial fluctuations caused by *CoRoT* systematics. In a number of cases, this variability is supported by strong correlation with infrared behavior in the corresponding IRAC light curve. We identified a handful of additional such variables by eye, as indicated in Table 4.

Disregarding flagged light curves, we find 218 definitively variable stars in the entire *CoRoT* data set, circled in Figure 6. Although the WTTSs are not the subject of this paper, we find that ∼45% of them are variable by the rms criterion alone (this fraction would increase were periodicity detection to be employed as well). Considering hereafter only the ones in the 162-object disk-bearing sample with both IRAC and *CoRoT* data, we are left with 83 variable by the rms criteria. A further 30 faint stars mainly with $R > 16$ were added to this set based on variability identified by eye. We identified 19 additional variables based on periodicity or quasi-periodicity alone, as explained below. The variability status of all objects in the disk-bearing data set is indicated in Table 4.

6.2. Identification of Periodic and Quasi-periodic Variables

Periodic photometric behavior is common among YSOs, although it is mostly associated with spotted WTTSs. Our disk-dominated sample does include a number of stars with quasi-periodic light curves, few of which are sinusoidal. We have developed a criterion below to differentiate between "periodic" and "quasi-periodic" stars. By "quasi–periodic," we refer to light curves that have a stable period but whose shape and/or amplitude changes from one cycle to the next. We use "periodic," on the other hand, to denote stable repeating patterns with shapes that evolve minimally over the 40 days of observation.

To select these objects from the IRAC and *CoRoT* data sets and identify legitimate variables that did not meet the rms or Stetson criteria, we have developed a period search technique. McQuillan et al. (2013) showed that the ACF is a particularly good tool for selecting the correct period from a non-sinusoidal light curve, by considering the larger of the first two local ACF peaks. The commonly used periodogram, on the other hand, tends to display many peaks corresponding to harmonics and aliases that may be confused with the true signal. We have therefore carried out a preliminary period search by interpolating all light-curve magnitude values onto evenly spaced time grids with interval $\Delta\tau$ and N points, and computing the ACF based on the following equation:

$$\mathrm{ACF}(\tau) = \frac{\sum_{i=0}^{N-\tau/(\Delta\tau)-1}(d_i - \langle d\rangle)(d_{i+\tau/(\Delta\tau)} - \langle d\rangle)}{\sum_{i=0}^{N-1}(d_i - \langle d\rangle)^2}. \quad (5)$$

Here d_i are the light-curve data points, $\langle d\rangle$ is their mean, $\tau = n\Delta\tau$ is the time lag, and N is the total number of points in the interpolated light curve. We let the time lag run from zero to the maximum baseline of the time series; peaks in the ACF indicate lag values for which the light curve is self-correlated. While interpolation may alter the light curves slightly, the sampling is dense enough compared to variability timescales that we expect any resulting inconsistencies to be small. We typically oversample the light curve by a factor of 1.5, corresponding to $\Delta\tau \sim 6$ minutes for *CoRoT* data and $\Delta\tau \sim 1.5$ hr for IRAC data. For each ACF, we note all local maxima occurring at time lags greater than zero and less than half the total time baseline (i.e., ∼15 days for IRAC light curves and ∼20 days for *CoRoT* light curves). We required the amplitude of any such peaks to be greater than 0.05 over the surrounding local minima. We then select the first or second local maximum, depending on which is higher. An example of this process and the succeeding steps are illustrated for Mon-000660 in Figure 28.

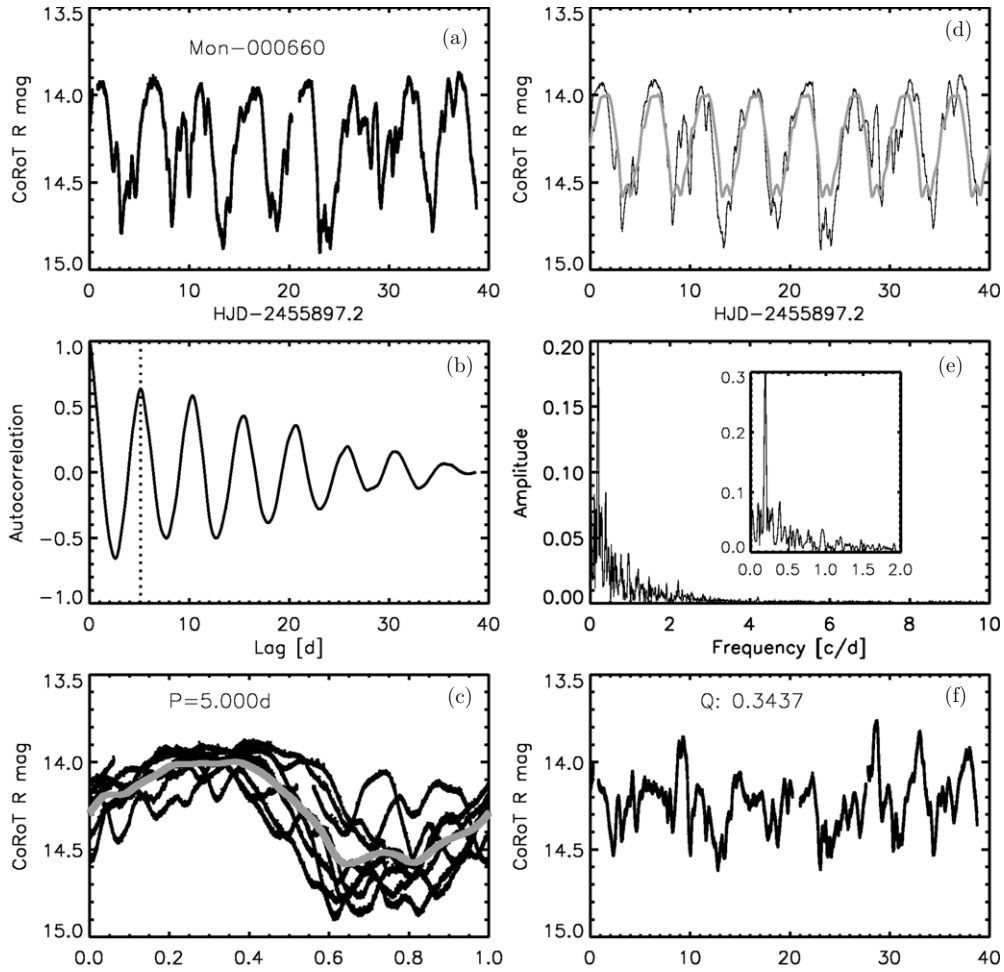

Figure 28. Example of the process we have used to identify periodic and quasi-periodic variables. In panel (a) we show the raw light curve for Mon-000660, and in panel (b) its ACF with the highest peak marked. Zooming in on the corresponding frequency in the periodogram in panel (e), we refine the frequency by noting the maximum here. We then phase the light curve to the corresponding period in panel (c), producing the boxcar-smoothed trend seen in gray. We overplot that trend on the raw light curve in panel (d) and subtract it from the raw light curve in panel (f). This remaining flux is then used to compute the Q value and determine that substantial residuals make this light curve quasi-periodic.

To check whether the selected ACF peak corresponds to a significant periodicity in the light curve, we then compute a Fourier transform periodogram and search for peaks within 15% of the frequency expected from the period of the ACF peak. Upon identifying the periodogram peak, we phase-fold the light curve around the selected period. Based on the coherence of phased light curves, we find that periods extracted from the periodogram are more accurate than those adopted from the ACF; the latter is more sensitive to long-term trends in the light curve. Initial use of the ACF is nevertheless vital to determining which of multiple peaks is the correct period to phase around, as shown by McQuillan et al. (2013).

Once the light curve is folded, we generate a smoothed phase-folded light curve smoothing over a boxcar with width 25% of the period. This approach is similar to that of Plavchan et al. (2008b), except that we only phase the light curve to a single period, as opposed to a continuum of periods. We overlay the smoothed phase curve on the original light curve, repeating it once per period. Comparison of the phase trend curve with the raw light curve provides an impression of how well a periodic model explains the behavior. We subtract the two curves to produce a residual as a function of time. For strictly periodic light curves, the remaining points should consist of noise, and indeed the residuals are consistent with the uncertainties shown in Figures 2 and 6. However, most of our light curves are better described as quasi-periodic: the amplitude of the residuals is significantly reduced compared to the raw data, but there remain strong trends not attributable to systematic errors. This is particularly the case for objects that display repeating flux dips of varying amplitude.

We have adopted a metric to assess the degree of periodicity in the light curves, by comparing the rms value before and after subtraction of the smooth phased curve. Since we are only considering timescales up to half the data length, we first remove any long-term trends on timescales over 15 days (IRAC) or 20 days (*CoRoT*) by subtracting a boxcar-smoothed version with a window of 10 days. We compute a periodicity metric, "Q," by assessing how close the light-curve points are to the systematic noise floor before and after the phased trend is subtracted from the light curve:

$$Q = \frac{\left(\mathrm{rms}^2_{\mathrm{resid}} - \sigma^2\right)}{\left(\mathrm{rms}^2_{\mathrm{raw}} - \sigma^2\right)}, \quad (6)$$

where $\mathrm{rms}_{\mathrm{raw}}$ and $\mathrm{rms}_{\mathrm{resid}}$ are the rms values of the raw light curve and the phase-subtracted light curve, respectively, whereas σ is the estimated uncertainty including the systematics (e.g., Section 3.3). Testing on sinusoidal light curves typical of WTTSs, we find Q to be a few percent or even negative (i.e.,

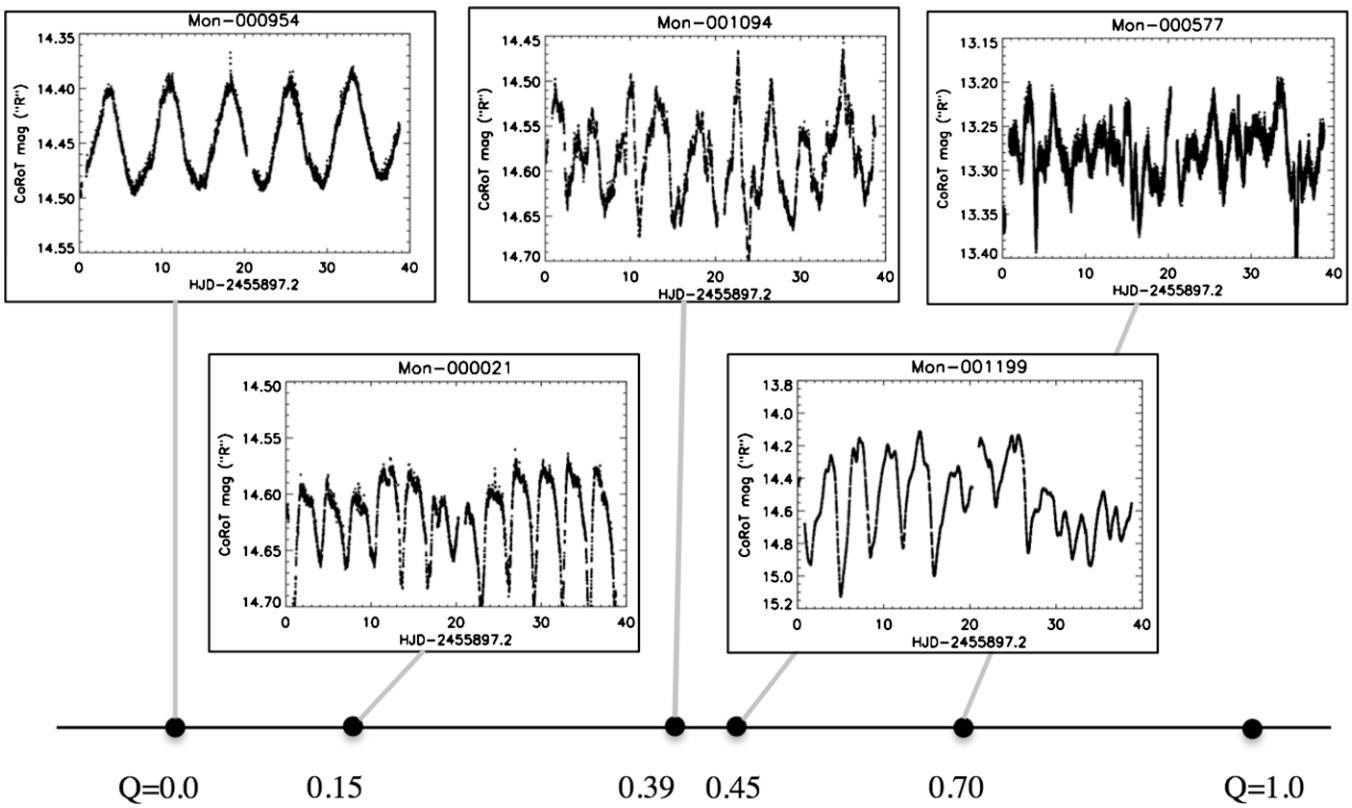

Figure 29. *CoRoT* light curves with representative values of the Q parameter, ranging from periodic (Q = 0–0.15) to quasi-periodic (Q = 0.15–0.5) to aperiodic $Q > 0.5$.

when the uncertainty is an overestimate). However, for light curves that appear to contain multiple sources of variability, the value is larger, ∼0.15–0.60. Light curves with no detectable periodicity have Q values of ∼0.6–1. Examples of different Q values are shown in Figure 29. We will test the dependence of Q on parameters such as period and time sampling in future work.

As an independent check on the periodicities, we note whether the corresponding peak in the Fourier transform periodogram exceeds the local noise level by at least 4.0. This criterion was put forth by Breger et al. (1993) as indicating a 0.1% false alarm probability; see Cody & Hillenbrand (2010) for further discussion. All of the periodic sources and many of the quasi-periodic sources have significant periodogram detections. A more extensive analysis of the periodic sources in the 2011 *CoRoT* sample will be presented in a forthcoming paper in the context of an updated rotation rate analysis for NGC 2264.

Once a significant periodic or quasi-periodic behavior has been identified and the phased trend subtracted out of the light curve, we recompute the periodogram to assess whether further periodicities are present. We once again use the criterion of periodogram local signal-to-noise ratio greater than 4.0. We mask out all frequencies associated with harmonics of the first detected signal, as well as the aliases. The frequencies of aliases are determined by overlaying on the primary peak the window function associated with the periodogram. If one or more significant signals remain outside of the masked values, we then repeat the period search as outlined above.

We report the results of our period search in Table 4, noting in the morphology column which objects are significantly periodic, quasi-periodic, and multi-periodic. We identify two optical light curves with multiple periodicities (Mon-000434 and Mon-000164), as well as one infrared light curve with two periods, only one of which is observed in the optical (Mon-001181). These could indicate binary systems in which both stars show spot modulation.

Among the stars that are periodic or quasi-periodic, the distributions of periods in the optical and in the infrared both peak near 5 days, but we find a significant dearth of infrared periods beyond 9 days compared to a steady decline in the number of optical periods out to 15 days. Of note, some of the infrared periods may originate at the stellar surface, if stellar emission dominates the disk flux at these wavelengths (as is the case for very weak disks).

6.3. Light-curve Flux Asymmetry

In addition to the cases of quasi-periodicity, we observe that many of the light curves are asymmetric with respect to a reflection along the magnitude axis. Some stars have prominent downward flux dips, while others have abrupt increases (see Section 5). We believe that this behavior is connected with the physical mechanisms causing variability. To quantify the degree of flux asymmetry, we have developed a metric, M. To determine its value, we first select the 10% highest and 10% lowest magnitude values in each light curve, after removal of 5σ outliers. This process is carried out by first smoothing the light curve on 2 hr timescales (*CoRoT*) or 6 hr timescales (for the more sparsely sampled IRAC data) and subtracting the smoothed trend from the raw data. Outliers are then measured on the residual light curve. After their removal, we compute the mean of the remaining points and compare with the median of the *entire* outlier-filtered light curve. We define the asymmetry metric via

$$M = (\langle d_{10\%} \rangle - d_{\rm med})/\sigma_d, \quad (7)$$

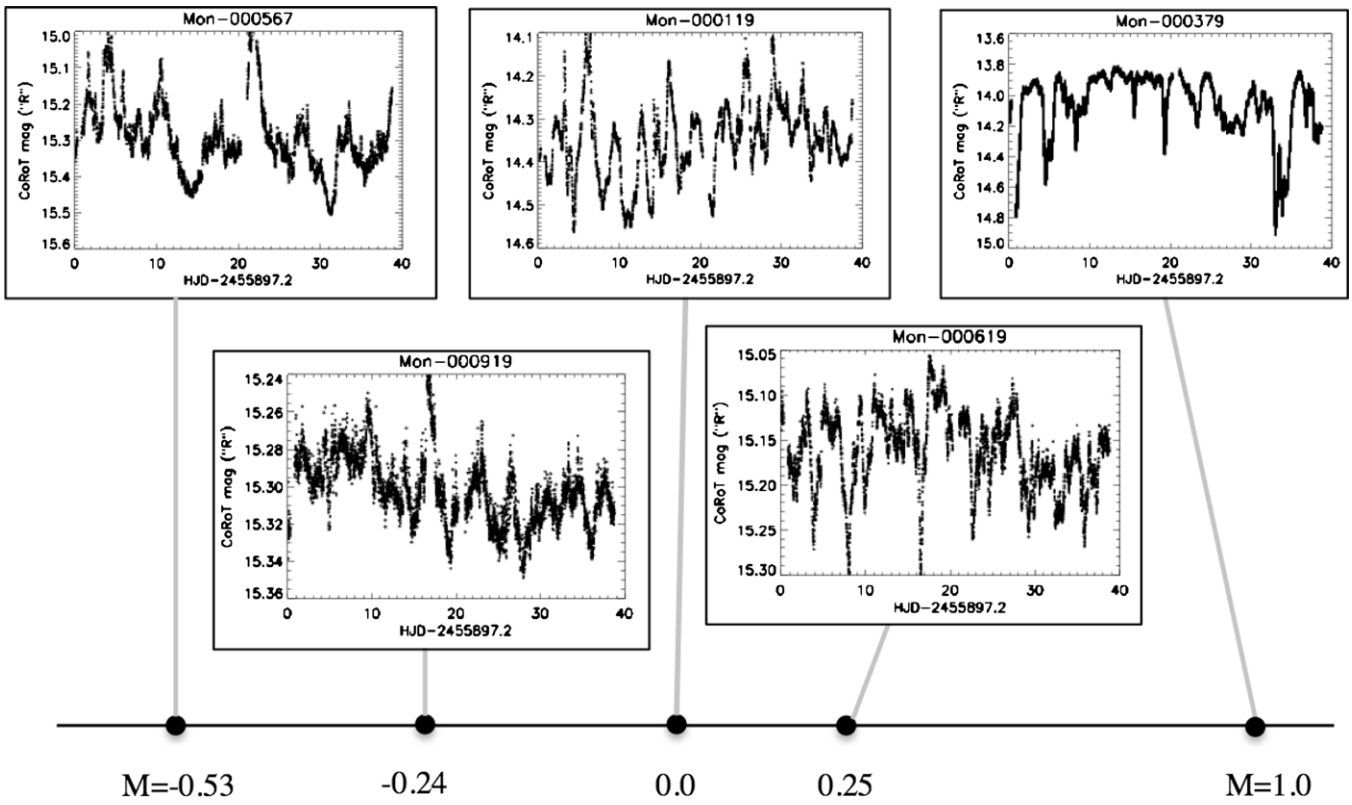

Figure 30. *CoRoT* light curves with representative values of the M parameter, ranging from bursting ($M < -0.25$) to symmetric ($M = -0.25$–0.25) to dipping $M > 0.25$.

where $\langle d_{10\%} \rangle$ is the mean of all data at the top and bottom decile of light curve, $d_{\rm med}$ is the median of the entire light curve, and σ_d is its overall rms.

In some cases, there is a clear asymmetry in the light curve, but it is superimposed on a longer timescale trend. Our asymmetry metric is only sensitive to asymmetries on timescales less than about half the light-curve duration, or 15–20 days. We therefore remove trends on longer timescales by subtracting out a smoothed version of the light curve before computing M. We find that a smoothing window of a few days is sufficient; in cases where short-term light-curve features were oversubtracted, we retain the M value computed on the raw data. These cases were identified visually comparing the raw light curve with the long-term trend overplotted. All light curves were also visually inspected to determine which value was most appropriate.

We encounter a range of M values in our disk-bearing data set, from approximately -1 (prominent upward flux peaks) to just over 1 (flux dips). Examples are shown in Figure 30. Examining the light curves by eye, we observe the most obvious asymmetric behavior to occur for values of M greater than 0.25, or less than -0.25.

6.4. Division of Light-curve Morphologies by Q and M

The M metric, in combination with timescale (Section 6.5) and the periodicity measure, Q, enables us to quantitatively retrieve the morphology classes that were first established by eye and that presumably represent different variability mechanisms. We plot Q against M in Figure 31, along with suggested boundaries to divide the different variability types. Examining the classifications made by eye (color-coded points), we find that the selected boundaries in Q (0.11, 0.61) and M (± 0.25) are quite successful in separating the variability sample into classes. They appear slightly less useful in the infrared since many more sources in this band vary on long timescales and relatively fewer exhibit dipping or bursting behavior. The lower infrared cadence may play a role here as well. Nevertheless, the fact that two parameters can divide our sample so well into the predetermined groups is promising for future variability classification efforts based on sparser data.

The Q–M diagram reveals several facets of the variability in our sources. First, while we have selected boundaries between different classes, the statistics show that there is a continuum of light-curve behavior along both the Q and the M axis. This suggests that sources on the boundaries of variability classes may be characterized by multiple physical mechanisms. Second, the Q–M diagram displays several areas devoid of points. There are relatively few variables that are both bursting and periodic. This may point to the stochastic nature of accretion. Likewise, there are relatively few dipper objects with highly periodic variability. The highest amplitudes of these light curves correlate with unstable variability patterns, such that they are quasi-periodic but not periodic.

6.5. Aperiodic Timescales

Timescale is an important quantifiable aspect of our light curves. Visual inspection of the data reveals that some objects oscillate quite rapidly (i.e., multiple zero crossings in a week), while others show only long-term trends. We wish to define a timescale measure for the purposes of examining correlations with physical parameters. While it is easy to attach a value to the periodic and quasi-periodic light curves, a timescale for aperiodic stars is not so obvious. Tools such as the ACF and periodogram have traditionally been used to assess whether there is a characteristic timescale for aperiodic variability.

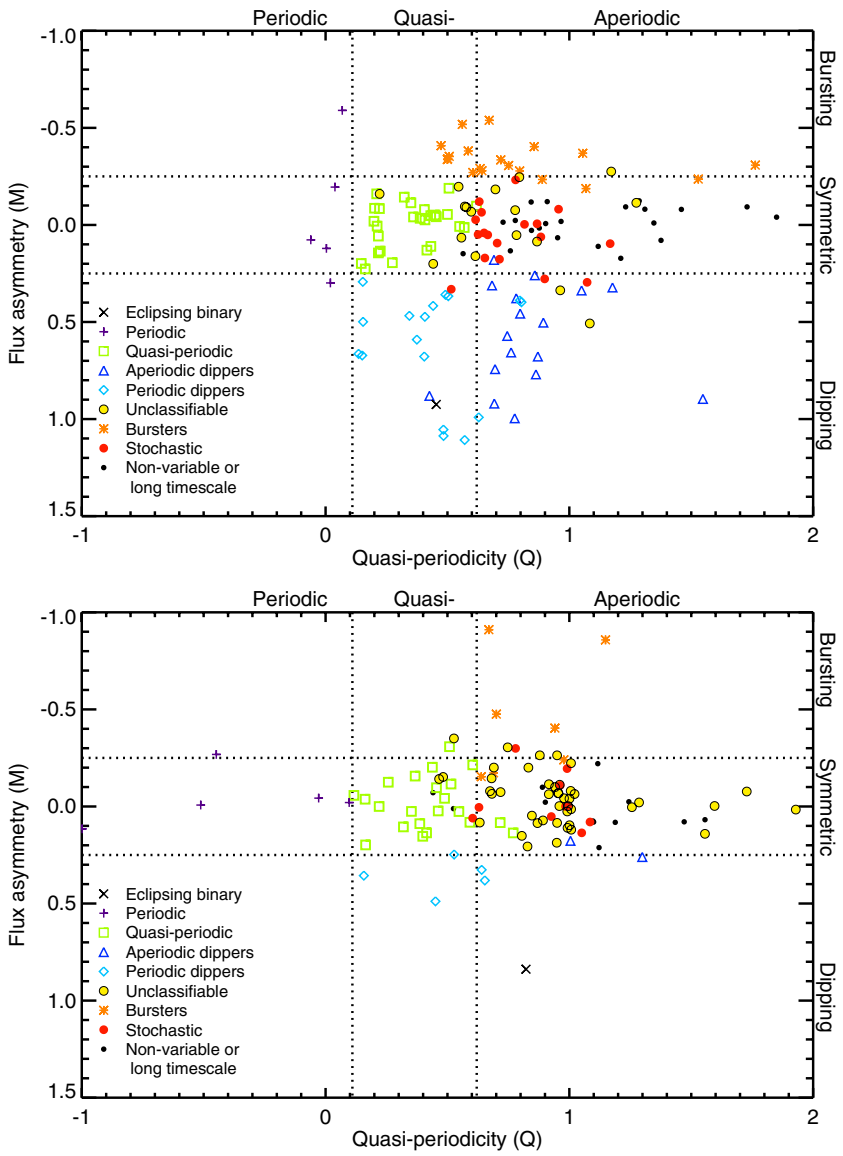

Figure 31. Top: light-curve morphology classes, as divided by the quasi-periodicity (Q) and flux asymmetry (M) parameters for optical light curves from *CoRoT* in our disk-bearing sample. Color coding indicates the variability classification chosen by eye, before statistical assessment. The eclipsing binary is not strictly periodic because its light curve contains aperiodic fluctuations out of eclipse. Bottom: same as the top, but for infrared light curves acquired from *Spitzer*/IRAC. The pileup of points at $Q \sim 1$ occurs because the subtraction of an incorrect phase curve tends to leave the rms unchanged from its raw value.

(A color version of this figure is available in the online journal.)

However, it is not immediately clear what amplitude level one should choose to extract a timescale from the ACF, or how to determine whether there is such a special time at all. Furthermore, the time sampling and baseline may strongly influence the appearance of the ACF.

We have adopted a different strategy, which is to identify the median timescale separating the largest consecutive peaks in a light curve. This process consists of two steps: (1) for each light curve, we calculated how the inferred timescale varies as a function of the amplitude threshold applied in selecting peaks to calculate timescales between; and (2) we collapse this set of timescales into a single value representing the highest amplitude variations within the light curve. For the first step, we calculate timescales for amplitudes as small as the light curve's noise level and as large as the light curve's full range (i.e., the absolute maximum minus the absolute minimum, after filtering for outliers). For each of these values, we run through the light curve, marking maxima and minima that differ from surrounding peaks by more than that amplitude (see the top and middle panels of Figure 32). We start by selecting the absolute maximum and count all peaks preceding it. We then repeat the process to identify peaks succeeding it. From this "PeakFind" algorithm, we estimate a characteristic timescale for each amplitude by computing the median time difference of all consecutive pairs of peaks and then multiplying by two. The normalization by 2.0 ensures that the derived timescale will match the period for periodic objects. This process results in a trend of timescale versus amplitude, which we invert to amplitude as a function of timescale, as shown in the bottom panel of Figure 32. We note that this function is not necessarily monotonic, because of the smaller number statistics in the case of large amplitudes and small numbers of peaks.

For many of our light curves, the PeakFind timescale reaches a maximum value that is much shorter than the duration of

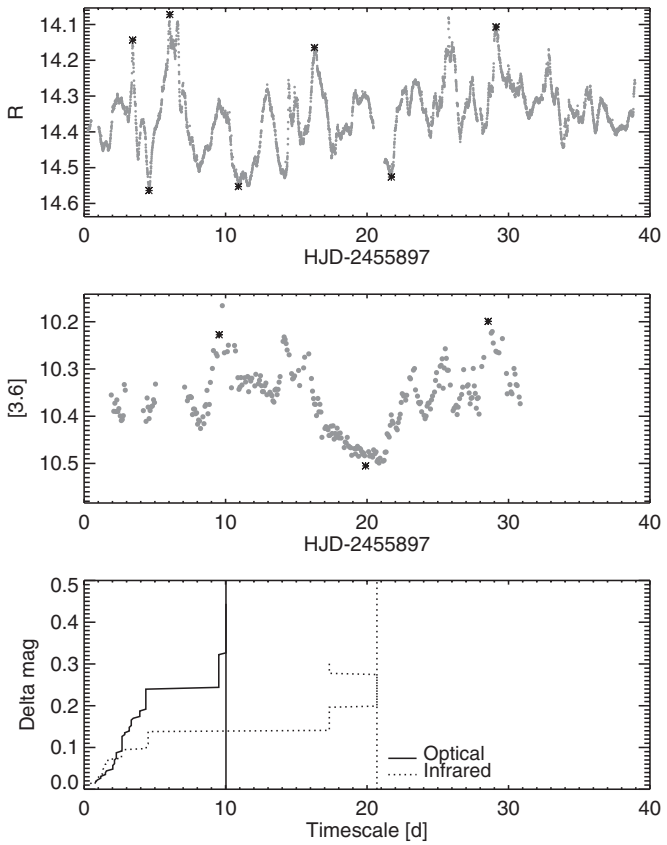

Figure 32. Example of how we compute optical and infrared timescales for the aperiodic variable Mon-001054. The raw *CoRoT* (top) and IRAC 3.5 μm (bottom) light curves are shown in gray, whereas peaks selected as being separated by at least 80% of the maximum minus minimum of the light curve are marked with black asterisks. The bottom plot shows the resulting amplitude-timescale trend, with the 80% value marked with vertical lines. See the text for further details.

the light curve. This implies that the full variability amplitude is accounted for by a relatively short timescale phenomenon. To extract a single timescale from the trend—the second step in the process—we note the maximum peak-to-peak amplitude of the light curve and adopt the timescale corresponding to 70% of this (i.e., the vertical lines in Figure 32). If this timescale is comparable to the duration of the time series, or ∼30–40 days, then it is a lower limit on the true maximum variability timescale. We emphasize that this "70% amplitude" timescale is not necessarily a *characteristic* timescale, since variability may be produced on a continuous spectrum of timescales, and we are not sensitive to those longer than 30–40 days. However, for fairly rapid variability we consider it an approximate upper limit to the timescales on which variability is generated. Simulations using damped random walks show that, for aperiodic signals with characteristic timescales of 0.1–5 days and amplitudes of 0.2 mag or more, the peak-finding timescale is well correlated with the true timescale on average but shows scatter comparable to the true timescale for any individual source (K. Findeisen 2014, in preparation). Therefore, the timescales are best interpreted in an ensemble sense. Using them as guidance, we are able to distinguish between aperiodic light curves that oscillate on day to week timescales and those that wander up and down over the course of a month or more. We find that the distribution of aperiodic stochastic timescales from the PeakFind method centers around 5–10 days, indicating that short timescales are dominant in the optical, at least among the spectral types encompassed by our data set.

With two types of timescales (i.e., quasi-periodic and aperiodic) in hand for the variables in our sample, we can compare them with the rms values in the optical and infrared, as shown in Figure 33. Separating objects into their variability type (aperiodic or quasi-periodic), we do not find any obvious correlations, apart from a subtle rise in variability amplitude from 1 to 5 day timescales. Aperiodic infrared variables show higher amplitudes than the periodic varieties, with many of the former achieving rms values between 0.1 and 0.2 mag. Both optical and infrared variables achieve their highest quasi-periodic amplitudes on timescales between 5 and 10 days. The amplitudes of aperiodic light curves have a much wider distribution of amplitude versus timescale.

7. CORRELATION OF OPTICAL AND INFRARED VARIABILITY

We expect correlation between the optical and infrared variability in cases where the dominant variability mechanisms take place on or near the stellar surface. We predict much less correlation when the mid-infrared flux is dominated by disk emission. Ultimately, the degree of optical/IR correlation is a function of many factors, including viewing angle, number of distinct variability mechanisms and their amplitudes, disk flux, and disk geometry (e.g., inner wall radius, flaring, gaps). While we do not have enough information to break these degeneracies, we can examine the multiwavelength correlation properties in the context of the different light-curve morphologies that we have identified. In Section 8, we explore further connections with available stellar and disk properties.

Of particular interest is how the statistics compare in the two different bands, optical and infrared. To portray the diversity of light-curve behavior, we have plotted in Figure 34 the rms values of each light curve. There are no distinct clusters in this diagram, and none of the morphology groups described in Section 5 occupy any particular region, apart from periodic and unclassifiable variables having preferentially low rms values. The latter are likely noise dominated, whereas the former could be the result of cool starspots, for which rms values of order a few percent are consistent with previous results in the literature.

We also present in Figure 34 a comparison of the inferred optical and infrared timescales for aperiodic variables. The values in both bands cover most of the parameter space from 1 to 40 or more days. Short-timescale behavior in the optical usually corresponds to relatively short timescale behavior in the infrared, but short-timescale behavior in the infrared does not necessarily mean a short timescale in the optical.

7.1. Optical/Infrared Correlation via the Stetson Index

To measure in detail the degree of correlation between optical and infrared time series, we first interpolate each *CoRoT* light curve onto the same time stamps as the IRAC 3.6 and 4.5 μm mapping data. Since the *CoRoT* observations were obtained at such high cadence, the effect of interpolation on the variability is negligible. The result is pairs of optical and infrared light curves with typically ∼300 points.

We have performed a cross-correlation of the *CoRoT*/IRAC sets using the Stetson index (Stetson 1996), as well as subtraction to generate color trends. We find that many sets of light curves are well correlated for part of the time series but

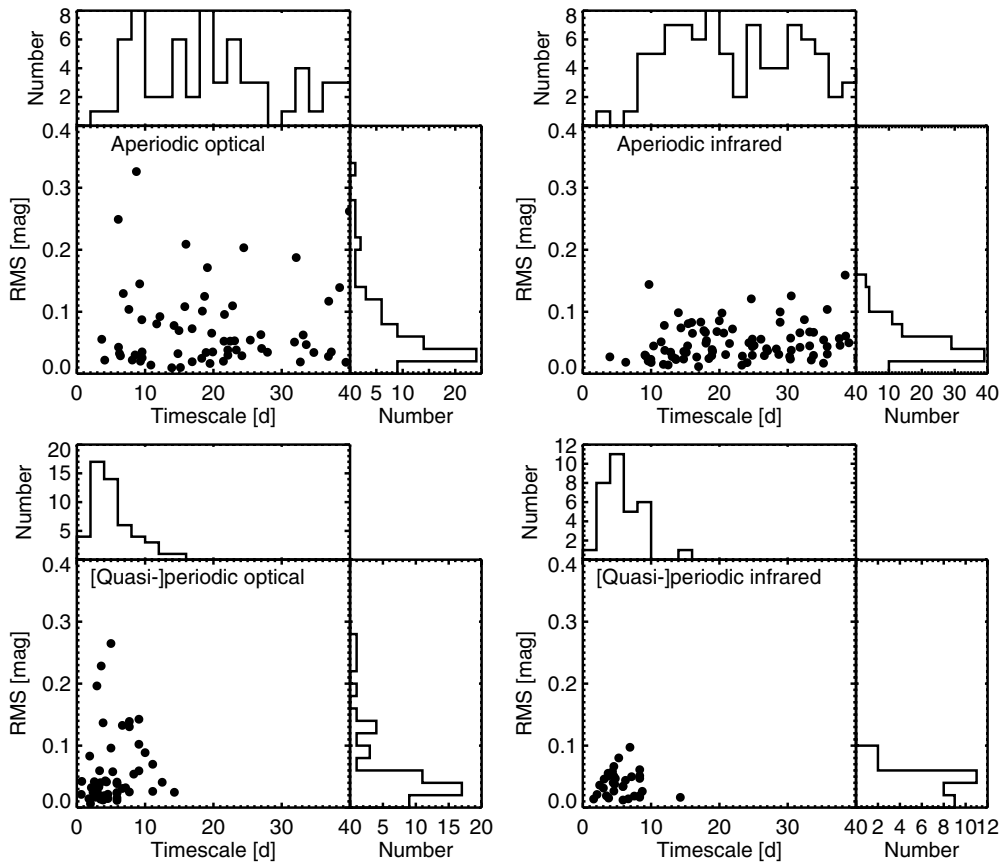

Figure 33. Timescale vs. rms, separated into [quasi-]periodic and aperiodic behavior, in both bands. We also display the distributions of each set of points.

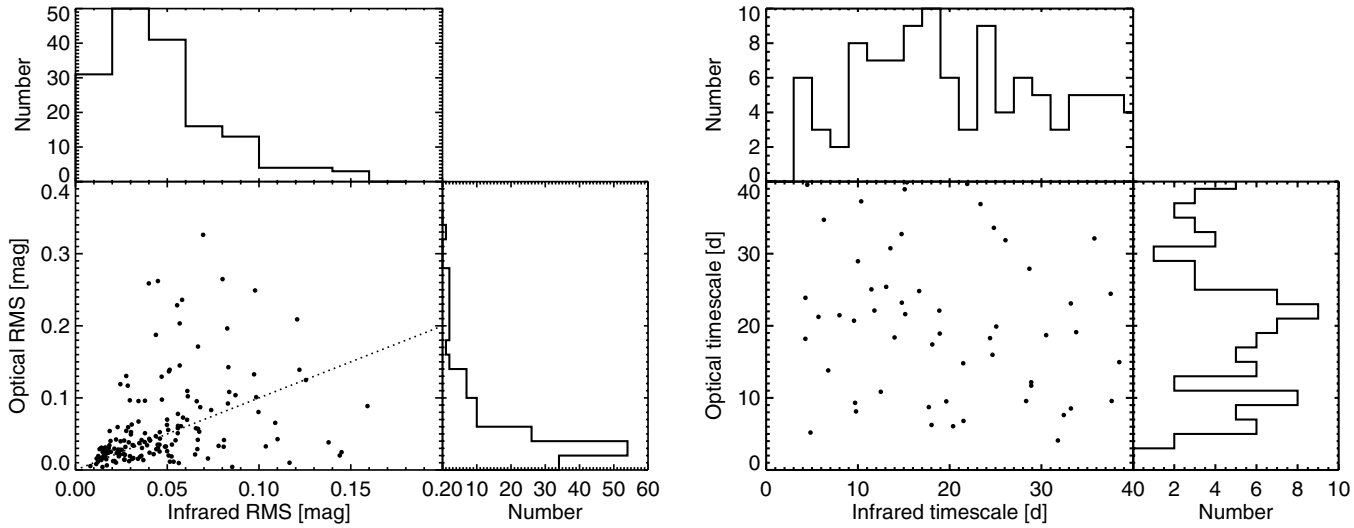

Figure 34. Left: correspondence between optical and infrared rms values for all objects in our data set. Right: optical and infrared aperiodic timescales in each band. These are quantized, because the aperiodic timescale involves division of the total time baseline (the same for all sources) by the number of peaks larger than a particular amplitude. Here the points at timescales of ∼40 days are lower limits. Timescales are not shown for objects that have a quasi-periodic optical or infrared light curve, since we find that the detected periods, if present in both bands, are always similar.

less correlated or varying with a different color slope in other parts. This makes it difficult to quantify correlation via a single parameter.

As an alternative, we have computed a time-dependent Stetson index by comparing 20 point sections (1.7 days) of the IRAC and interpolated *CoRoT* light curves. The 20 point step size was motivated by the typical duration of short-timescale light-curve fluctuations, which is a few days. Well-correlated light curves should display a positive Stetson index with little dependence on time. Light curves that are correlated at some times but not others will instead display a fluctuating Stetson index, reaching large values at some times and dropping to zero or below at others. To differentiate this behavior from chance correlation between sections of two light curves, we have performed simulations using time series from different stars. We match optical and infrared light curves from *different* stars,

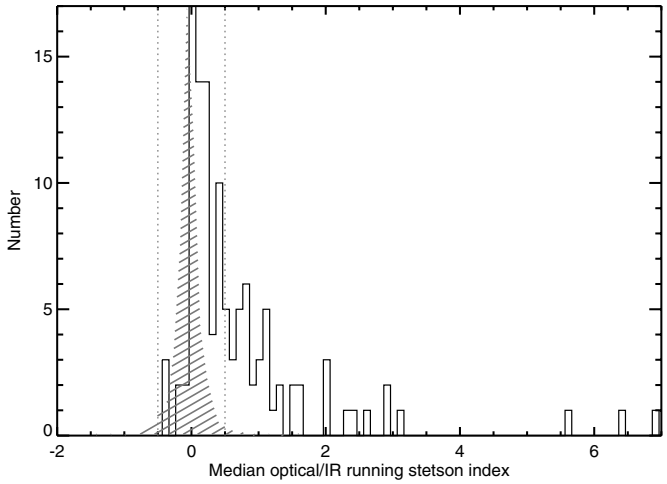

Figure 35. Distributions of median running Stetson index for pairs of *CoRoT* and IRAC light curves in our disk-bearing sample. Here the values from the 3.6 and 4.5 μm bands are averaged. The hashed region shows the distribution for randomly selected light-curve pairs, and dotted lines mark the 95% confidence interval for random Stetson indices. Values greater than 0.6 indicate well-correlated optical and infrared light curves.

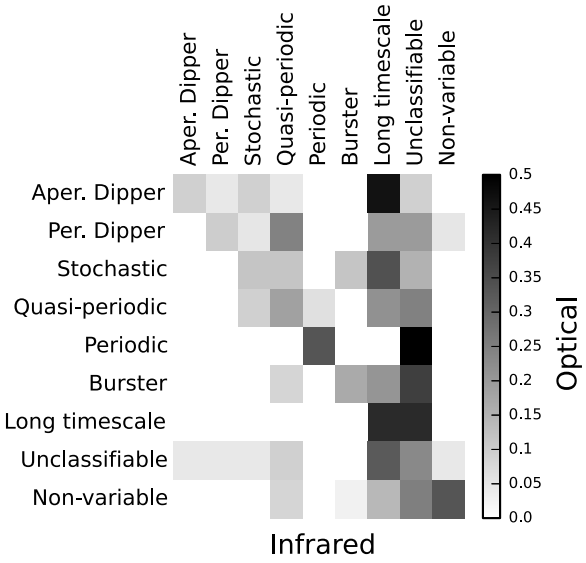

Figure 36. Correlation matrix between assigned optical and infrared variability types. For each optical morphology class, this diagram shows the fractions of objects that occupy each infrared class. It should be read along rows. For example, just over 10% of optical variables classified as aperiodic dippers are also aperiodic dippers in the infrared; the reverse (i.e., 10% of aperiodic infrared dippers being aperiodic dippers in the optical) is not necessarily true. Continuing along the same row, we also see that just over 50% of aperiodic optical dippers are long-timescale variables in the infrared. The remaining 34% of optical variables are a mixture of periodic dipper (∼6%), stochastic (∼11%), quasi-periodic (∼6%), and unclassifiable (11%) in the infrared.

thereby guaranteeing that there should be no true correlation. Only light curves with at least 250 points are allowed, since the more sparsely sampled HDR mode light curves will have a broader Stetson index distribution. One thousand simulations of randomly matched light-curve pairs revealed that 95% of uncorrelated light curves have a median running Stetson index between −0.5 and 0.5 when sampled at every 20 points. Repeating the simulations on HDR light curves for every five points, the value increased to 1.0. We also ran the simulations for a sampling step size of 50 points, but found that the running Stetson index showed more systematics, and its median was less consistent between the two IRAC channels, despite flux behavior being nearly the same in these bands. The distribution of median running Stetson index for *CoRoT* light curves paired with IRAC light curves is shown in Figure 35.

We report the median running Stetson index for all objects in Table 4. Stars with large negative running Stetson indices exhibit anticorrelated behavior in the optical and infrared.

The fractions of correlated versus uncorrelated and anticorrelated light curves may indicate the percentage of sources in which variability is disk dominated. To determine this number, we assemble the distribution of median running Stetson indices in Figure 35, along with the distribution expected for uncorrelated light curves, as derived in our simulations. Although we have drawn a cutoff of 95% confidence, it is clear that the set of Stetson indices is skewed with respect to the distribution defined by the simulations. We conclude that there is low-level optical/infrared correlation in many of the objects; this is not surprising since stellar variability will generally have a small infrared contribution due to emission from the long-wavelength tail of the star's SED. In general, however, the larger infrared contribution from the dust means that variability originating in the disk will dominate the light curve.

Overall, 38% of our sample shows evidence of correlation at the 2σ level, and 58% shows correlation at the 1σ level. There is generally a correlation between the shapes in the optical and those in the infrared, but in many cases it is quite weak (i.e., it consists of transient dips or bursts matching up). To further illuminate the relationship between optical and infrared behavior, we have plotted a correlation matrix comparing the morphologies assigned in each band. Figure 36 confirms a low-level optical/infrared correlation at best in most sources.

7.2. Well-correlated Optical and Infrared Variability

We have identified light curves that are correlated in the optical and infrared by selecting those with a large median running Stetson index. Some of these light curves display partial correlation in that the infrared flux trends mimic those in the optical over part of the time series, but at other points there is no resemblance between the two bands.

There are two scenarios for correlation of behavior in the optical and infrared. First, if there is only one variability process affecting the star, then the light curves should exhibit a relatively simple wavelength dependence. Second, if the disk flux dominates in the infrared bands but variability reflects mainly reprocessed stellar light, then we would also expect to see correlated behavior, either in or out of phase. We test these scenarios in Section 8 by comparing the Stetson index to measures of disk to star flux.

We have identified three broad categories of morphological behavior among the well-correlated light curves: optical dippers, bursters and stochastic stars with similar infrared amplitude, and optical stochastic stars with lower amplitude infrared light curves. A selection of these is presented in Figure 37, while optical and infrared light curves for the entire 162 member disk-bearing data set are provided in the Appendix, Figure 49. Some of these have behavior that makes sense in the context of the extinction-dominated variability model. Here, fluctuations in the light curve are caused by changing amounts of dust blocking the star, and the optical/infrared correlation simply reflects the wavelength dependence of extinction, diluted by any flux from the inner disk. Confronting this model are the two objects Mon-000183 and Mon-000566, which display *deeper* dips in the infrared than in the optical. This behavior is not expected from

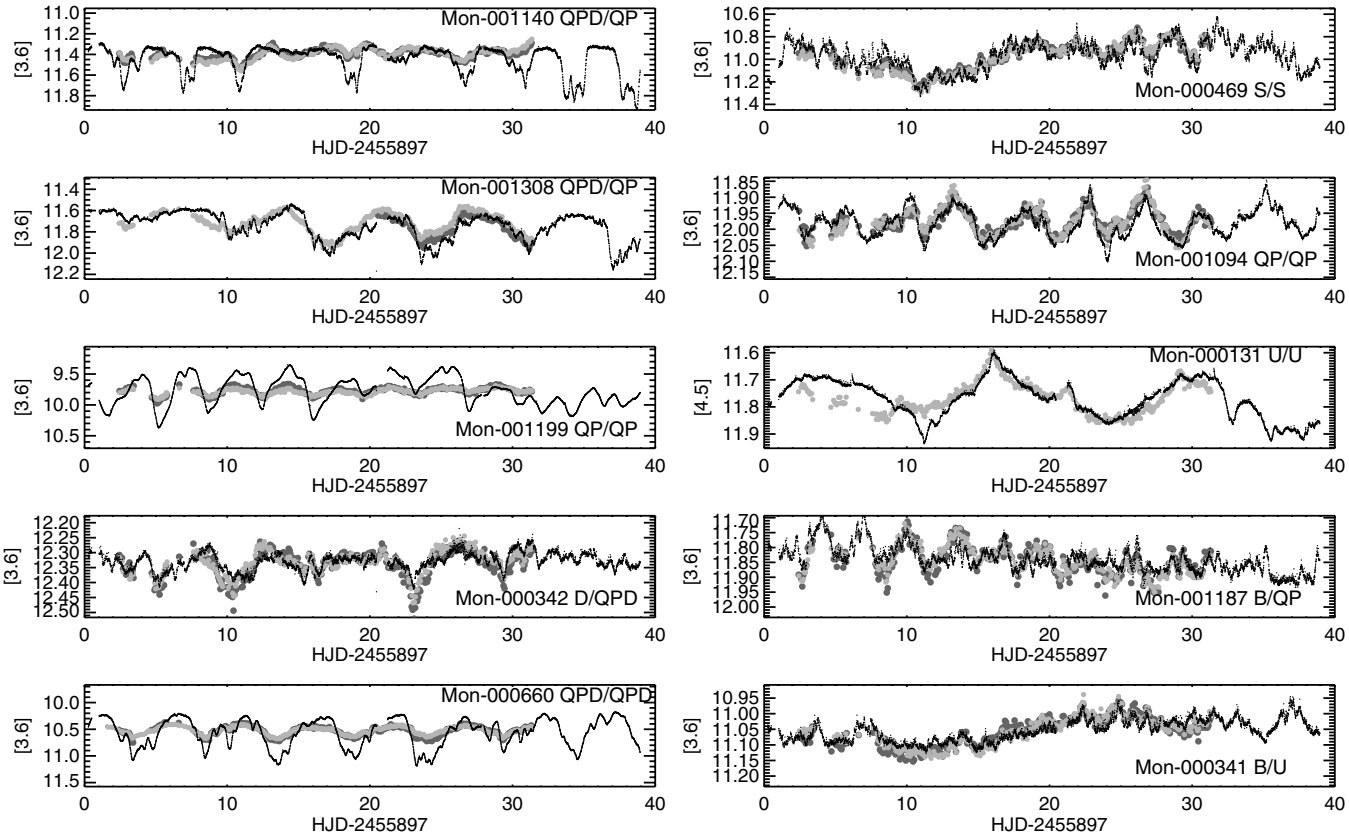

Figure 37. Light curves with correlated optical and infrared behavior. Small black points are *CoRoT* data, light gray points are 3.6 μm data, and dark gray points are 4.5 μm data (sometimes hidden behind the 3.6 μm points). Labels show the Mon ID along with the optical and infrared morphologies, respectively; morphology abbreviations are the same as in Table 4.

any standard extinction law and may require unique geometry, such as occultations of the disk by itself (i.e., the front blocks flux from the back wall).

The remaining set of well-correlated optical and infrared light curves displays very similar morphology and amplitude in each band. Half of these are members of the optical bursting class, and the rest are stochastic or unknown morphology. Strong optical/infrared correlation for these would be expected if flux changes are reflective of increases in accretion, the radiation from which is absorbed and reemitted by the inner disk.

7.3. Uncorrelated Optical and Infrared Variability

Some 62% of the variable light curves in our sample display little correlation between the optical and infrared bands. In these cases, there are likely two or more variability mechanisms at work, connected separately with the star and the disk. Alternatively, a single variability mechanism could be at work if it only affects one wavelength region. Since the infrared flux is in most cases not dominated by stellar or accretion emission, disk-driven mechanisms are necessary to explain the often large-amplitude ($\sim$0.1 mag) infrared modulation on week or longer timescales. One possible origin is magnetic turbulence, proposed by Turner (2013) to modulate the inner disk scale height and thereby alter the observed mid-infrared emission.

We have assembled a set of the most prominent uncorrelated optical and infrared behavior in Figure 38. The wide range of morphologies in both bands is evident. Particularly interesting examples of uncorrelated behavior occur in Mon-000185, Mon-000273, Mon-000357, Mon-000876, and Mon-000928, for which there is almost no optical variability, but high-amplitude (0.1–0.3 mag) infrared light-curve excursions on 5–10 day timescales. We have checked the individual images of these objects for erroneous cross matching of *CoRoT* and *Spitzer* sources, but in all cases there is no nearby star that could be a better match. This type of behavior occurs in a few percent of our disk-bearing stars.

The selection of objects with uncorrelated behavior is particularly helpful for investigating the distribution of infrared variability timescales, since we do not have to worry about much contamination from optical processes. We have measured the aperiodic infrared timescales of stars with median running Stetson indices less than 0.6. As illustrated in Figure 39, the distribution displays a clump around 5–15 days, although there are many additional objects with infrared timescales at 20 days and longer. The individual examples of rapid infrared changes, as well as the overall distribution, lend support to the idea that disk structural changes may be occurring close to or even faster than the local dynamical timescale in some cases. The latter is between a few days and a few weeks, depending on stellar mass and dust properties.

7.4. Inverse Correlation: Optical and Infrared Phase Shifts

A prediction of YSO variability models for edge-on systems (e.g., Kesseli et al. 2013) is that inner disk regions may receive non-uniform illumination from the central star, thereby reradiating infrared flux in a time-variable manner. An example is an accretion hot spot on the stellar surface, radiation from which interacts only with the region of the inner disk on that hemisphere of the star. In this case, we expect to observe the infrared emission 180 degrees out of phase with the hot spot

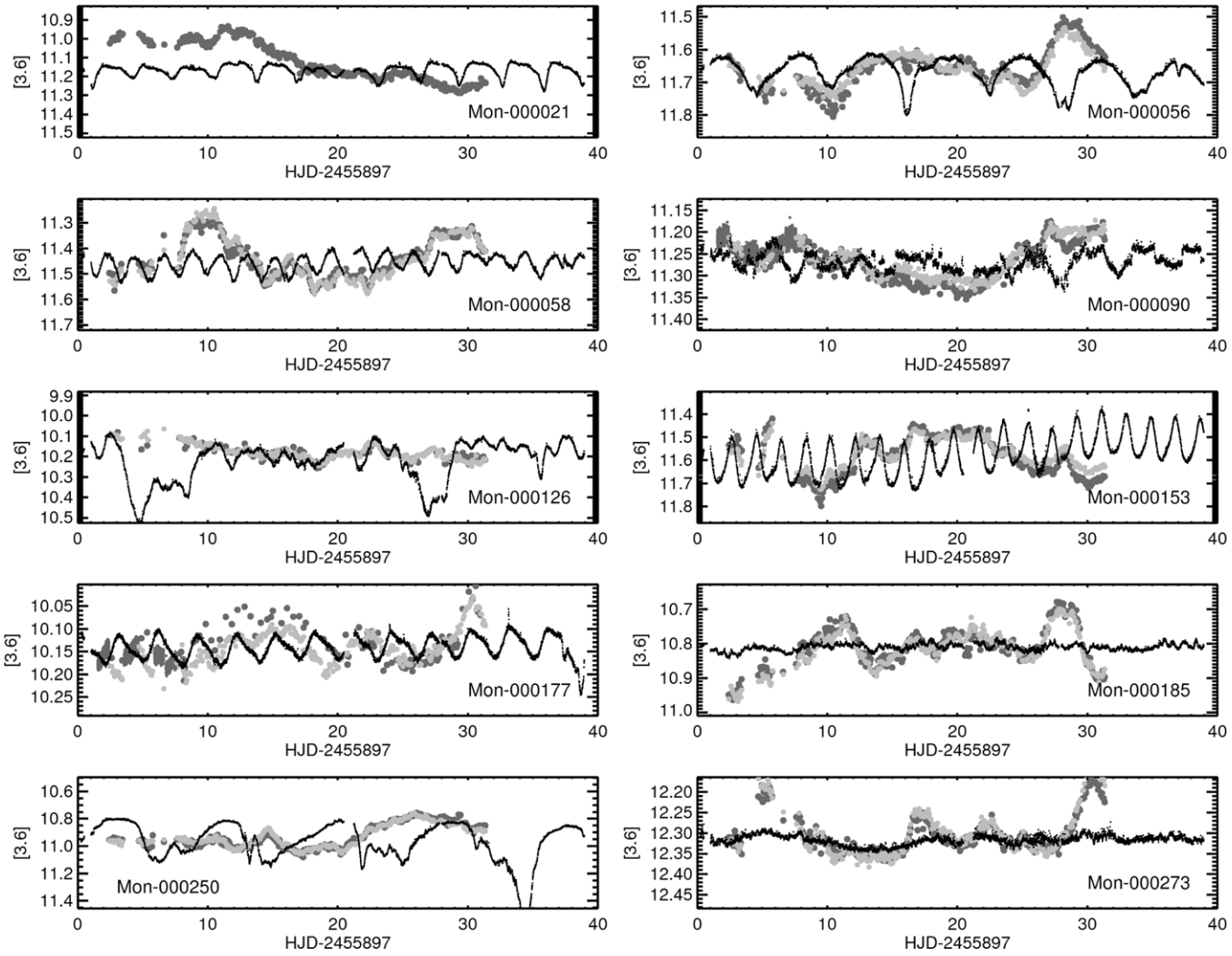

Figure 38. Light curves with uncorrelated optical and infrared behavior. Small black points are *CoRoT* data, light gray points are 3.6 μm data, and dark gray points are 4.5 μm data (sometimes hidden behind the 3.6 μm points).

signature, since we do not view the heated region of the disk wall until it has rotated behind the star.

Surprisingly, we encounter very few such examples of optical/infrared phase shifts in our time series. The only object with a clear inverse relationship between the two bands is Mon-001031. Mon-001132 displays a more subtle phase lag, but this shift does not appear to be constant across the entire observation time. We present the two light curves in Figure 40.

8. VARIABILITY IN THE CONTEXT OF STELLAR AND DISK PROPERTIES

For most of the *CoRoT*/*Spitzer* data set, we have available spectral types, classification of the infrared excess, and optical through infrared photometry enabling determination of position on the H-R diagram. In many cases, we also have measurements of the equivalent width of prominent emission lines, such as Hα. We have correlated the variability properties measured in Section 6 with a number of the above-mentioned parameters and searched for combinations that may offer physical insight.

8.1. Relationship of Variability to Stellar Parameters

The main stellar parameter of interest is the effective temperature, which serves as a proxy for mass. We have estimated this for the 112 stars in our sample that have available spectral types in Table 3. We then plotted the variability properties involving timescale and amplitude against temperature. One might expect infrared variability timescale to scale with temperature since it could reflect dynamics near the sublimation radius, which is in turn dependent on stellar mass. For completeness, we have separated the timescale measurements into quasi-periodic and aperiodic sets, as well as divided them into the two wavelength bands before comparing with temperatures. The correlation diagrams resulting from this exercise are shown in Figures 41. Timescale, whether periodic or aperiodic, does not show any prominent trends as a function of temperature. However, there is a lower envelope to the distribution of aperiodic infrared timescales versus temperature; this could be consistent with the orbital period at the sublimation setting the minimum timescale for disk variability. In addition, the implied lack of a global dependence of the variability timescale on mass does not necessarily mean that there is no relationship between these two parameters. We suspect that there are subclasses of variability that exhibit different behavior as a function of stellar mass. For example, the dipper objects show larger infrared amplitudes in comparison to the optical for preferentially later spectral types. Finally, there may be currently unobservable factors, such as disk inclination, that influence the variability properties.

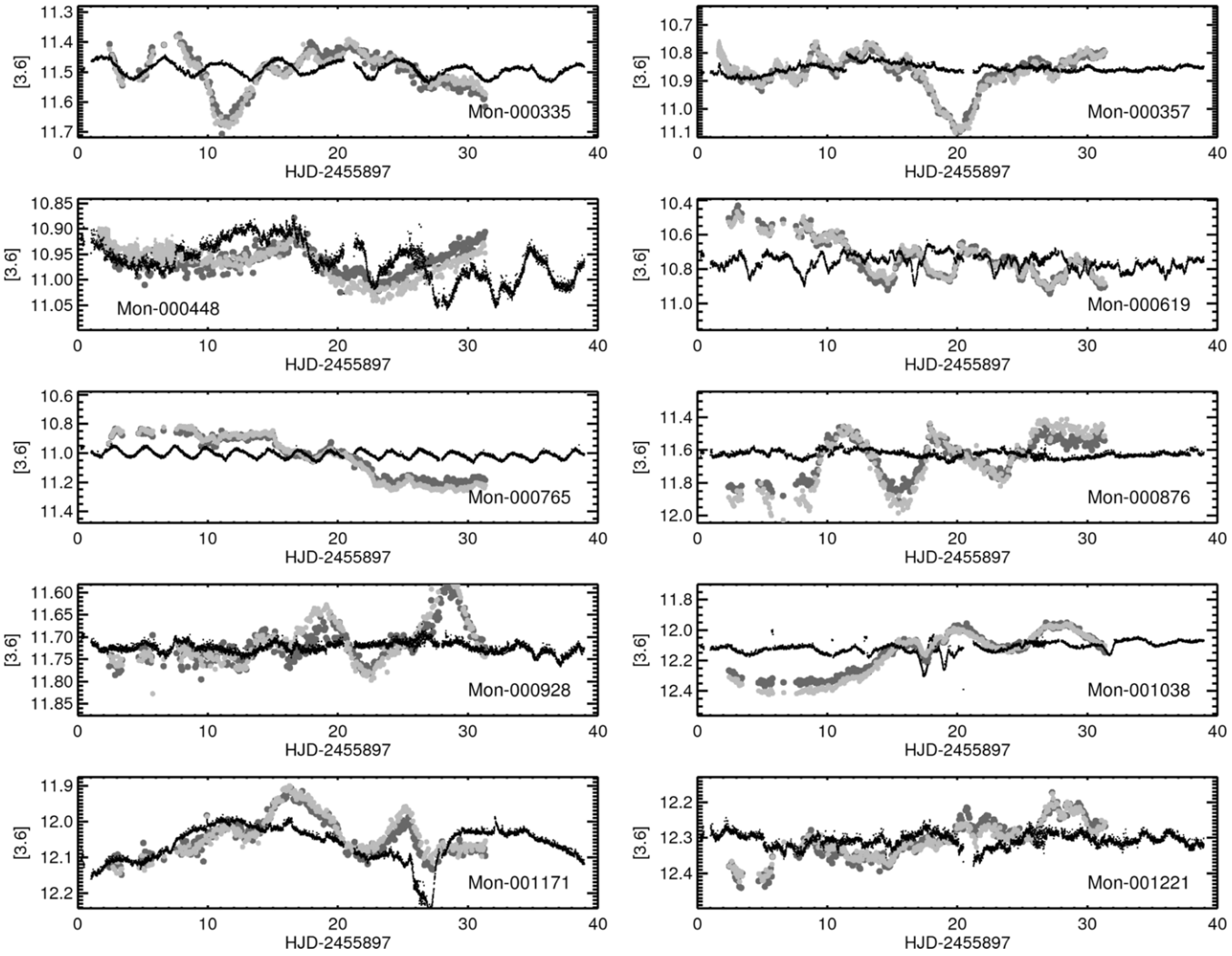

Figure 38. (Continued)

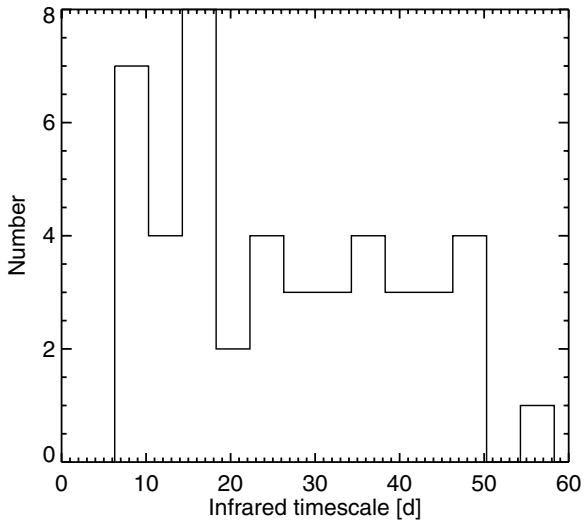

Figure 39. Distribution of timescales measured with the PeakFind algorithm for infrared light curves that are not well correlated with their optical counterparts.

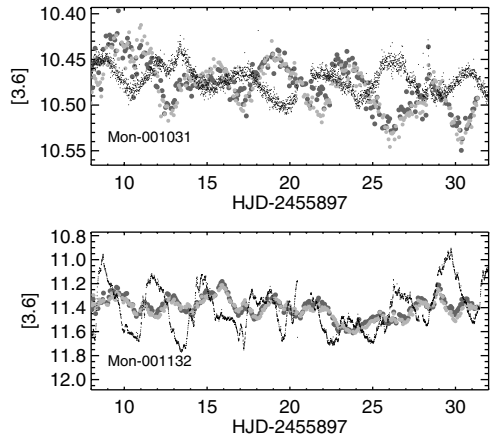

Figure 40. Light curves with potential phased shifts between their optical and infrared behavior. Small black points are *CoRoT* data, light gray points are 3.6 μm data, and dark gray points are 4.5 μm data (sometimes hidden behind the 3.6 μm points).

We have also carried out a similar comparison of variability amplitude versus temperature, as shown in Figure 42. Here, we find the surprising result that aperiodic variability amplitudes are significantly lower around the cool stars in our sample. This trend is the opposite of what one would expect from a detection bias, in which it is harder to detect low-amplitude variability around fainter stars. The effect is stronger in the optical, but also seems to appear in the infrared. This is in contrast to the periodic variability, which shows no appreciable mass dependence. The

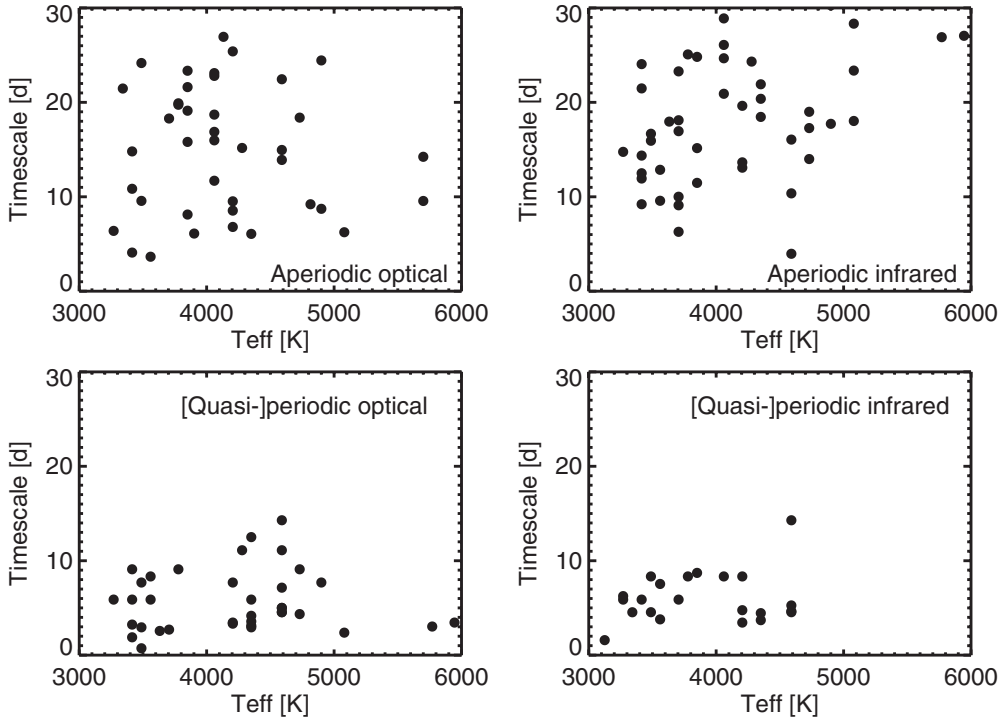

Figure 41. We plot variability timescale against effective temperature (where spectral types are available), as a proxy for mass. We do not see correlations between these two parameters, although the lower envelope of aperiodic infrared timescales is roughly consistent with the orbital period at the disk sublimation radius.

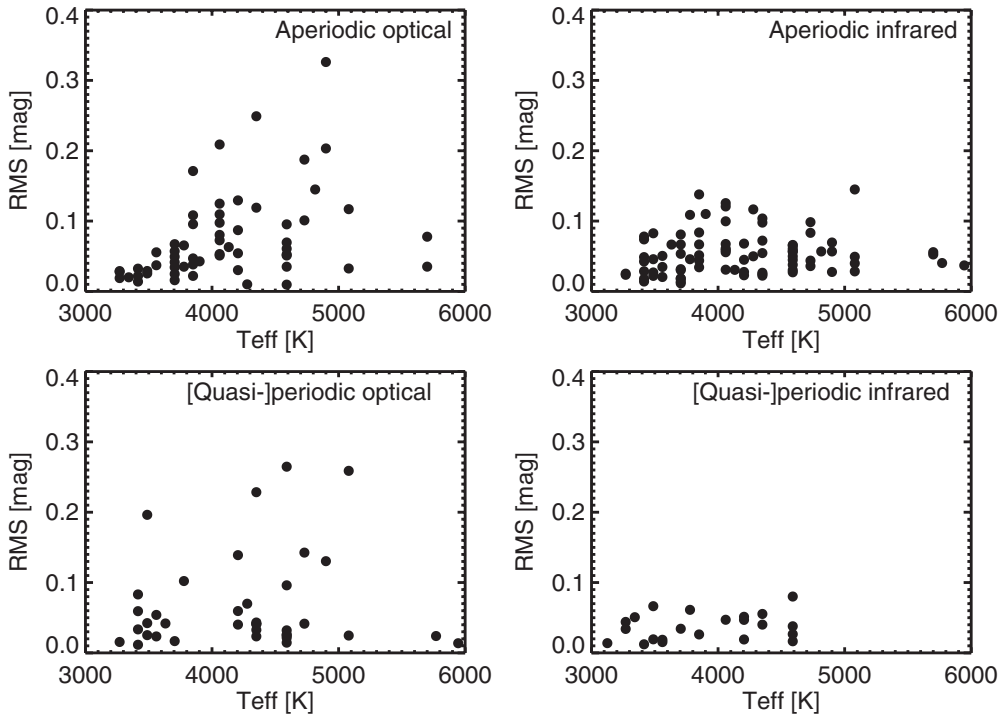

Figure 42. rms vs. stellar effective temperature, for [quasi-]periodic and aperiodic variables in both bands. The amplitudes of optical variability appear to grow with mass, while no such trend is seen in the infrared.

rms/temperature trend in aperiodic variables may reflect a correlation of magnetic field strength and/or configuration with mass. However, this may be contradicted by recent results from Zeeman–Doppler imaging that suggest that the dipole field component *weakens* with increasing mass (e.g., Gregory et al. 2012).

Perhaps the most telling correlation we have noted is the connection between light-curve flux asymmetry (M) and Hα equivalent width. We plot these two parameters in Figure 43. While there is not a one-to-one correspondence between them, it is clear that the more negative M values correspond to stronger Hα emission. This finding supports the idea that the burster

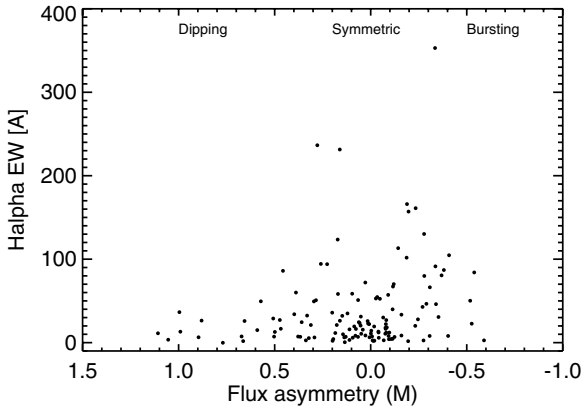

Figure 43. Flux asymmetry (M) against the equivalent width of Hα emission. The more negative M values correspond to bursting behavior in the light curves.

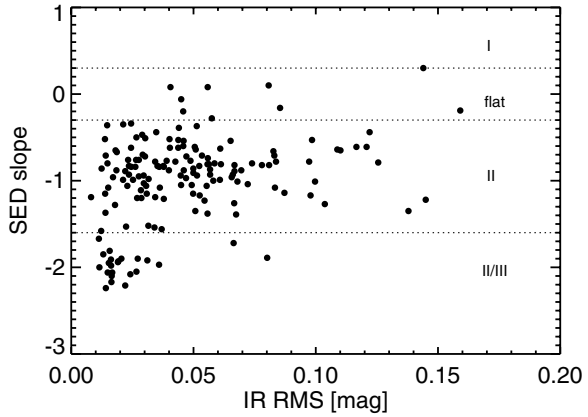

Figure 44. rms value of infrared light curves vs. their SED slope, α. More positive α values are correlated with larger infrared rms, suggesting a relationship between disk variability and evolutionary state. Dotted lines mark the boundaries between various SED classes, which are labeled; most of our sample is Class II.

class of light curves represents the most strongly and unstably accreting stars in our data set (see also Stauffer et al. 2014 for confirmation of this idea).

8.2. Infrared Excess

In addition to searching for global correlations between variability and stellar properties, we can also ask whether variability is well connected to *disk* properties. We first compared the rms light-curve value for infrared variables with the slope of the SED, α (as calculated in Section 2.1). The result, shown in Figure 44, does not display a strong dependence on morphology type, but there does appear to be a subtle lower envelope, with few high-amplitude variables at low α values. This suggests that disks with earlier classes can achieve higher levels of variability, a result that has also been borne out in other clusters (e.g., Morales-Calderón et al. 2009). It also makes sense given that the Class II/III objects in our sample have less dust to generate variability.

We also suspect that the ratio of disk excess to stellar flux plays a significant role in light-curve morphology. As a proxy for this ratio, we have computed the $K-[4.5]$ color of all sources in our sample. We compare this with the median running Stetson index in Figure 45. Surprisingly, there is no strong dependence of optical/infrared correlation on disk strength either. However, the light curves of a number of individual sources do make sense in the context of their SEDs. For example, several stars (e.g., Mon-001094) display well-correlated behavior at similar

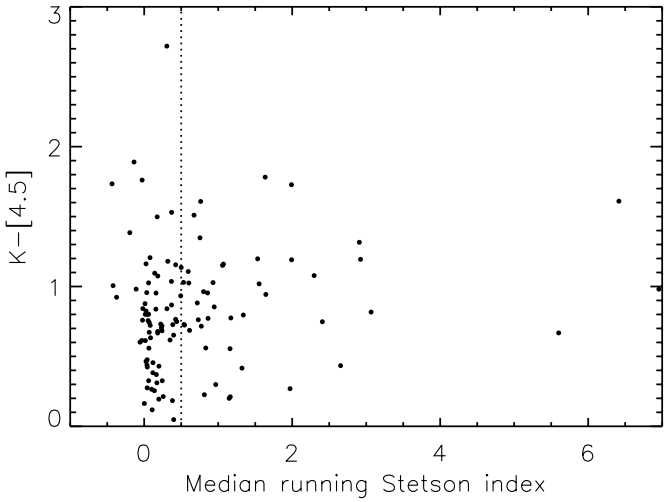

Figure 45. Degree of optical/infrared correlation (i.e., Stetson index) does not have a one-to-one relationship with the strength of disk emission, as parameterized here by the $K-[4.5]$ color.

amplitudes in the two bands. We suspect in these cases that there is a single variability process at work, and it is associated with the stellar surface. The disk, on the other hand, is weak and has little emission compared to the stellar flux in all bands. We see that this is the case from the small $K-[4.5]$ values of these objects. Estimates of their disk to stellar flux ratios in the infrared also support this idea, since the values are less than 10^{-3}.

There are other objects in our diagram for which the high degree of optical/infrared correlation is not expected to relate strongly to the disk flux strength. These are the dippers, which are suspected to be caused by dust extinction events. This phenomenon is mostly dependent on disk inclination and can occur even for transitional disks, as is the case for prototype Mon-000660 (also known as V354 Mon). Therefore, as with the lack of variability and temperature trends, the fact that there is no global relationship with disk flux is not particularly surprising.

9. SUMMARY

We have analyzed a sample of 162 disk-bearing members of NGC 2264 with high-cadence time series photometry in the optical from *CoRoT* and in the mid-infrared from *Spitzer*. Overall, we find that 81% of our disk-bearing sample is variable in the optical and 91% is variable in the infrared. While the stars without disks will be the subject of a future paper, we have found that the infrared variability level among these is much lower, at 36%. These statistics confirm that accretion disk processes are strongly associated with flux changes. The timescales composing the aperiodic variability span a range from a few days out to the duration of the data set.

We identify seven light-curve morphology classes in each band, including quasi-periodic variability, dippers, bursters, stochastic behavior, strictly periodic, and long-timescale behavior. Among the optical variables, quasi-periodic phenomena are the most common, whereas long-timescale behavior and unclassifiable behavior are the most common in the infrared. Periodic and aperiodic dipper behavior is surprisingly common in the optical, at over 21% of the variability sample. Comparing with the Bertout (2000) prediction of a 15% occurrence rate for occultations by circumstellar material, we infer that either the disk scale height has to be higher than previously assumed, or the

disk obscuration model may be invalid in part. A further puzzle came in the form of two stars (Mon-000183 and Mon-000566) displaying dips that are *deeper* in the infrared (nearly 10%) than in the optical (∼2%–3%). A very non-standard extinction law or geometric peculiarities will have to be invoked to explain these two enigmatic objects.

Pure periodicities are very rare in the disk-bearing sample. We argue that each of these classes represents a distinct physical variability mechanism on the star or in the disk. While follow-up studies including spectroscopy are needed to confirm physical mechanisms, the data are consistent with variable circumstellar obscuration, unsteady accretion, rotating starspots, and rapid structural changes in the disk—and likely multiple of these processes happening simultaneously. Some of the variability may be due directly to the effects of these phenomena on physical properties, while some may be due to radiative transfer effects on the SED.

The clear asymmetries in the dipper- and burster-type light curves motivated us to develop a statistic measure of asymmetry, "*M*." In combination with the quasi-periodicity, "*Q*," we can uniquely identify the variability type of each star in each band without relying on subjective evaluation. Although we set out to understand the wavelength dependence of variability in our sample, we have found that in fact optical and infrared variability behavior in young disk-bearing stars is not well correlated in over 50% of cases. Most of our stars have different optical and infrared classes, with dipping and bursting behavior becoming less common at longer wavelengths and long-timescale variability becoming more common.

We highlight the set of high-amplitude infrared variables for which there is little to no corresponding variability in the optical. We have measured timescales of order ∼5–10 days for these variables, providing evidence that they represent structural rearrangements in the disk. Among the entire sample, we find that high-amplitude (>0.1 mag) infrared variability appears in objects with SED class of type II and earlier, whereas the majority of type II/III transitional disk systems have rms infrared amplitudes less than 0.05 mag. Other correlations identified between variability properties and star/disk parameters include increases in aperiodic amplitude with stellar effective temperature, as well as increased flux asymmetry with Hα equivalent width. These correlations hint at a connection between variability properties and magnetospheric structure.

Overall, we have developed a process for automatically classifying variability that can be applied to other data sets and clusters as well. We have focused exclusively on time series photometry from *CoRoT* and *Spitzer* here, but in future papers we will explore variability at the full range of available wavelengths.

This work is based in part on observations made with the *Spitzer Space Telescope*, which is operated by the Jet Propulsion Laboratory, California Institute of Technology under a contract with NASA. Support for this work was provided by NASA through an award issued by JPL/Caltech. S.H.P.A. acknowledges support from CNpq, CAPES, and Fapemig. R.G. gratefully acknowledges funding support from NASA ADAP grants NNX11AD14G and NNX13AF08G and Caltech/JPL awards 1373081, 1424329, and 1440160 in support of *Spitzer Space Telescope* observing programs. M.M.G. acknowledges support from INCT-A/CNPq. K.Z. received a Pegasus Marie Curie Fellowship of the Research Foundation Flanders (FWO) during part of this work and received funding from the European Research Council under the European Community's Seventh Framework Programme (FP7/2007–2013)/ERC grant agreement No. 227224 (PROSPERITY).

APPENDIX

A.1. NGC 2264 Membership Criteria

NGC 2264 has been the subject of many young cluster studies, from photometric and Hα censuses (e.g., Rebull et al. 2002; Lamm et al. 2004) to X-ray (e.g., Ramírez et al. 2004a; Flaccomio et al. 2006; Feigelson et al. 2013) and radial velocity surveys (e.g., Fűrész et al. 2006). To cull a reliable membership list from candidates reported in the literature, we required that objects meet at least two of six criteria: (1) photometric data consistent with the $V-I$ or $R-I$ cluster locus defined by Flaccomio et al. (2006) (see their Section 3.2); (2) strong photometric Hα emission, according to the criteria of Sung et al. (2008), *or* spectroscopic Hα EW larger than 10 Å; (3) X-ray detection at a flux greater than 10^{-4} $L_{\rm bol}$ (Ramírez et al. 2004a, 2004b; Flaccomio et al. 2006); (4) radial velocity consistent with NGC 2264 membership, as classified by Fűrész et al. (2006); (5) mid-infrared excess indicating a disk (i.e., Class I, II, or flat SED, according to selection methods described in Section 4.2); and (6) spatial location coinciding with an $A_V > 7$ region of NGC 2264, if an object displays an infrared excess or X-ray emission but is not detected in the optical.

We identified highly embedded objects for criterion (6) by plotting X-ray and mid-infrared source locations on the extinction map produced by Teixeira et al. (2012). These obscured stars were added to our overall membership list for further study, but not included in this paper since we are focusing specifically on targets with *CoRoT* detections.

The above requirements eliminate most field dwarf and extragalactic contaminants from our membership sample. We have avoided selecting members based on variability detection so as not to bias our statistical analysis of the light-curve types.

A.2. IRAC Staring Data

While not used extensively in this paper, the high-cadence staring data from *Spitzer*/IRAC offer an important window into short-timescale infrared variability in YSOs. In preparing it for analysis, we performed a series of procedures to remove systematics. The steps described below may be of general interest to other *Spitzer*/IRAC users.

A.2.1. Staring Data Quality and Correction of Systematics

The pixel-phase effect, or variation of measured flux as a function of sub-pixel position, is a known issue affecting the IRAC detector (see the IRAC instrument handbook, v2.0.3). Intrapixel sensitivity variations introduce two systematic effects to the staring (i.e., continuous, non-dithered) light curves: first, the flux may vary up to 6% as the pointing shifts gradually from one side of a pixel to the other; second, the flux exhibits oscillations at the percent level on <1 hr timescales. The first effect reflects the pointing stability of *Spitzer*, while the second was determined by the engineering team to be associated with the cycling of a battery heater on board the satellite, causing periodic flexure between the star tracker and the cold focal plane. The result is that the pointing center on the detector oscillates within individual pixels, convolving their sensitivity variations with the intrinsic flux. In 2010 October, the *Spitzer* engineering team was able to reduce both the amplitude and period of the

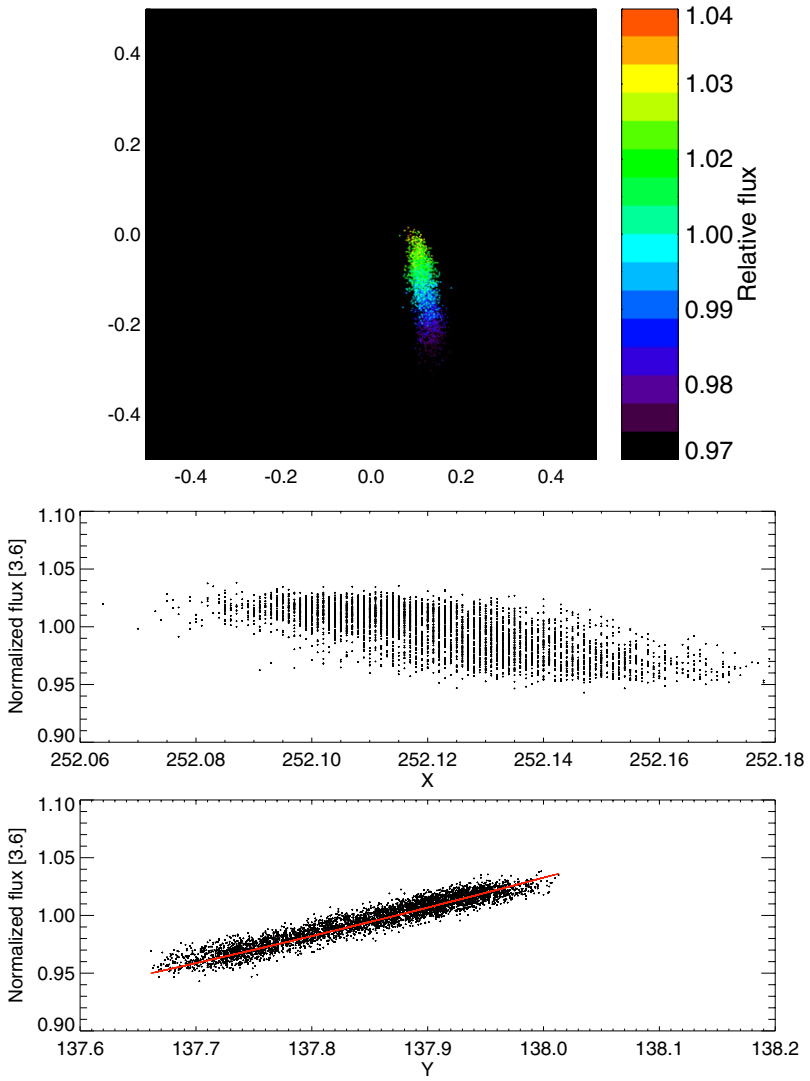

Figure 46. Normalized flux values as a function of pixel position for a non-variable star in our sample (top). The coordinate 0,0 is the pixel center. The pointing varied primarily in the *Y* direction, as shown in the flux vs. *Y* and flux vs. *X* plots at middle and bottom. The red line indicates the slope in flux vs. *Y* that minimizes the pixel-phase peak in the periodogram shown in Figure 47; this is *not* a direct linear fit to the data.

(A color version of this figure is available in the online journal.)

heater-associated temperature fluctuations, the latter from ∼60 minutes to ∼40 minutes. However, the effect remains prominent at the 0.5% level in both channels, comparable to the white-noise contribution for bright stars in the sample.

Our goal of assessing infrared variability of young stars on short timescales and at low amplitudes necessitates the removal of pixel-phase variations to the extent possible from the data. A pixel-phase correction exists for Warm *Spitzer* observations, but tests on our light curves revealed that it works for stars on some pixels, but not others. Several techniques have been developed to provide a more consistent correction, many of which involve fitting a polynomial to the flux as a function of detector *X* and *Y* position (e.g., Bonfils et al. 2011). Unfortunately, this approach does not work well for many of our targets, as the erratic variability that we seek to study cannot be modeled analytically and thus prevents a robust fit. In Cody & Hillenbrand (2011), we adopted a different technique, involving a Gaussian model of the intra-pixel sensitivity variation, for which free parameters were fit by minimizing the height of the pixel-phase oscillation peak in the periodogram. Maps of the pixel sensitivity were determined independently for each star, and the inferred flux variation as a function of *X* and *Y* position was then subtracted from the light curves.

While this method provided satisfactory corrections without compromising intrinsic stellar variability, it was computationally intensive. To apply a similar technique to our ∼500 staring targets, we require an algorithm with fewer free parameters. Fortunately, during our 2011 observations of NGC 2264, object centroids were stable to ∼0.08 pixel (i.e., 0.″1) in the *X* detector position over the course of each 16–26 hr staring mode observation. Flux variations are much better correlated with the *Y* centroids, which vary by 0.3–0.4 pixels (0.″3–0.″5). Plots of the normalized flux versus *Y* for stars lacking obvious variability by eye revealed nearly linear trends, as shown in Figure 46. We therefore chose a basic pixel-phase correction that fits a single slope characterizing the pixel sensitivity as a function of *Y* position. To determine this slope, *A*, we express the sensitivity, *s*, as a linear function of *Y* position on the detector:

$$s(y) = A(y - y_{\rm med}) + 1. \quad \text{(A1)}$$

Here we have normalized the sensitivity to a median value of 1.0 in the area of the pixel where the data fall. Applying

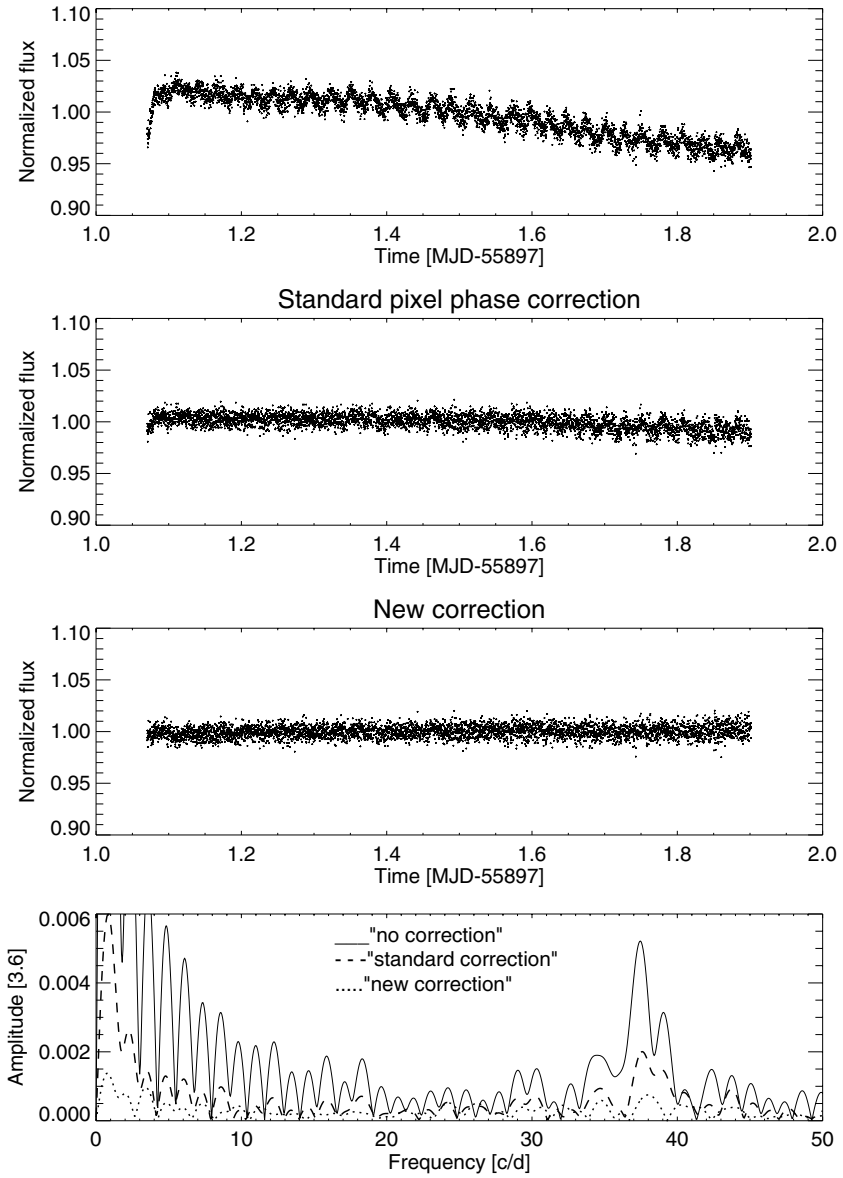

Figure 47. Top: uncorrected light curve, showing the pixel-phase oscillation, as well as longer timescale systematics. Middle: light curve processed with the standard Warm *Spitzer* pixel-phase correction; this algorithm does not fully remove the systematics. Bottom: light curve corrected by the procedure described in this paper. Below these light curves, we display the periodograms of the corrected light curves (dashed, dotted curves), as compared with the periodogram of the raw light curve (solid curve).

this sensitivity function, the true flux data, $d_{\rm true}(y)$, will be observed as

$$d_{\rm obs}(y) = d_{\rm true}(A(y - y_{\rm med}) + 1). \quad \text{(A2)}$$

Note that we have specified the observed and true data to have the same median. To correct the observed data, we then invert this equation, exploiting the fact that $y - y_{\rm med} \ll 1$:

$$d_{\rm true}(y) = d_{\rm obs}/(A(y-y_{\rm med})+1) \sim d_{\rm obs}(1-A(y-y_{\rm med})). \quad \text{(A3)}$$

We wish to determine the value of A so that the corrected light curve is devoid of pixel-related systematics. To do this, we take advantage of the pixel-phase effect, which causes $y(t)$, the detector position, to oscillate rapidly as a function of time. The period of oscillation is approximately 40 minutes. To determine this value more accurately, we compute a Fourier transform periodogram for each chunk of staring data, $y(t)$, first subtracting out its median value $y_{\rm med}$ to remove low-frequency systematics:

$$FT(f, y(t_k)) = \frac{2}{N}\left[\left(\sum_{k=0}^{N}\sin(-2\pi f t_k)(y(t_k) - y_{\rm med})\right)^2 + \left(\sum_{k=0}^{N}\cos(-2\pi f t_k)(y(t_k) - y_{\rm med})\right)^2\right]^{1/2}, \quad \text{(A4)}$$

where f is frequency in the periodogram, k is the index of points in the time series, and N is the total number of points. We numerically locate the highest peak in this periodogram and note its frequency, f_0. We find a value of $\sim$37.5 cycles per day; this can be seen with the solid curve in the bottom panels of Figure 47. The corresponding pixel-phase period is $1/f_0 \sim 38.4$ minutes.

We will now use the oscillatory behavior of $y(t)$ to determine the best value of the slope A in the pixel sensitivity function $s(y)$. We do this by minimizing the value of the Fourier transform periodogram of the data themselves, $d(y(t_k))$, at f_0. The value of A resulting from this process can then be used to remove the effects of pixel sensitivity variation from the data without compromising variability. We begin by writing out the Fourier transform periodogram for the true data, again subtracting out the median value, $d_{\rm med}$, to eliminate periodogram systematics:

$$FT(f, d(y(t_k)) = \frac{2}{N}\left[\left(\sum_{k=0}^{N}\sin(-2\pi f t_k)(d_{\rm true}(t_k) - d_{\rm med})^2 + \left(\sum_{k=0}^{N}\cos(-2\pi f t_k)(d_{\rm true}(t_k) - d_{\rm med})\right)^2\right]^{1/2}$$
$$= \frac{2}{N}\left[\left(\sum_{k=0}^{N}\sin(-2\pi f t_k)(d_{\rm obs}(t_k)\cdot(1 - A(y_k - y_{\rm med})) - d_{\rm med})\right)^2 + \left(\sum_{k=0}^{N}\cos(-2\pi f t_k)(d_{\rm obs}(t_k)\cdot(1 - A(y_k - y_{\rm med})) - d_{\rm med})\right)^2\right]^{1/2}. \quad \text{(A5)}$$

We next minimize the periodogram with respect to the slope, A, at the peak frequency f_0:

$$\frac{d{\rm FT}(f_0, d(y(t_k))}{dA} = 0. \quad \text{(A6)}$$

It can be shown that this equation takes the form

$$0 = AC_1 + C_2 + AC_3 + C_4, \quad \text{(A7)}$$

where C_1, C_2, C_3, and C_4 are constants, as follows:

$$C_1 = -\left[\sum_{k=0}^{N}\sin(-2\pi f_0 t_k)\frac{d_{\rm obs}(t_k)}{d_{\rm med}}\cdot(y_k - y_{\rm med})\right]^2, \quad \text{(A8)}$$

$$C_2 = \left[\sum_{k=0}^{N}\sin(-2\pi f_0 t_k)\left(\frac{d_{\rm obs}(t_k)}{d_{\rm med}} - 1\right)\right] \times \left[\sum_{k=0}^{N}\sin(-2\pi f_0 t_k)\frac{d_{\rm obs}(t_k)}{d_{\rm med}}\cdot(y_k - y_{\rm med})\right], \quad \text{(A9)}$$

$$C_3 = -\left[\sum_{k=0}^{N}\cos(-2\pi f_0 t_k)\frac{d_{\rm obs}(t_k)}{d_{\rm med}}\cdot(y_k - y_{\rm med})\right]^2, \quad \text{(A10)}$$

$$C_4 = \left[\sum_{k=0}^{N}\cos(-2\pi f_0 t_k)\left(\frac{d_{\rm obs}(t_k)}{d_{\rm med}} - 1\right)\right] \times \left[\sum_{k=0}^{N}\cos(-2\pi f_0 t_k)\frac{d_{\rm obs}(t_k)}{d_{\rm med}}\cdot(y_k - y_{\rm med})\right]. \quad \text{(A11)}$$

Operating on the four sections of by-BCD staring light curves, we determine analytically the slope A that minimizes the pixel-phase oscillation signal by computing

$$A = \frac{-(C_2 + C_4)}{C_1 + C3}. \quad \text{(A12)}$$

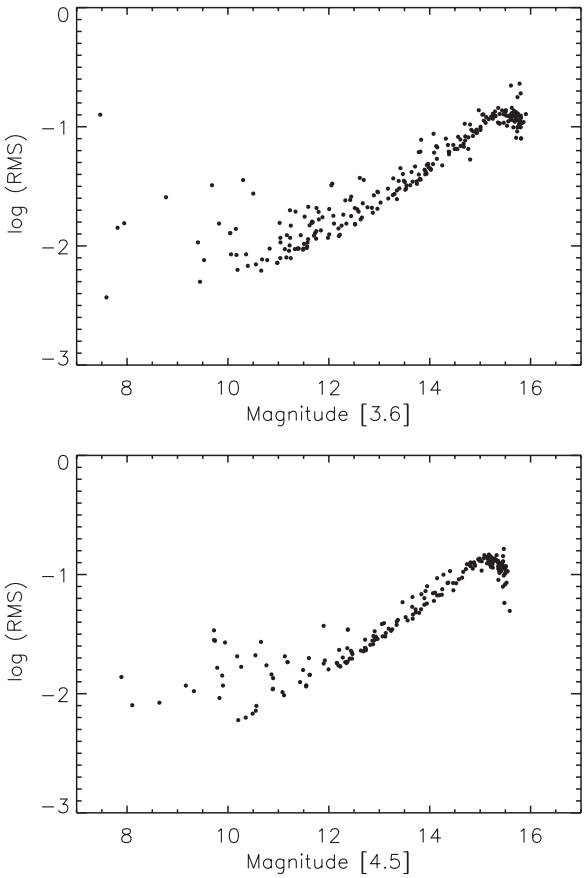

Figure 48. Standard deviations for the first section of IRAC staring light curves in channel 1 (top) and channel 2 (bottom), as a function of magnitude. The lower envelope of values closely matches the uncertainties predicted by Poisson noise and sky background, whereas the higher values are due to stellar variability.

Finally, we divide out the pixel response from the light-curve sections by calculating $d_{\rm true}$ as in Equation (3). Because the X and Y positions are well correlated in time, elimination of the variation associated with shifts in Y only should effectively remove flux trends in X as well (see Figure 46).

Application of our algorithm resulted in a substantial reduction in the level of systematic variability in our light curves, as indicated by both visual inspection and measurement of the height of the periodogram peak at the 40 minute pixel-phase oscillation period. An example comparing our modified correction with the standard correction and a raw light curve is shown in Figure 47. For approximately 1% of light curves, the pixel sensitivity distribution was not well modeled by a linear fit and our correction introduced oscillatory features that were not present in the original light curve. In these cases, we retained the raw light curve or the version corrected with the standard Warm *Spitzer* pixel-phase prescription, depending on which one displayed lower levels of systematics.

The rms values of the corrected 3.6 μm staring light curves ranged from 0.003 mag (at a magnitude of 7.5) to 0.1 mag (at a magnitude of 15.5). The 4.5 μm light curves had similar but slightly lower precision (by a factor of $\sim$1.5). The rms values as a function of magnitude for one of the staring photometry sections are presented in Figure 48; these are consistent with the predicted uncertainties based on Poisson noise and sky background.

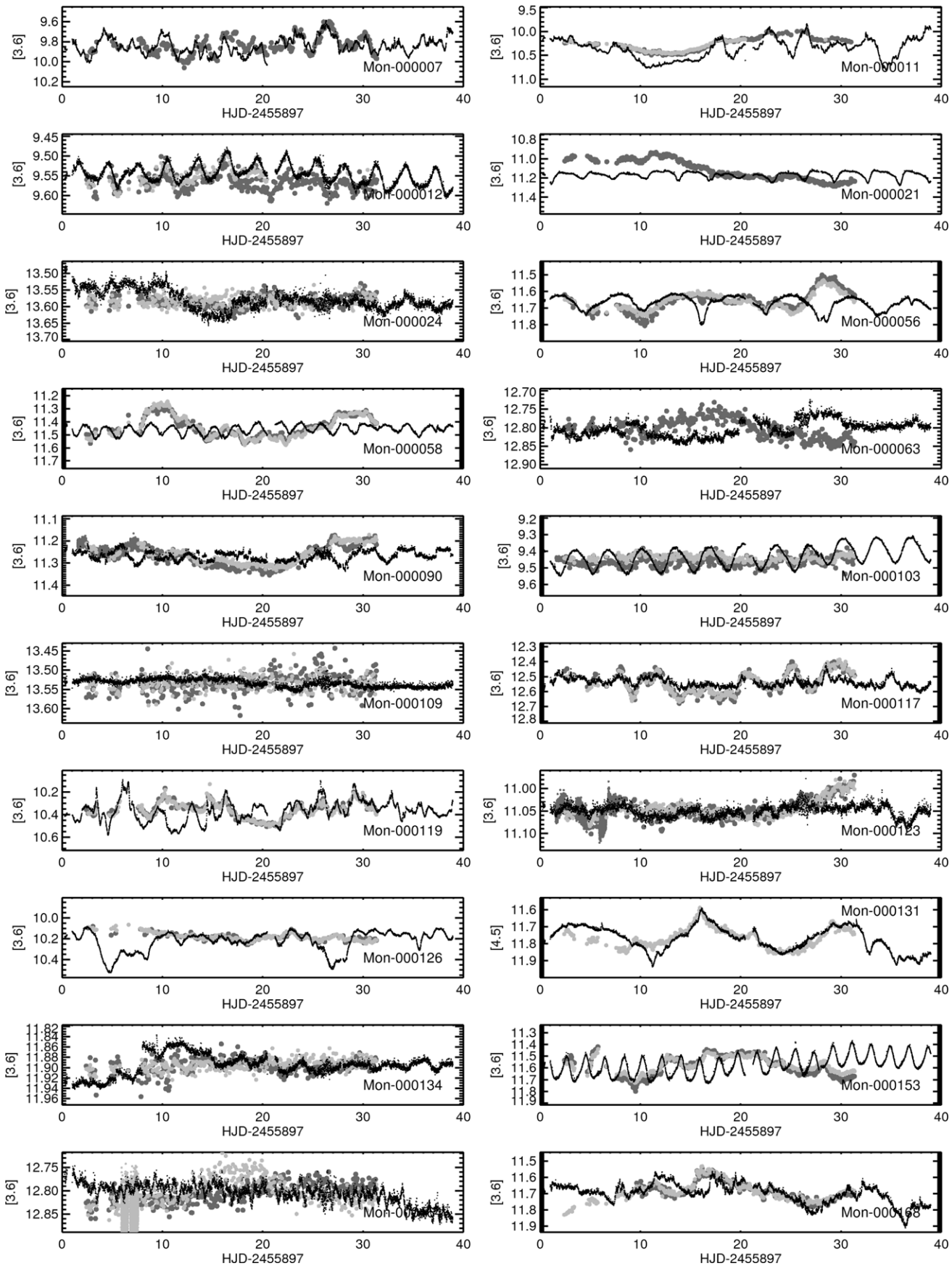

Figure 49. Light curves for all stars in the 162 member disk-bearing sample of this paper. Small black points are *CoRoT* data, light gray points are IRAC 3.6 μm data, and dark gray points are IRAC 4.5 μm data (sometimes hidden behind the 3.6 μm points). More information is available in Tables 3 and 4; objects are presented in the same order here.

(An extended version of this figure is available in the online journal.)

A.2.2. Merging the Mapping and Staring Data

Each section of staring photometry was surrounded by lower cadence mapping photometry. While both data types contain the same systematics, those taken in mapping mode are much less correlated in time, since the dithering and other pointing changes sample the varying pixel sensitivity in a random manner. We therefore cannot remove the mapping systematics but have accounted for them (e.g., Section 3.3) for statistical purposes. Much of the staring photometry, on the other hand, displays significant and correctable zero-point offsets from the surrounding mapping points. This effect occurs when the sensitivity of a single pixel containing the object centroid during a staring observation differs from the mean sensitivity across the many different pixels occupied during mapping observations. Since discontinuities in the light curves create challenges for variability analysis, we have introduced a further set of corrections to ensure smooth transitions between staring and mapping photometry. Following pixel-phase mitigation, we selected the set of ∼280 by-BCD staring points lying within 1.2 hr of the beginning or end of each staring data section. Likewise, we select the set of ∼6 mapping points (from by-AOR photometry) lying within 9.6 hr of the beginning or end of each mapping section. For each set of photometry, we computed a linear fit to the magnitudes as a function of time, to account for short-timescale variability. Offsets between adjacent staring and mapping light-curve sections were then determined by subtracting the fit values at the point midway between them. Each staring section had an offset at both ends, from which we determined the mean. This final offset was then applied to the entire staring section, thereby knitting it to the surrounding mapping data.

The typical offset between staring and mapping data was ±0.01–0.05 mag. It is unclear as to why it is often larger than the random scatter in the mapping data. Since the offset fits are undoubtedly affected by observational noise, we use the combined light curves with caution and provide statistics separately for mapping data and individual staring data sections. To produce staring light curves with lower uncertainties, we further binned sets of 10 points for a final cadence of 2.5 minutes. In all, there were twenty-six stars in our disk-bearing sample with both IRAC staring data and *CoRoT* observations.

A.3. Complete Combined Optical/Infrared Data Set

We assemble in Figure 49 the entire 162 member disk-bearing data set observed by *CoRoT* and *Spitzer*. Small black dots are optical data, light gray points are 3.6 μm data, and dark gray points are 4.5 μm data.

REFERENCES

Affer, L., Micela, G., Favata, F., Flaccomio, E., & Bouvier, J. 2013, MNRAS, 430, 1433
Alencar, S. H. P., Teixeira, P. S., Guimarães, M. M., et al. 2010, A&A, 519, A88
Alves de Oliveira, C., & Casali, M. 2008, A&A, 485, 155
Artemenko, S. A., Grankin, K. N., & Petrov, P. P. 2012, AstL, 38, 783
Auvergne, M., Bodin, P., Boisnard, L., et al. 2009, A&A, 506, 411
Bachiller, R. 1996, ARA&A, 34, 111
Baglin, A., Auvergne, M., Barge, P., et al. 2006, in Proc. The CoRoT Mission Pre-Launch Status—Stellar Seismology and Planet Finding, ed. M. Fridlund, A. Baglin, J. Lochard, & L. Conroy (ESA Special Publication, Vol. 1306; Noordwijk: ESA), 33
Barsony, M., Ressler, M. E., & Marsh, K. A. 2005, ApJ, 630, 381
Batalha, C. C., Quast, G. R., Torres, C. A. O., et al. 1998, A&AS, 128, 561
Bertout, C. 1989, ARA&A, 27, 351
Bertout, C. 2000, A&A, 363, 984
Bertout, C., Basri, G., & Bouvier, J. 1988, ApJ, 330, 350
Billot, N., Morales-Calderón, M., Stauffer, J. R., Megeath, S. T., & Whitney, B. 2012, ApJL, 753, L35
Bonfils, X., Gillon, M., Forveille, T., et al. 2011, A&A, 528, A111
Bouvier, J., Alencar, S. H. P., Boutelier, T., et al. 2007, A&A, 463, 1017
Bouvier, J., Cabrit, S., Fernandez, M., Martin, E. L., & Matthews, J. M. 1993, A&A, 272, 176
Bouvier, J., Chelli, A., Allain, S., et al. 1999, A&A, 349, 619
Bouvier, J., Grankin, K. N., Alencar, S. H. P., et al. 2003, A&A, 409, 169
Breger, M., Stich, J., Garrido, R., et al. 1993, A&A, 271, 482
Caballero, J. A., Béjar, V. J. S., Rebolo, R., & Zapatero Osorio, M. R. 2004, A&A, 424, 857
Carpenter, J. M., Hillenbrand, L. A., & Skrutskie, M. F. 2001, AJ, 121, 3160
Carpenter, J. M., Hillenbrand, L. A., Skrutskie, M. F., & Meyer, M. R. 2002, AJ, 124, 1001
Cauley, P. W., Johns-Krull, C. M., Hamilton, C. M., & Lockhart, K. 2012, ApJ, 756, 68
Chelli, A., Carrasco, L., Mújica, R., Recillas, E., & Bouvier, J. 1999, A&A, 345, L9
Cieza, L., & Baliber, N. 2006, ApJ, 649, 862
Cody, A. M., & Hillenbrand, L. A. 2010, ApJS, 191, 389
Cody, A. M., & Hillenbrand, L. A. 2011, ApJ, 741, 9
Cody, A. M., Tayar, J., Hillenbrand, L. A., Matthews, J. M., & Kallinger, T. 2013, AJ, 145, 79
Cohen, R. E., Herbst, W., & Williams, E. C. 2003, ApJL, 596, L243
Cohen, R. E., Herbst, W., & Williams, E. C. 2004, AJ, 127, 1602
Dahm, S. E. 2008, in Handbook of Star Forming Regions, Volume 1, ed. B. Reipurth (San Francisco, CA: ASP), 966
Dahm, S. E., & Simon, T. 2005, AJ, 129, 829
Dullemond, C. P., van den Ancker, M. E., Acke, B., & van Boekel, R. 2003, ApJL, 594, L47
Eiroa, C., Oudmaijer, R. D., Davies, J. K., et al. 2002, A&A, 384, 1038
Espaillat, C., Furlan, E., D'Alessio, P., et al. 2011, ApJ, 728, 49
Evans, N., Calvet, N., Cieza, L., et al. 2009, arXiv:0901.1691
Faesi, C. M., Covey, K. R., Gutermuth, R., et al. 2012, PASP, 124, 1137
Fazio, G. G., Hora, J. L., Allen, L. E., et al. 2004, ApJS, 154, 10
Feigelson, E. D., Townsley, L. K., Broos, P. S., et al. 2013, ApJS, 209, 26
Fernandez, M., & Eiroa, C. 1996, A&A, 310, 143
Findeisen, K., Hillenbrand, L., Ofek, E., et al. 2013, ApJ, 768, 93
Flaccomio, E., Micela, G., & Sciortino, S. 2006, A&A, 455, 903
Flaherty, K. M., & Muzerolle, J. 2010, ApJ, 719, 1733
Flaherty, K. M., Muzerolle, J., Rieke, G., et al. 2012, ApJ, 748, 71
Frasca, A., Covino, E., Spezzi, L., et al. 2009, A&A, 508, 1313
Fűrész, G., Hartmann, L. W., Szentgyorgyi, A. H., et al. 2006, ApJ, 648, 1090
Grankin, K. N., Bouvier, J., Herbst, W., & Melnikov, S. Y. 2008, A&A, 479, 827
Grankin, K. N., Melnikov, S. Y., Bouvier, J., Herbst, W., & Shevchenko, V. S. 2007, A&A, 461, 183
Greene, T. P., Wilking, B. A., Andre, P., Young, E. T., & Lada, C. J. 1994, ApJ, 434, 614
Gregory, S. G., Donati, J.-F., Morin, J., et al. 2012, ApJ, 755, 97
Gutermuth, R. A., Megeath, S. T., Myers, P. C., et al. 2009, ApJS, 184, 18
Herbst, W., Herbst, D. K., Grossman, E. J., & Weinstein, D. 1994, AJ, 108, 1906
Herbst, W., LeDuc, K., Hamilton, C. M., et al. 2010, AJ, 140, 2025
Herbst, W., Maley, J. A., & Williams, E. C. 2000, AJ, 120, 349
Herbst, W., & Shevchenko, V. S. 1999, AJ, 118, 1043
Indebetouw, R., Mathis, J. S., Babler, B. L., et al. 2005, ApJ, 619, 931
Joy, A. H. 1949, ApJ, 110, 424
Kesseli, A., Whitney, B., Wood, K., et al. 2013, BAAS, 45, #256.10
Koldoba, A. V., Ustyugova, G. V., Romanova, M. M., & Lovelace, R. V. E. 2008, MNRAS, 388, 357
Lada, C. J., & Wilking, B. A. 1984, ApJ, 287, 610
Lamm, M. H., Bailer-Jones, C. A. L., Mundt, R., Herbst, W., & Scholz, A. 2004, A&A, 417, 557
Lasker, B. M., Sturch, C. R., McLean, B. J., et al. 1990, AJ, 99, 2019
Makidon, R. B., Rebull, L. M., Strom, S. E., Adams, M. T., & Patten, B. M. 2004, AJ, 127, 2228
McQuillan, A., Aigrain, S., & Mazeh, T. 2013, MNRAS, 432, 1203
Mislis, D., Schmitt, J. H. M. M., Carone, L., Guenther, E. W., & Pätzold, M. 2010, A&A, 522, A86
Morales-Calderón, M., Stauffer, J. R., Hillenbrand, L. A., et al. 2011, ApJ, 733, 50
Morales-Calderón, M., Stauffer, J. R., Rebull, L., et al. 2009, ApJ, 702, 1507
Muzerolle, J., Flaherty, K., Balog, Z., et al. 2009, ApJL, 704, L15
Parenago, P. P. 1954, TrSht, 25, 1
Park, B.-G., Sung, H., Bessell, M. S., & Kang, Y. H. 2000, AJ, 120, 894
Parks, J. R., Plavchan, P., White, R. J., & Gee, A. H. 2014, ApJS, 211, 3

Pilbratt, G. L., Riedinger, J. R., Passvogel, T., et al. 2010, A&A, 518, L1
Plavchan, P., Gee, A. H., Stapelfeldt, K., & Becker, A. 2008a, ApJL, 684, L37
Plavchan, P., Güth, T., Laohakunakorn, N., & Parks, J. R. 2013, A&A, 554, A110
Plavchan, P., Jura, M., Kirkpatrick, J. D., Cutri, R. M., & Gallagher, S. C. 2008b, ApJS, 175, 191
Press, W. H. 1978, ComAp, 7, 103
Ramírez, S. V., Rebull, L., Stauffer, J., et al. 2004a, AJ, 127, 2659
Ramírez, S. V., Rebull, L., Stauffer, J., et al. 2004b, AJ, 128, 787
Reach, W. T., Megeath, S. T., Cohen, M., et al. 2005, PASP, 117, 978
Rebull, L. M. 2011, in ASP Conf. Ser. 448, 16th Cambridge Workshop on Cool Stars, Stellar Systems, and the Sun, ed. C. Johns-Krull, M. K. Browning, & A. A. West (San Francisco, CA: ASP), 5
Rebull, L. M., Makidon, R. B., Strom, S. E., et al. 2002, AJ, 123, 1528
Rice, T. S., Wolk, S. J., & Aspin, C. 2012, ApJ, 755, 65
Rodríguez-Ledesma, M. V., Mundt, R., & Eislöffel, J. 2009, A&A, 502, 883
Romanova, M. M., Kulkarni, A. K., & Lovelace, R. V. E. 2008, ApJL, 673, L171
Romanova, M. M., Ustyugova, G. V., Koldoba, A. V., & Lovelace, R. V. E. 2011, MNRAS, 416, 416
Rucinski, S. M., Matthews, J. M., Kuschnig, R., et al. 2008, MNRAS, 391, 1913
Rucinski, S. M., Zwintz, K., Hareter, M., et al. 2010, A&A, 522, A113
Samadi, R., Fialho, F., Costa, J. E. S., et al. 2006, in Proc. The CoRoT Mission Pre-Launch Status—Stellar Seismology and Planet Finding, ed. M. Fridlund, A. Baglin, J. Lochard, & L. Conroy (ESA Special Publication, Vol. 1306; Noordwijk: ESA), 317
Scholz, A. 2012, MNRAS, 420, 1495
Scholz, A., Xu, X., Jayawardhana, R., et al. 2009, MNRAS, 398, 873
Siwak, M., Rucinski, S. M., Matthews, J. M., et al. 2011, MNRAS, 410, 2725
Skrutskie, M. F., Meyer, M. R., Whalen, D., & Hamilton, C. 1996, AJ, 112, 2168
Stassun, K., & Wood, K. 1999, ApJ, 510, 892
Stassun, K. G., Mathieu, R. D., Mazeh, T., & Vrba, F. J. 1999, AJ, 117, 2941
Stauffer, J. R., Cody, A. M., Baglin, A., et al. 2014, AJ, 147, 83
Stetson, P. B. 1996, PASP, 108, 851
Sung, H., Bessell, M. S., Chun, M.-Y., Karimov, R., & Ibrahimov, M. 2008, AJ, 135, 441
Sung, H., Bessell, M. S., & Lee, S.-W. 1997, AJ, 114, 2644
Sung, H., Stauffer, J. R., & Bessell, M. S. 2009, AJ, 138, 1116
Teixeira, P. S., Lada, C. J., Marengo, M., & Lada, E. A. 2012, A&A, 540, A83
Turner, N. J. 2013, BAAS, 45, #205.05
van Boekel, R., Juhász, A., Henning, T., et al. 2010, A&A, 517, A16
Vrba, F. J., Chugainov, P. F., Weaver, W. B., & Stauffer, J. S. 1993, AJ, 106, 1608
Walker, M. F. 1956, ApJS, 2, 365
Weaver, W. B., & Frank, J. L. 1980, MNRAS, 191, 321
Werner, M. W., Roellig, T. L., Low, F. J., et al. 2004, ApJS, 154, 1
Wilking, B. A., Bontemps, S., Schuler, R. E., Greene, T. P., & André, P. 2001, ApJ, 551, 357
Wolk, S. J., Rice, T. S., & Aspin, C. 2013, ApJ, 773, 145
Zwintz, K., Kallinger, T., Guenther, D. B., et al. 2011, ApJ, 729, 20